HOKKAIDO UNIVERSITY

Title	Electrocatalytic nitrate and nitrous oxide reduction reactions at trimetallic interfaces of Pt, Pd and Sn
Author(s)	Sarker, Abinash Chandro
Degree Grantor	北海道大学
Degree Name	博士(環境科学)
Dissertation Number	甲第15132号
Issue Date	2022-09-26
DOI	https://doi.org/10.14943/doctoral.k15132
Doc URL	https://hdl.handle.net/2115/96081
Type	doctoral thesis
File Information	Sarker_Abinash_Chandro.pdf

Hokkaido University Collection of Scholarly and Academic Papers : HUSCAP

Doctoral Thesis

Electrocatalytic nitrate and nitrous oxide reduction reactions at trimetallic interfaces of Pt, Pd and Sn



Abinash Chandro Sarker

Division of Environmental Materials Science
Graduate School of Environmental Science
Hokkaido University

September 2022

Contents

Chapter 1: General Introduction

1.1 Background for efficient nitrate and nitrous oxide removal 1

1.1.1 Background for efficient nitrate removal 1

1.1.2 Background for efficient nitrous oxide removal 3

1.2 NO_3^- and N_2O removal technologies 4

1.2.1 NO_3^- removal technologies 4

1.2.2 N_2O removal technologies 4

1.3 Electrocatalytic NO_3^- and N_2O reduction 4

1.3.1 NO_3^- and N_2O reduction on monometallic electrodes 5

1.3.2 NO_3^- reduction on bimetallic electrodes 9

1.3.3 NO_3^- reduction on trimetallic electrodes 12

1.3.4 NO_3^- reduction on single crystalline electrodes 14

1.4 Objective of this thesis 16

1.5 Outline of this thesis 17

1.6 References 18

Chapter 2: Electrocatalytic Nitrate and Nitrous Oxide Reduction at Interfaces Between Pt-Pd Nanoparticles and Fluorine-Doped Tin Oxide

2.1 Introduction 27

2.2 Experimental 28

2.2.1 Materials 28

2.2.2 Electrode preparation 28

2.2.3 Electrochemical measurements 29

2.2.4 Physicochemical characterizations 30

2.3 Results and discussion 30

2.3.1 Characterization of Pt/FTO and Pd/FTO electrodes 30
2.3.2 Optimizing NO_3RR at Pt/FTO and Pd/FTO electrodes 33
2.3.3 NO_3RR at Pt/Pd/FTO electrodes 37
2.3.4 NO_2RR, NORR, and N_2ORR at Pt/Pd/FTO and Pt/Pd/GC electrodes 40
2.4 Conclusions 43
2.5 References 43

Chapter 3: Electrocatalytic Nitrous Oxide Reduction at Pt–Pd–Sn Nanoparticles

3.1 Introduction 48
3.2 Experimental section 49
3.2.1 Materials 49
3.2.2 Synthesis of Pt–Sn and Pt–Pd–Sn nanoparticles 49
3.2.3 Preparation of carbon-supported Pt–Sn and Pt–Pd–Sn NPs 50
3.2.4 Catalyst characterizations 50
3.2.5 Electrochemical measurements 51
3.2.6 Gaseous product detection and quantification 52
3.3 Results and discussion 54
3.3.1 Characterization of Pt–Sn/C and Pt–Pd–Sn/C 54
3.3.2 Electrocatalytic N_2ORR at Pt–Sn/C and Pt–Pd–Sn/C 58
3.3.3 Product analysis of electrocatalytic N_2ORR 60
3.4 Conclusions 63
3.5 References 63

Chapter 4: Electrocatalytic Nitrous Oxide Reduction at Sn-Modified Pd Nanocubes

4.1 Introduction 66
4.2 Experimental section 67

4.2.1 Materials 67
4.2.2 Synthesis of Pd nanocubes 67
4.2.3 Preparation of carbon-supported Pd NCs 67
4.2.4 Catalyst characterization 68
4.2.5 Electrochemical measurements 68
4.3 Results and discussion 69
4.3.1 Synthesis and characterization of Pd NCs 69
4.3.2 Characterization of Sn-modified Pd_NC/C 71
4.3.3 Electrocatalytic N_2ORR at Sn/Pd_NC/C 72
4.4 Conclusions 74
4.5 References 74

Chapter 5: General Conclusions 77

Acknowledgements 79

Chapter 1

General Introduction

1.1 Background for efficient nitrate and nitrous oxide removal

1.1.1 Background for efficient nitrate removal

Dinitrogen (N_2) in the nitrogen cycle is harmless, but the contamination of groundwater by its most oxidizing state nitrate anion (NO_3^-) is harmful to the environment and human health [1–5]. Anthropogenic activities, such as overuse of nitrogenous fertilizers in agricultural lands, animal feces, discharge of treated wastewater, and industrial effluents are mainly accountable for NO_3^- contamination [6]. Moreover, NO_3^--containing storm-water runoff from urban surfaces also leads to an increase in the amount of NO_3^- in surface and groundwater [7]. The NO_3^--contaminated water causes the eutrophication phenomenon and consequently damages the aquatic ecosystems [8]. NO_3^- is converted into N_2O as a by-product through the biological denitrification processes ($NO_3^- \rightarrow NO_2^- \rightarrow NO \rightarrow N_2O \rightarrow N_2$) in the natural environment, which is accountable for global warming and depletion of the ozone layer [9]. NO_3^- in drinking water is reduced by gastro-intestinal microorganisms into nitrite (NO_2^-) that causes methemoglobinemia, which is called “blue baby syndrome” for children [10]. NO_2^- in the body can react with amino compounds to form *N*-nitrosamines, which are suspected to be carcinogenic [11]. More worryingly, NO_3^- concentration in drinking water has exceeded 100 mg L^{-1} in some countries (Figure 1.1) [12–14]. To minimize the health threats of NO_3^-, the World Health Organization (WHO) has recommended a maximum of 50 mg L^{-1} as NO_3^- (~11 mg L^{-1} as NO_3^--N) in drinking water [15]. In Japan, the maximum concentration based on the sum of NO_3^--N and NO_2^--N is 10 mg L^{-1} [16]. Therefore, efficient technology is required for NO_3^- removal.

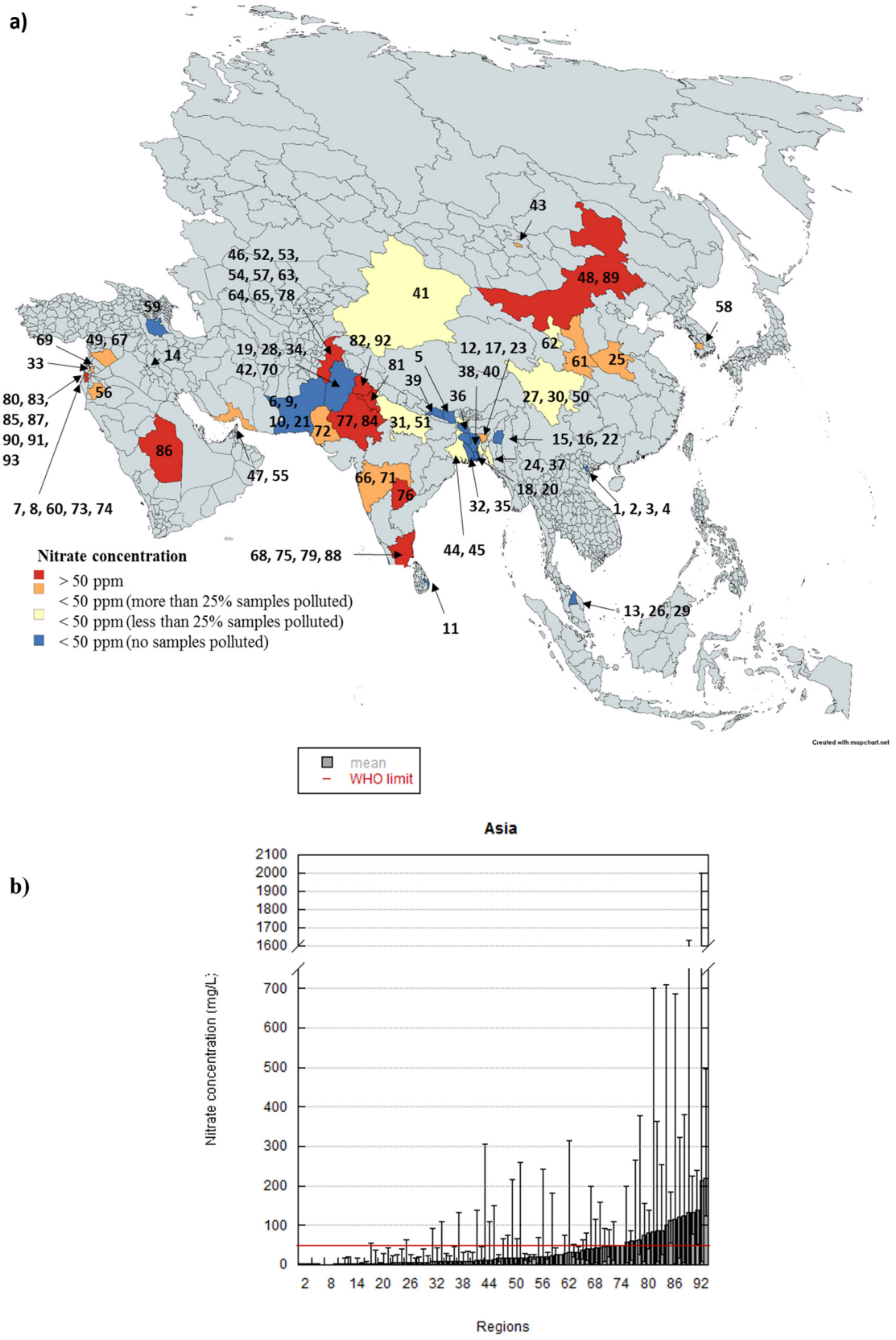


Figure 1.1 (a) Studied regions and b) NO_3^- concentration in groundwater in Asia. Adapted with permission from ref. [12], copyright 2021, Elsevier.

1.1.2 Background for efficient nitrous oxide removal

N_2O is one of the potential by-products of NO_3^- reduction reaction (NO_3RR), which is further reduced to N_2. N_2O is a greenhouse gas and a scavenger for the depletion of the ozone layer [5,17]. N_2O is mainly released from agricultural sources: fertilizers, manures, and crop residues [9]. Combustion of fossil fuels, biomass burning, and industrial activities, such as nitric acid, adipic acid, and caprolactam production plants are also accountable for increasing the concentration of N_2O in the atmosphere [18,19]. The concentration of N_2O in the atmosphere has increased by approximately 14% in 2017 when compared to the concentration in 1940 and has an increasing trend up to date [20]. Global Monitoring Laboratory reported the atmospheric concentration of N_2O of 335 parts per billion (ppb) till January 2022 with an increasing rate of about one ppb annually (Figure 1.2) [21]. The increasing trend of the concentration of N_2O over time is a great matter of concern because of its long lifetime over 100 years and about 300 times greater global warming potential than CO_2 [5,19,22–24]. Therefore, there is an urgent need to develop efficient catalysts that can remove both NO_3^- and N_2O to keep the world sustainable.

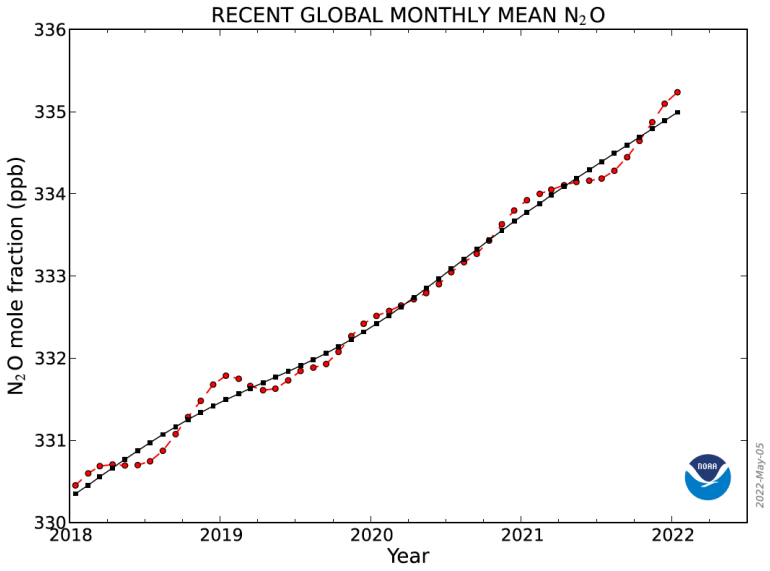


Figure 1.2 Globally-averaged, monthly mean atmospheric nitrous oxide abundance determined from marine surface sites. Adapted with permission from ref. [21], NOAA/GML.

1.2 NO_3^- and N_2O removal technologies

1.2.1 NO_3^- removal technologies

Many technologies have been developed for NO_3^- removal, for example, biological treatments, ion exchanges, reverse osmosis, electrodialysis, electrocoagulation, catalytic reduction, and electrocatalytic reduction processes [25–34]. However, biological denitrification requires a long startup time, ion exchange, reverse osmosis, electrodialysis, and electrocoagulation lead to secondary NO_3^--containing wastewater, and catalytic reduction requires reducing agents, leading to their limited application [26,27,33]. On the other hand, electrocatalytic reduction is the most promising technique for NO_3^- removal because of no production of a secondary NO_3^--containing waste stream, no requirement of additional chemicals, no possibility of bacterial contamination, and renewable energy friendliness [26,34–36].

1.2.2 N_2O removal technologies

To date, several technologies, such as thermal decomposition, direct catalytic decomposition, selective catalytic reduction, and electrocatalytic reduction have been developed for N_2O removal [37–41]. However, thermal decomposition and direct catalytic decomposition require very high (> 800°C) and medium temperatures (> 300–500°C), respectively [37,39,40]. Selective catalytic reduction requires reducing agents like propane/ammonia [38,39]. On the other hand, electrocatalytic N_2O reduction reaction (N_2ORR) does not require any reducing agent and can be powered by green energies like wind and solar powers at room temperature and pressure [36,42]. This method is efficient for not only the reduction of N_2O directly, but also the reduction of N_2O obtained from NO_3RR, leading to a green environment [36].

1.3 Electrocatalytic NO_3^- and N_2O reduction

NO_3^- can electrocatalytically be reduced towards the most desirable product N_2 with the following by-products: nitrite ion (NO_2^-), nitric oxide (NO), nitrous oxide (N_2O), hydroxylamine (NH_2OH/NH_3OH^+), and ammonia (NH_3/NH_4^+) (Figure 1.3) [43–48]. The formation of these by-products is the main obstacle to N_2 selectivity. On the other hand, N_2O is a potential by-product that should be completely reduced to a single product N_2, which is a two-electron and one-step process. Therefore, highly efficient electrode materials are needed to develop for the efficient reduction of both NO_3^- and N_2O to benign

N_2 in terms of the water purification at the family level. Catalytic activity and product selectivity of a catalyst mainly depend on electrode materials and their composition, and surface structure [49].

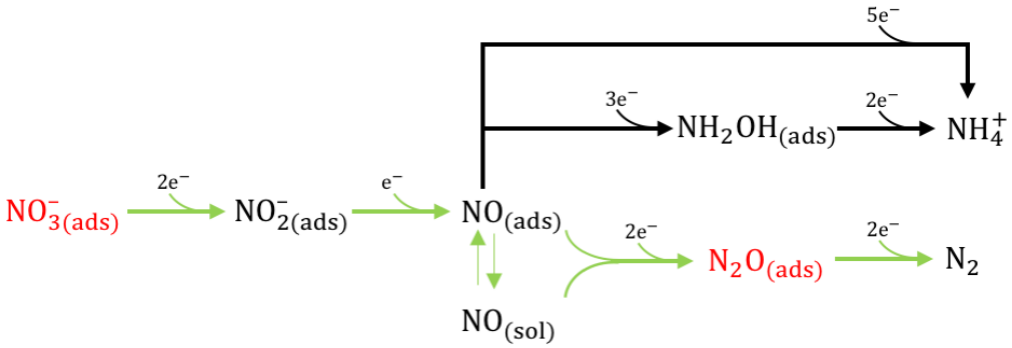


Figure 1.3 The simplified reaction pathway of electrocatalytic NO_3^- and N_2O reduction [43–45].

Numerous studies have been conducted on the development of efficient electrocatalysts for the NO_3RR towards N_2. Monometallic electrocatalysts, such as Pt, Pd, and Cu have been widely studied and show promising properties [26,45,50–52]. Bimetallic electrocatalysts, such as Pt and Pd substrates integrated with promoter metals (p-block elements and Cu) have been widely investigated and show improvement in the NO_3RR activity [53–62]. A few studies on trimetallic catalysts that are composed of Pt+Pd mixture/alloy substrates modified with a 3rd metal as a promoter, such as Sn and Ge have been conducted and show further enhancement of the NO_3RR activity [36,42,43,46]. On the other hand, N_2ORR has been studied mainly on transition metal electrodes [41,63–67].

1.3.1 NO_3^- and N_2O reduction on monometallic electrodes

NO_3^- reduction on monometallic electrodes

In the 1970s, as many as 30 metals (M) including Pt and Pd were studied to compare their electrocatalytic nitric acid/nitrate reduction activity and it was concluded that the nitric acid/nitrate reduction activity of transition metals is related to the volcanic relationship of the M–H and M–O interaction energies [68]. Later five transition metals (Pt, Pd, Rh, Ru, and Ir) were investigated for electrocatalytic NO_3RR in acidic media (0.5 M H_2SO_4+0.1 M $NaNO_3$) and the NO_3RR activity was found to be decreased in the following order: Rh > Ru > Ir > Pt and Pd [45]. Of the transition-metal electrodes, Rh showed the highest NO_3RR activity of about –0.15 mA cm^{-2} at +0.16 V vs. RHE

(reversible hydrogen electrode), which is very low when compared to bi- and trimetallic electrodes described in the next. Pt and Pd showed very low NO_3RR activity due to the co-adsorption of hydrogen or the copetittion with hydrogen adsorption as the NO_3^- has low adsorption enthalpy on Pt and Pd when compared with hydrogen adsorption [45,69–71]. A kinetic finding was reported that the reduction of NO_3^- to NO_2^- is the rate-determining step and the first electron transfer is involved in the rate-determining step (Tafel slope: ~120 mV dec^{-1}) [45,72]. Thermodynamically, the step of the reduction of NO_3^- to NO_2^- shown below was also reported as favorable [50].

$$NO_3^- + 2H^+ + 2e^- \rightarrow NO_2^- + H_2O \quad E^{\ominus} = 0.835\ \text{V vs. NHE}$$

where NHE is the normal hydrogen electrode.

Among the noble metals, there are many findings on Pt and Pd electrodes to understand the process of NO_3RR to N_2. On porous Pt electrode, N_2O and N_2 were reported as gaseous products of NO_3RR below +0.4 V vs. RHE (in the potential region of hydrogen adsorption/desorption) in acidic media (0.5 M H_2SO_4+0.5 M $NaNO_3$) [73]. To further understand the NO_3RR pathway towards N_2, NO_2^- reduction reaction (NO_2RR) was reported on porous Pt electrode in acidic media (0.5 M H_2SO_4+0.012 M $NaNO_2$) and it was concluded that the NO_2^- is converted stepwise to NO (0.6–1 V vs. RHE), N_2O (0.2–0.8 V vs. RHE), and N_2 (0.1–0.6 V vs. RHE) [73]. NO is the key intermediate of the NO_3RR to produce a selective product. Koper *et al.* studied Pt and Pd electrodes for NO reduction reaction (NORR) in acidic (0.1 M H_2SO_4) and alkaline (0.1 M KOH) media [74]. They reported N_2O and NH_4^+ as the products on the Pt electrode without the formation of N_2 and identified the Pd electrode as the best for selective reduction of NO to N_2 through N_2O. They concluded that the adsorbed NO is reduced to NH_3 and both the adsorbed NO and solution NO are necessary for the production of N_2O (Figure 1.3) [45,74]. From the thermodynamic point of view, all the steps involved in the NO_2^- reduction towards N_2 shown below are favorable [41,50,73].

$$NO_2^- + 2H^+ + 2e^- \rightarrow NO + H_2O \quad E^{\ominus} = 1.202\ \text{V vs. NHE}$$
$$2NO + 2H^+ + 2e^- \rightarrow N_2O + H_2O \quad E^{\ominus} = 1.59\ \text{V vs. NHE}$$
$$N_2O + 2H^+ + 2e^- \rightarrow N_2 + H_2O \quad E^{\ominus} = 1.77\ \text{V vs. NHE}$$

N_2O reduction on monometallic electrodes

Many metals including Pt and Pd have been widely studied for electrocatalytic N_2ORR [41,63–67]. The Pt and Pd electrodes showed about 100% Faradaic efficiency of

N_2 produced from N_2ORR in 0.3 M K_2SO_4 aqueous solution, although the adsorpton of N_2O is competitive with hydrogen adsorption on these electrodes in the potential region of hydrogen adsorption/dsorption [41,64,66,67].

To understand the role of adsorbed hydrogen in the electrocatalytic N_2ORR, Ebert *et al.* firstly studided polyoriented Pt single crystalline electrode in acidic media (Figure 1.4) [66]. The N_2ORR was observed in the potential region of hydrogen adsorption/desorption and the reaction was inhibited by the high concentration of adsorbed hydrogen at the more negative potential. They concluded that the adsorbed hydrogen plays an important role for the N_2ORR to N_2 and the reaction between adsorbed N_2O and adsorbed hydrogen is the rate-determining step (rds).

$$H^+ + e^- \rightarrow H_{(ads)}$$

$$N_2O_{(ads)} + H_{(ads)} \rightarrow N_2 + OH_{(ads)} \quad \text{(rds)}$$

$$OH_{(ads)} + H^+ + e^- \rightarrow H_2O \quad \text{(fast)}$$

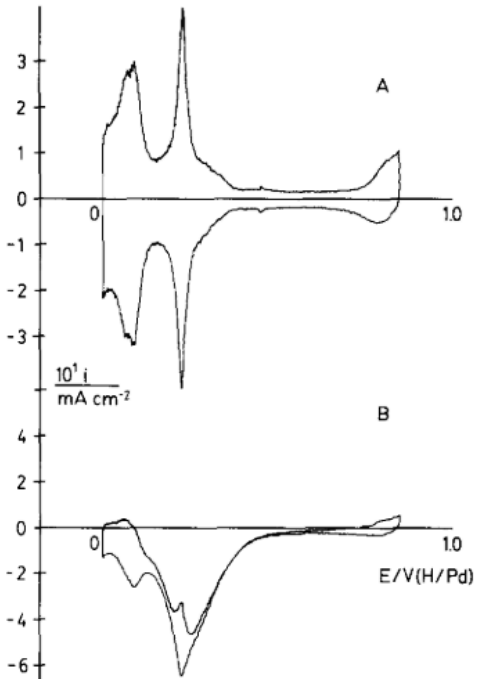


Figure 1.4 Cyclic voltammograms of a spherical Pt single crystal electrode in an aqueous solution of 0.1 M H_2SO_4 (A) under Ar at a sweep rate of 200 mV s^{-1} and (B) under N_2O at a sweep rate of 100 mV s^{-1}. Adapted with permission from ref. [66], copyright 1989, Elsevier.

Later, Attard *et. al.* studied polycrystalline Pd, Rh, Ir(111), and Rh(111) electrodes for electrocatalytic N_2ORR in aqueous H_2SO_4 and $HClO_4$ solutions and reargued on the above-mentioned mechanism [64]. On the polycrystalline Pd electrode, the N_2ORR currents appeared at a more positive potential in $HClO_4$ solution than in H_2SO_4 solution, and the onset potential of N_2ORR in $HClO_4$ aqueous solution was also found to be more positive than a onset potential of hydrogen adsorption/desorption. They interpreted that the adsorbed hydrogen is not essential for the N_2ORR, and N_2ORR begins just at the end of the oxide reduction. The adsorption of SO_4^- causes such difference of onset potential in different electrolyte solutions. They proposed that the rate-determining step should be the $N_2O_{(ads)}$ decomposition to N_2 and adsorbed O, and concluded that the N_2ORR rate depends on available catalytic sites for N_2O adsorption that are free of anions, hydrogen, and oxide [64].

$$M - N_2O_{(ads)} \rightarrow N_{2\,(g)} + M - O \text{ (rds, M: metals)}$$

$$M - O_{(ads)} + 2H^+ + 2e^- \rightarrow H_2 \rightarrow M + H_2O \text{ (fast)}$$

Li *et. al.* studied the electrocatalytic N_2ORR on the surface of electrodeposited Pd on glassy carbon electrodes (Pd/GC) in different pH buffer solutions (Figure 1.5) [67]. They concluded that the Pd/GC electrode showed N_2ORR currents after the reduction of the oxide layer, but the N_2ORR currents were found to be poor in acidic electrolyte because the hydrogen adsorption competes with the N_2O adsorption. Because of the lack of such competition in alkaline electrolytes, the same electrode showed efficient N_2ORR activity.

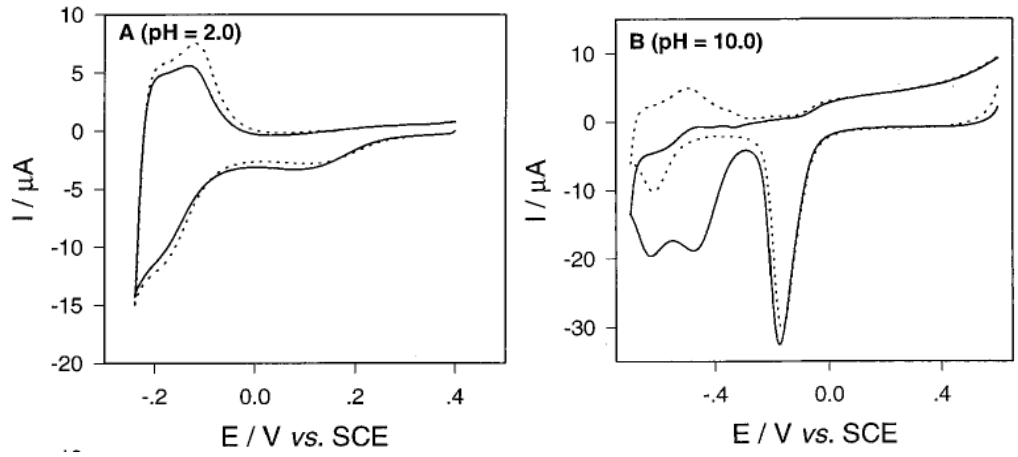


Figure 1.5 Cyclic voltammograms of the Pd/GC electrode in the citrate buffer solution of (A) pH 2.0 and (B) pH 10.0 in the absence (…) and presence (–) of 0.73 mM N_2O solution at a sweep rate of 50 mV s^{-1}. Adapted with permission from ref. [67], copyright 1998, American Chemical Society.

1.3.2 NO_3^- reduction on bimetallic electrodes

Monometallic electrodes are not active enough for electrocatalytic NO_3RR as mentioned above. Therefore, a second metal as a promoter is integrated onto the surfaces of the noble metals, including Pt and Pd to improve their NO_3RR activity [53–62]. When their surfaces are modified with p-block metal adatoms including Sn, the adsorption of NO_3^- increases at Sn/Pt or Sn/Pd interfaces, promoting the rate-determining step of the NO_3^- reduction to NO_2^- (Figure 1.6) [47,53,54,56,57,59,62,72,75]. Sn most likely interacts with one of the oxygen atoms of NO_3^- as it has higher affinity to oxygen than Pt or Pd and the Pt or Pd may interact with nitrogen atom of NO_3^- [72]. It is considered as an accepted general model for improvement of electrochemical NO_3^- reduction [53].

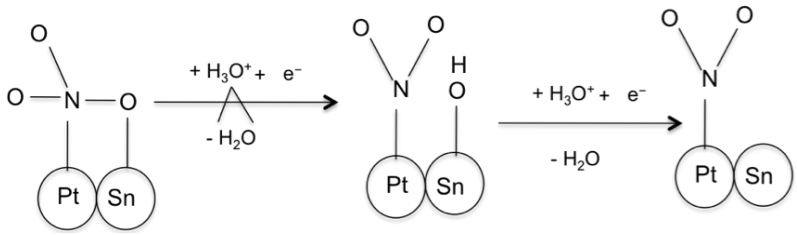


Figure 1.6 Mechanism of electrocatalytic NO_3RR to NO_2^- at the Pt/Sn interface. Adapted with permission from ref. [72], copyright 2004, Elsevier.

Koper *et al.* studied the NO_3RR on polycrystalline Pt electrode modified with p-block metals including Sn in acidic media and identified Sn as the best promoter for enhancing NO_3RR activity with the formation of NO, N_2O, NH_2OH, and NH_3 (Figure 1.7) [53]. Based on the DFT calculations, they reported that the Sn surface alloy, adatoms or oxidized states of Sn species such as $Sn(OH)_x$ on the Pt surface enhanced the adsorption energy of NO_3^- (Table 1.1).

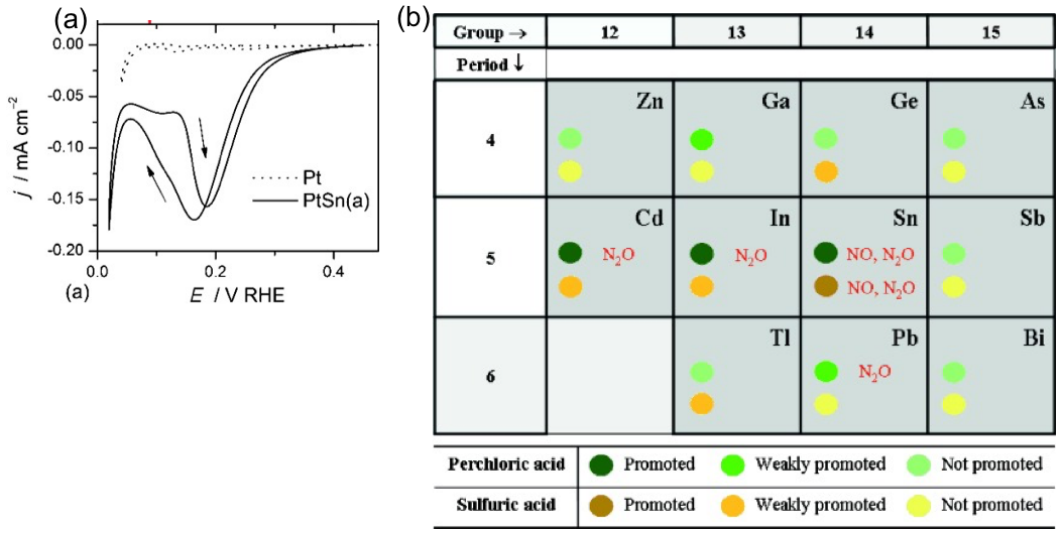


Figure 1.7 (a) Cyclic voltammograms of the bare Pt electrode (dotted line) and Sn-modified Pt electrode (Sn coverage, $\theta_{Sn} \approx 0.337$) (solid line) in an aqueous solution of 0.1 M H_2SO_4 containing 0.01 M $NaNO_3$ under Ar at a sweep rate of 1 mV s^{-1} and (b) the promoting effect and the product distribution along with the sites of Sn and other p-block elements in the periodic table. Adapted with permission from ref. [53], copyright 2013, Wiley-VCH.

Table 1.1 DFT free energies of nitrate adsorption on Pt(111), 50% Sn(surface alloy)–Pt(111), and Pt(111) surfaces with Sn and $Sn(OH)_x$ adatom species [53].

Catalyst	ΔG_{NO3}/eV
Pt(111)	–0.55
50% Sn(surface alloy)–Pt(111)	–0.71
Sn(adatom)/Pt(111)	–0.74
$Sn(OH)_x$(adatom)/Pt(111)	–1.17

Shimazu *et al.* widely investigated Sn-modified Pt and Pd electrodes for NO_3RR in acidic media (0.1 M $HClO_4$+0.01 M $NaNO_3$) [54,72]. Sn-modified Pt electrodes showed the Sn-coverage (θ_{Sn}) dependent NO_3RR activity and at $\theta_{Sn} \approx 0.35$, they showed the maximum NO_3RR current density of –3.6 mA cm^{-2} at –0.1 V vs. Ag|AgCl (sat. KCl) (+0.16 V vs. RHE) [56,72]. On the other hand, Sn-modified Pd electrodes at $\theta_{Sn} \geq 0.65$ showed the maximum NO_3RR current density of –10.3 mA cm^{-2} at –0.1 V vs. Ag|AgCl

(sat. KCl) (+0.16 V vs. RHE) [54,61]. Even this value of NO_3RR current density is the highest among all bimetallic electrodes already reported [54]. However, the Sn-modified Pt and Pd electrodes including other noble metal electrodes have a good ability for N–O bond breaking of NO_3^-, resulting in high NO_3RR activity [61]. Note that the unmodified and Sn-modified Pt and Pd electrodes (Sn/Pt and Sn/Pd) were reported to show almost similar NO_2RR activity in acidic media [76]. This result further supports the rate-determining step of the NO_3^- reduction to NO_2^-.

The products of the Sn-modified Pt and Pd electrodes in acidic media were summarized in Table 1.2, which are NO_2^-, NO, N_2O, N_2, NH_3OH^+, and NH_4^+. Sn-modified Pt electrodes produce a hydrogenated species of NH_3OH^+ (46%) as the main product due to their high N–H bond formation ability and the low N–N bond formation ability, whereas Sn-modified Pd electrodes mainly produce N_2O as the main the product because of having their N–N formation ability and suppression of N–H formation ability [54,58,61,72].

Table 1.2 Distribution of products for NO_3RR on Sn-modified Pt and Pd electrodes.

Electrode	Electrolyte	Experimental conditions	Ionic products	Gaseous products	Detection methods	Ref.
Sn/Pt (thin film), $\theta_{Sn} \approx 0.35$	0.1 M $HClO_4$ + 0.01 M $NaNO_3$	–0.2 V vs. Ag|AgCl (sat. KCl), 5 h	NO_2^- (10%), **NH_3OH^+ (46%),** NH_4^+ (11%)	N_2O (7%), **N_2 (26%)**	[a]DEMS, ion chromatogragy & [b]FIA	[61,72]
Sn/Pt (poly), $\theta_{Sn} \approx 0.41$	0.1 M $HClO_4$ + 0.01 M $NaNO_3$	1 mV s^{-1}, 0.5~0 V vs. RHE	Not investigated	NO, **N_2O (main),** N_2	*In situ* online	[57]
Sn/Pt (poly), $\theta_{Sn} \approx 0.926$				**NO (main)**, N_2O		
Sn/Pt (plate), $\theta_{Sn} \approx 0.23$ & 0.91	0.1 M $HClO_4$ + 0.1 M HNO_3 (or 0.1 M $NaNO_3$)	1 mV s^{-1}, 0.5~0 V vs. RHE	NO_2^-, **NH_3OH^+ (main),** NH_4^+	Not investigated	Ion chromatogragy	[58]
Sn/Pd/Au, $\theta_{Sn} \geq 0.65$	0.1 M $HClO_4$ + 0.01 M $NaNO_3$	–0.2 V vs. Ag|AgCl (sat. KCl), 5 h	NO_2^- (13%), NH_3OH^+ (9%)	**N_2O (78%)**	[a]DEMS, ion chromatogragy & [b]FIA	[54,61]
Sn/Pd/Au, θ_{Sn}: 0.60~0.80	0.1 M H_2SO_4 + 0.1 M HNO_3	1 mV s^{-1}, 0.5~0 V vs. RHE	NH_3OH^+ **(main)** NH_4^+	NO, **N_2O (main),** N_2	*In situ* online & ion chromatogragy	[47]

[a]DEMS refers to differential electrochemical mass spectrometry.

[b]FIA refers to flow injection analysis.

1.3.3 NO_3^- reduction on trimetallic electrodes

As mentioned above, bimetallic electrodes: Sn-modified Pt and Pd electrodes are active for electrocatalytic NO_3RR. To further improve their NO_3RR activity and the product selectivity towards N_2, Pt and Pd are mixed and their surfaces are modified with Sn [46]. Sn-modified PdPt alloy (Sn/PdPt) electrodes, Pd/Pt = 31/69 molar ratio prepared by sputtering method onto the previously sputtered Au on the glass, were investigated for the electrocatalytic NO_3RR in acidic media (0.1 M $HClO_4$+0.01 M $NaNO_3$) (Figure 1.8a) [46]. The Sn/PdPt electrode was found to show higher NO_3RR activity than the bimetallic counterparts of Sn-modified Pt or Pd electrodes (Sn/Pt or Sn/Pd) and the NO_3RR current densities at –0.1 V vs. Ag|AgCl (sat. KCl) (+0.16 vs. RHE) decreased in the following order: Sn/PdPt (–5.1 mA cm^{-2}) > Sn/Pt (–4.1 mA cm^{-2}) > Sn/Pd (–3.6 mA cm^{-2}) (Figure 1.8b) [46]. The clear increase of NO_3RR activity at the Sn/PdPt electrode is attributed to the synergetic effect of Pt and Pd [43,46,75]. Next, the products of NO_3RR at the electrodes have been discussed.

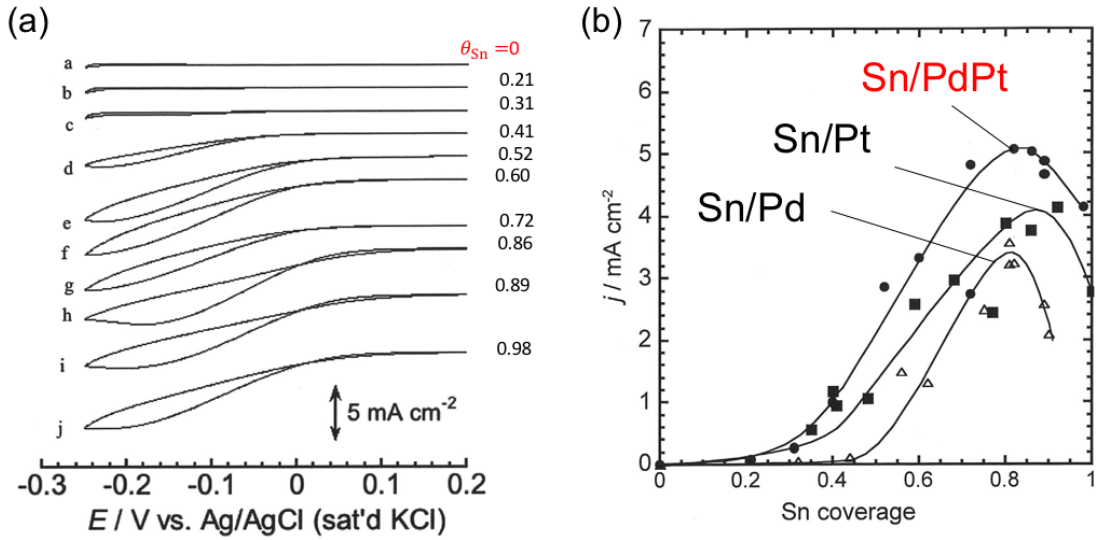


Figure 1.8 (a) Cyclic voltammograms of Sn/PdPt electrodes with different Sn coverages (θ_{Sn}) for NO_3RR in an aqueous solution of 0.1 M $HClO_4$ containing 0.01 M $NaNO_3$ under Ar at a sweep rate of 10 mV s^{-1} and (b) Sn coverage dependence of the NO_3RR current density at –0.1 V vs. Ag/AgCl (sat. KCl) (+0.16 V vs. RHE). Adapted with permission from ref. [46], copyright 2020, Elsevier.

For the product distribution of NO_3RR at Sn/Pt, Sn/Pd, and Sn/PdPt electrodes, 5 h electrolysis at –0.2 V vs. Ag|AgCl (sat. KCl) in an aqueous 0.1 M $HClO_4$+0.01 M $NaNO_3$ solution was performed [46]. The Sn/PdPt electrode produced a higher amount of N_2 (44%) than Sn/Pt (N_2, 32%) and Sn/Pd (N_2, 28%). In addition, the amount of hydrogenated products (NH_3OH^++ NH_4^+, ca. 26 %) at the Sn/PdPt electrode was found to be lower than that at the Sn/Pt electrode (ca. 36 %), and the amount of N_2O (ca. 25%) at the Sn/PdPt electrode was lower than that (ca. 29 %) at Sn/Pd electrode, resulting in the high amount of N_2 at the Sn/PdPt electrode. It was concluded that the N–H bond formation ability (hydrogenation ability) of the Sn/Pt electrode decreased and the N–O bond cleavage ability of the Sn/Pd electrode increased in the Sn/PdPt electrode. Thus, the maximum formation of N_2 (44%) was achieved at the Sn/PdPt electrode.

In a reverse system, Pt nanoparticle (NP)-modified fluorine-doped tin oxide (FTO) substrate electrodes (Pt/FTO) were investigated for electrocatalytic NO_3RR in acidic media (Figure 1.9) [62]. Note that Pt NPs with different pulse numbers were prepared by an arc-plasma deposition (APD) method. It was concluded that the Pt/Sn interface of the Pt/FTO electrodes acts as the catalytic active site for NO_3RR, as the Pt NPs on glassy carbon substrates (Pt/GC) showed almost no such activity.

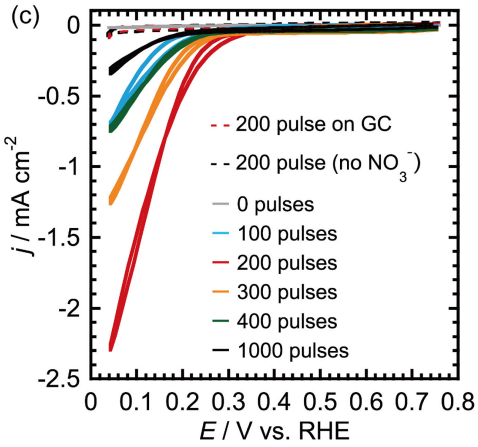


Figure 1.9 Cyclic voltammograms of the Pt NPs with different pulse number on fluorine-doped tin oxide (FTO) substrate electrodes (Pt/FTO) in an aqueous solution of 0.1 M $HClO_4$ containing 0.01 M $NaNO_3$ under Ar at a sweep rate of 10 mV s^{-1}. Adapted with permission from ref. [62], The Electrochemical Society of Japan.

1.3.4 NO_3^- reduction on single crystalline electrodes

Surface structure and composition of electrode materials play an important role in electrocatalytic NO_3RR activity and product selectivity. Based on the high NO_3RR activity of the Sn-modified Pt and Pd polycrystalline electrodes, Sn-modified single-crystalline electrodes: Pt(111), Pt(100), Pd(111), PdPt(111) (3 wt% Pd), and PdPt(100) (3 wt% Pd) were investigated for NO_3RR in acidic media (0.1 M $HClO_4$+0.1 M $NaNO_3$) (Figure 1.10) [75]. The unmodified single-crystalline electrodes showed almost no NO_3RR activity, whereas the modification of their surfaces with Sn improved NO_3RR activity. The NO_3RR activity order decreased in the following order: Sn/PdPt(100) > Sn/PdPt(111) > Sn/Pt(100) > Sn/Pd(111) ≈ Sn/Pt(111). At +0.16 V vs. RHE, the Sn/PdPt(100) showed NO_3RR current density of –12.4 mA cm^{-2}, which was higher than the maximum NO_3RR current density of –10.3 mA cm^{-2} +0.16 V vs. RHE on Sn-modified Pd thin film electrode [54]. From XPS observation, it was concluded that the Sn^0 was deposited on the (100) surfaces, whereas Sn^{2+} was on (111) surfaces. Thus, the Sn alloy formation on the PdPt(100) surface and the combination of these metals modulate the adsorption ability of NO_3^-, resulting in the high NO_3RR activity. The gaseous product selectivity on the Sn-modified (100) surfaces has been discussed in the next.

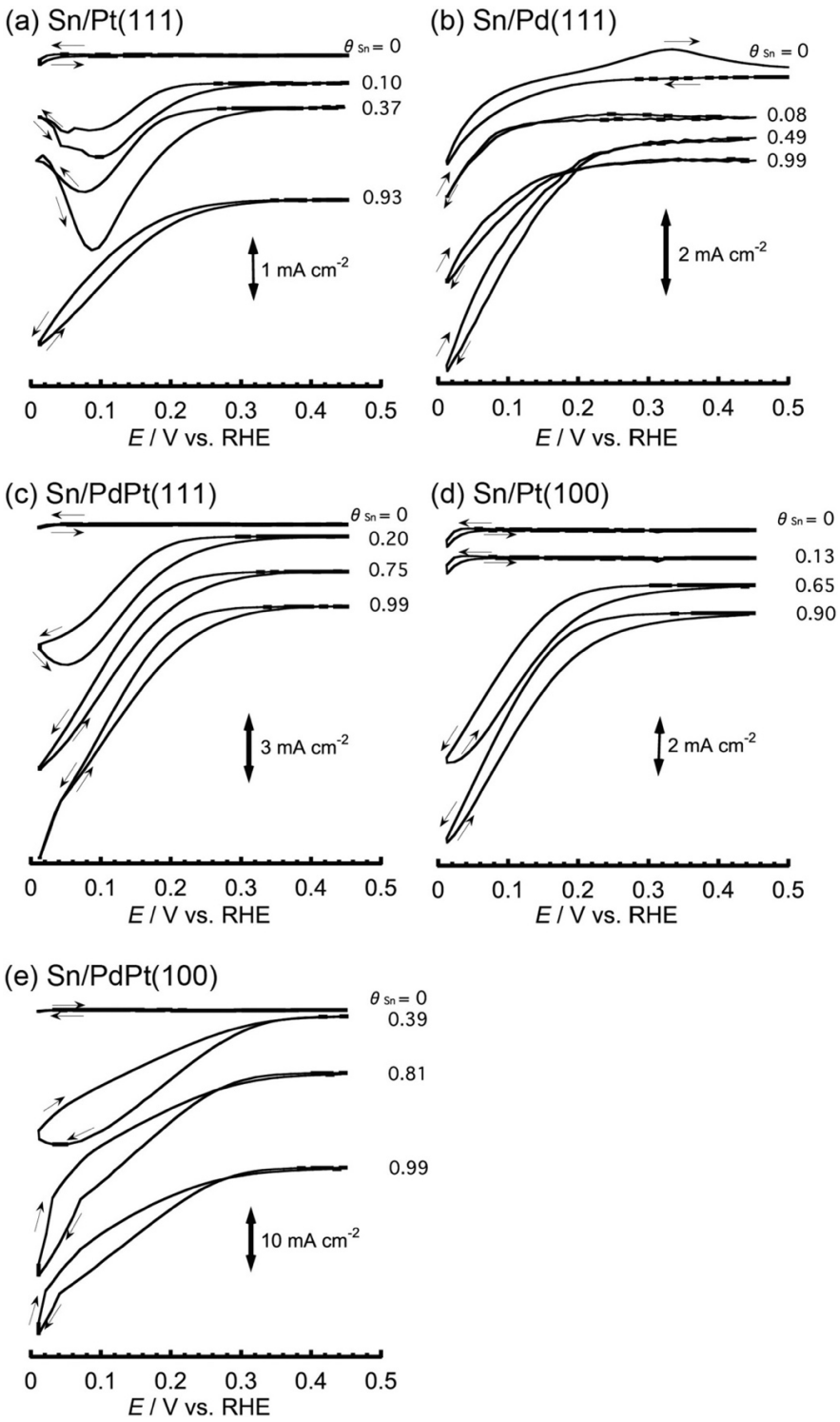


Figure 1.10 (a) Cyclic voltammograms for NO_3RR on Sn-modified Pt and PdPt (3 wt% Pd) alloy single crystalline electrodes in an aqueous solution of 0.1 M $HClO_4$ containing 0.1M $NaNO_3$ under Ar at a sweep rate of 10 mV s^{-1}. Adapted with permission from ref. [75], copyright 2017, Elsevier.

The gaseous products of the Sn/Pt(100), Sn/Pd(100), and Sn/PdPt(100) electrodes for NO_3RR were reported in acidic media (0.1 M $HClO_4$+0.1 M $NaNO_3$) [36]. On Sn/Pt(100), NO and N_2O were identified as volatile products with a Faradaic efficiency of ca. 25%, indicating the NH_3 and NH_2OH as non-volatile products. On the other hand, Sn/Pd(100), and Sn/PdPt(100) produced not only NO and N_2O but also N_2. The total Faradaic efficiency of these gaseous products was ca. 92 % at +0.2 V vs. RHE, in which the N_2 was 34 %. It was concluded that the Pd(100) surface proceeds with the reduction of NO to N_2 rather than the formation of non-volatile products. The most important conclusion was that the PdPt(100) had a weaker affinity with H-adatoms than Pt(100) and thus, the modulation of H-adsorption energy for metal alloys would be a key to the selective N_2 production.

1.4 Objective of this thesis

Previous studies have shown that the high NO_3RR activity can be achieved at trimetallic Sn-modified PdPt alloy (Sn/PdPt) electrodes when compared the bimetallic counterparts of Sn-modified Pt or Pd electrodes (Sn/Pt or Sn/Pd) and these electrodes were not studied for N_2ORR. In a reverse system, Pt nanoparticle (NP)-modified fluorine-doped tin oxide (FTO) substrate electrodes (Pt/FTO) were studied for NO_3RR, in which the Pt/Sn interface acts as the catalytic active site. However, most of the studies for NO_3RR have been done on Sn-modified noble metal electrodes. The same electrode was not investigated for the reduction of NO_3^- and its potential by-products: NO_2^-, NO, and N_2O.

The objective of this thesis is to expand the investigation on (i) the reverse system: (Pt+Pd) mixture NP-modified FTO electrodes and (ii) chemically synthesized Sn-containing Pt-Pd NP electrodes for NO_3RR, NO_2RR, NORR, and N_2ORR. Firstly, the (Pt+Pd)/FTO electrodes were optimized with Pt:Pd = 3:2 atomic ratio by an arc-plasma deposition (APD) method for NO_3RR, and the optimized electrode was investigated for NO_2RR, NORR, and N_2ORR to understand the role of the PtPd/Sn interface. As this is a model study, further Pt–Pd–Sn NPs with the optimized Pt:Pd = 3:2 atomic ratio were synthesized by a wet chemical method and immobilized on carbon support to investigate the electrocatalytic reduction of the most potential by-product N_2O obtained from NO_3RR. Finally, Pd nanocubes (NCs) and Sn-modified Pd NCs were studied for electrocatalytic N_2ORR to understand the role of surface structure.

1.5 Outline of this thesis

The main body of this thesis includes five chapters.

Chapter 1 described the background for efficient NO_3^- and N_2O removal, NO_3^- and N_2O removal technologies, advantages of electrocatalytic NO_3^- and N_2O removal technologies, and previous studies on electrocatalytic NO_3RR and N_2ORR, objective and outline of this thesis.

Chapter 2 described the preparation of the Pt and/or Pd NPs on fluorine-doped tin oxide (FTO) electrodes: Pt/FTO, Pd/FTO, and Pt/Pd/FTO by an arc-plasma deposition (APD) method and the advantageous of this method. The electrodes were characterized by cyclic voltammetry (CV), transmission electron microscopy (TEM), and X-ray photoelectron spectroscopy (XPS). The Pt/FTO and Pd/FTO electrodes were optimized for electrocatalytic NO_3RR with respect to the pulse number of Pt and Pd. Keeping the same optimized pulse number, Pt/Pd/FTO electrodes were prepared by changing Pt–to–Pd pulse ratios and optimized for electrocatalytic NO_3RR. Then, the NO_3RR activities of the optimized Pt/FTO, Pd/FTO, and Pt/Pd/FTO electrodes were compared and the optimized Pt/Pd/FTO electrode with Pt:Pd = 3:2 atomic ratio was identified as the best for NO_3RR. The presence of the trimetallic PtPd/Sn interface in the optimized Pt/Pd/FTO electrode was confirmed by TEM, scanning transmission electron microscopy (STEM), and energy dispersive spectroscopy (EDS) mapping images, and XPS. Then, the optimized Pt/Pd/FTO and Pt/Pd/glassy carbon (GC) electrodes were investigated for the reduction of each potential intermediates of NO_3RR: NO_2^-, NO, and N_2O in acidic media to understand the role of the PtPd/Sn interface.

Chapter 3 described the preparation of Pt–Sn NPs, and Pt–Pd–Sn NPs according to the optimized Pt:Pd = 3:2 atomic ratio obtained from the APD method, immobilization of the NPs on a carbon support, and their characterization by TEM, STEM, EDS mapping, X-ray powder diffraction (XRD), and CV. The carbon-supported Pt–Sn and Pt–Pd–Sn NPs were investigated for N_2ORR in acidic media and their catalytic activities were compared. The presence of the Pt/Sn and PtPd/Sn interfaces was confirmed by TEM, STEM, EDS mapping images, and XPS. The products obtained from N_2ORR were detected and quantified by gas chromatography, and the results were discussed.

Chapter 4 described the preparation of Pd nanocubes (NCs) on a carbon support and their characterization by TEM and CV, modification of their surfaces with Sn. Electrocatalytic activities of the unmodified and Sn-modified Pd NCs were investigated for N_2ORR in acidic media to understand the role of surface structure at Pd/Sn interfaces. The results were discussed.

In **Chapter 5**, the summary of this thesis and conclusions were described. The future prospect of the thesis for electrocatalytic NO_3RR and N_2ORR was also mentioned.

1.6 References

[1] D.E. Canfield, A.N. Glazer, P.G. Falkowski, The evolution and future of earth's nitrogen cycle, Science. 330 (2010) 192–196. https://doi.org/10.1126/science.1186120.

[2] M.E. A. Scheidleder, J. Grath, G. Winkler, U. Stärk, C. Koreimann, C. Gmeiner, S. Nixon, J. Casillas, P. Gravesen, J. Leonard, Groundwater quality and quantity in Europe, Eur. Environ. Agency. (1999) 1–123. https://www.eea.europa.eu/publications/TEC22.

[3] C.J. Johnson, B.C. Kross, Continuing importance of nitrate contamination of groundwater and wells in rural areas, Am. J. Ind. Med. 18 (1990) 449–456. https://doi.org/10.1002/ajim.4700180416.

[4] R.R. Jones, P.J. Weyer, C.T. Dellavalle, M. Inoue-Choi, K.E. Anderson, K.P. Cantor, S. Krasner, K. Robien, L.E. Beane Freeman, D.T. Silverman, M.H. Ward, Nitrate from drinking water and diet and bladder cancer among postmenopausal women in Iowa, Environ. Health Perspect. 124 (2016) 1751–1758. https://doi.org/10.1289/EHP191.

[5] H. Tian, R. Xu, J.G. Canadell, R.L. Thompson, W. Winiwarter, P. Suntharalingam, E.A. Davidson, P. Ciais, R.B. Jackson, G. Janssens-Maenhout, M.J. Prather, P. Regnier, N. Pan, S. Pan, G.P. Peters, H. Shi, F.N. Tubiello, S. Zaehle, F. Zhou, A. Arneth, G. Battaglia, S. Berthet, L. Bopp, A.F. Bouwman, E.T. Buitenhuis, J. Chang, M.P. Chipperfield, S.R.S. Dangal, E. Dlugokencky, J.W. Elkins, B.D. Eyre, B. Fu, B. Hall, A. Ito, F. Joos, P.B. Krummel, A. Landolfi, G.G. Laruelle, R. Lauerwald, W. Li, S. Lienert, T. Maavara, M. MacLeod, D.B. Millet, S. Olin, P.K. Patra, R.G. Prinn, P.A. Raymond, D.J. Ruiz, G.R. van der

Werf, N. Vuichard, J. Wang, R.F. Weiss, K.C. Wells, C. Wilson, J. Yang, Y. Yao, A comprehensive quantification of global nitrous oxide sources and sinks, Nature. 586 (2020) 248–256. https://doi.org/10.1038/s41586-020-2780-0.

[6] K. Parris, Impact of agriculture on water pollution in OECD countries: Recent trends and future prospects, Int. J. Water Resour. Dev. 27 (2011) 33–52. https://doi.org/10.1080/07900627.2010.531898.

[7] Y.Y. Yang, G.S. Toor, Sources and mechanisms of nitrate and orthophosphate transport in urban stormwater runoff from residential catchments, Water Res. 112 (2017) 176–184. https://doi.org/10.1016/j.watres.2017.01.039.

[8] N. HANLEY, The economics of nitrate pollution, Eur. Rev. Agric. Econ. 17 (1990) 129–151. https://doi.org/10.1093/erae/17.2.129.

[9] M. Strokal, C. Kroeze, Nitrous oxide (N2O) emissions from human waste in 1970-2050, Curr. Opin. Environ. Sustain. 9 (2014) 108–121. https://doi.org/10.1016/j.cosust.2014.09.008.

[10] A.A. Avery, Infantile Methemoglobinemia: Reexamining the Role of Drinking Water Nitrates, Environ. Health Perspect. 107 (1999) 583–586. https://doi.org/10.1289/ehp.99107583.

[11] Nitrate and Nitrite in Drinking-water Background Document for Development of WHO Guidelines for Drinking-water Quality, World Health Organization, 2016. https://cdn.who.int/media/docs/default-source/wash-documents/wash-chemicals/nitrate-nitrite-background-jan17.pdf?sfvrsn=1c1e1502_4.

[12] E. Abascal, L. Gómez-Coma, I. Ortiz, A. Ortiz, Global diagnosis of nitrate pollution in groundwater and review of removal technologies, Sci. Total Environ. 810 (2022) 152233. https://doi.org/10.1016/j.scitotenv.2021.152233.

[13] M.H. Ward, R.R. Jones, J.D. Brender, T.M. de Kok, P.J. Weyer, B.T. Nolan, C.M. Villanueva, S.G. van Breda, Drinking water nitrate and human health: An updated review, Int. J. Environ. Res. Public Health. 15 (2018) 1–31. https://doi.org/10.3390/ijerph15071557.

[14] Z. Zhou, N. Ansems, P. Torfs, A Global Assessment of Nitrate Contamination in Groundwater, Int. Groundw. Resour. Assess. Cent. (2015) 1–27.

[15] Guidelines for Drinking-water Quality, World Health Organization, 4th ed., 2011. https://doi.org/10.1007/978-1-4020-4410-6_184.

[16] Drinking Water Quality Standards in Japan, Ministry of Health, Labor and

Welfare, Japan, 2015.
www.mhlw.go.jp/english/policy/health/water_supply/dl/4a.pdf.

[17] O. Badr, S.D. Probert, Nitrous Oxide in the Earth's Atmosphere, Appl. Energy. 41 (1992) 177–200. https://doi.org/10.1016/0306-2619(92)90002-S.

[18] M. Konsolakis, Recent Advances on Nitrous Oxide (N2O) Decomposition over Non-Noble-Metal Oxide Catalysts: Catalytic Performance, Mechanistic Considerations, and Surface Chemistry Aspects, ACS Catal. 5 (2015) 6397–6421. https://doi.org/10.1021/acscatal.5b01605.

[19] Drawing Down N2O to Protect Climate and the Ozone Layer: A UNEP synthesis report, 2013. https://wedocs.unep.org/20.500.11822/8489.

[20] R.L. Thompson, L. Lassaletta, P.K. Patra, C. Wilson, K.C. Wells, A. Gressent, E.N. Koffi, M.P. Chipperfield, W. Winiwarter, E.A. Davidson, H. Tian, J.G. Canadell, Acceleration of global N2O emissions seen from two decades of atmospheric inversion, Nat. Clim. Chang. 9 (2019) 993–998. https://doi.org/10.1038/s41558-019-0613-7.

[21] Ed Dlugokencky, Trends in atmospheric nitrous oxide, National Oceanic and Atmospheric Administration/Global Monitoring Laboratory, (2022). gml.noaa.gov/ccgg/trends_n2o/ (accessed May 7, 2022).

[22] A.R. Ravishankara, J.S. Daniel, R.W. Portmann, Nitrous oxide (N2O): The dominant ozone-depleting substance emitted in the 21st century, Science (80-.). 326 (2009) 123–125. https://doi.org/10.1126/science.1176985.

[23] J.C. López, G. Quijano, T.S.O. Souza, J.M. Estrada, R. Lebrero, R. Muñoz, Biotechnologies for greenhouse gases (CH4, N2O, and CO2) abatement: State of the art and challenges, Appl. Microbiol. Biotechnol. 97 (2013) 2277–2303. https://doi.org/10.1007/s00253-013-4734-z.

[24] K. Kim, J. Byun, H. Kim, K.S. Lee, H.S. Lee, J. Kim, T. Hyeon, J.J. Kim, J.W. Han, Systematic Approach to Designing a Highly Efficient Core–Shell Electrocatalyst for N2O Reduction, ACS Catal. 11 (2021) 15089–15097. https://doi.org/10.1021/acscatal.1c03832.

[25] V. Urbain, Nitrate removal from drinking water—review, J. Environ. Eng. (United States). 124 (1998) 903–903. https://doi.org/10.1061/(ASCE)0733-9372(1998)124:9(903).

[26] M. Duca, M.T.M. Koper, Powering denitrification: The perspectives of

electrocatalytic nitrate reduction, Energy Environ. Sci. 5 (2012) 9726–9742. https://doi.org/10.1039/c2ee23062c.

[27] S.G. Lehman, M. Badruzzaman, S. Adham, D.J. Roberts, D.A. Clifford, Perchlorate and nitrate treatment by ion exchange integrated with biological brine treatment, Water Res. 42 (2008) 969–976. https://doi.org/10.1016/j.watres.2007.09.011.

[28] D. Clifford, X. Liu, Ion exchange for nitrate removal, J. / Am. Water Work. Assoc. 85 (1993) 135–143. https://doi.org/10.1002/j.1551-8833.1993.tb05971.x.

[29] J.J. Schoeman, A. Steyn, Nitrate removal with reverse osmosis in a rural area in South Africa, Desalination. 155 (2003) 15–26. https://doi.org/10.1016/S0011-9164(03)00235-2.

[30] A. El Midaoui, F. Elhannouni, M. Taky, L. Chay, M.A. Menkouchi Sahli, L. Echihabi, M. Hafsi, Optimization of nitrate removal operation from ground water by electrodialysis, Sep. Purif. Technol. 29 (2002) 235–244. https://doi.org/10.1016/S1383-5866(02)00092-8.

[31] G. Chen, Electrochemical technologies in wastewater treatment, Sep. Purif. Technol. 38 (2004) 11–41. https://doi.org/10.1016/j.seppur.2003.10.006.

[32] S. Vasudevan, F. Epron, J. Lakshmi, S. Ravichandran, S. Mohan, G. Sozhan, Removal of NO3- from drinking water by electrocoagulation - An alternate approach, Clean - Soil, Air, Water. (2010). https://doi.org/10.1002/clen.200900226.

[33] M. Kobune, D. Takizawa, J. Nojima, R. Otomo, Y. Kamiya, Catalytic reduction of nitrate in water over alumina-supported nickel catalyst toward purification of polluted groundwater, Catal. Today. 352 (2020) 204–211. https://doi.org/10.1016/j.cattod.2020.01.037.

[34] H. Xu, Y. Ma, J. Chen, W. Zhang, J. Yang, Electrocatalytic reduction of nitrate – a step towards a sustainable nitrogen cycle, Chem. Soc. Rev. 51 (2022) 2710–2758. https://doi.org/10.1039/d1cs00857a.

[35] Z. Wang, D. Richards, N. Singh, Recent discoveries in the reaction mechanism of heterogeneous electrocatalytic nitrate reduction, Catal. Sci. Technol. 11 (2021) 705–725. https://doi.org/10.1039/d0cy02025g.

[36] M. Kato, Y. Unuma, M. Okui, Y. Qu, J. Zheng, S. Taguchi, F. Kiguchi, M. Torihata, Y. Gao, N. Hoshi, I. Yagi, Electrocatalytic activity and volatile product

selectivity for nitrate reduction at tin-modified Pt(100), Pd(100) and Pd–Pt(100) single crystal electrodes in acidic media, Electrochim. Acta. 398 (2021) 139281. https://doi.org/10.1016/j.electacta.2021.139281.

[37] M. Galle, D.W. Agar, O. Watzenberger, Thermal N2O decomposition in regenerative heat exchanger reactors, Chem. Eng. Sci. 56 (2001) 1587–1595. https://doi.org/10.1016/S0009-2509(00)00386-9.

[38] G. Centi, F. Vazzana, Selective catalytic reduction of N2O in industrial emissions containing O2, H2O and SO2: Behavior of Fe/ZSM-5 catalysts, Catal. Today. 53 (1999) 683–693. https://doi.org/10.1016/S0920-5861(99)00155-8.

[39] A. Wang, Y. Wang, E.D. Walter, R.K. Kukkadapu, Y. Guo, G. Lu, R.S. Weber, Y. Wang, C.H.F. Peden, F. Gao, Catalytic N2O decomposition and reduction by NH3 over Fe/Beta and Fe/SSZ-13 catalysts, J. Catal. 358 (2018) 199–210. https://doi.org/10.1016/j.jcat.2017.12.011.

[40] X. Xu, H. Xu, F. Kapteijn, J.A. Moulijn, SBA-15 based catalysts in catalytic N2O decomposition in a model tail-gas from nitric acid plants, Appl. Catal. B Environ. 53 (2004) 265–274. https://doi.org/10.1016/j.apcatb.2004.04.023.

[41] A. Kudo, A. Mine, Electrocatalysis for N2O reduction on metal electrodes, J. Electroanal. Chem. 408 (1996) 267–269. https://doi.org/10.1016/0022-0728(96)04630-X.

[42] M. Kato, M. Okui, S. Taguchi, I. Yagi, Electrocatalytic nitrate reduction on well-defined surfaces of tin-modified platinum, palladium and platinum-palladium single crystalline electrodes in acidic and neutral media, J. Electroanal. Chem. 800 (2017) 46–53. https://doi.org/10.1016/j.jelechem.2017.01.020.

[43] J.F.E. Gootzen, P.G.J.M. Peeters, J.M.B. Dukers, L. Lefferts, W. Visscher, J.A.R. Van Veen, The electrocatalytic reduction of NO-3 on Pt, Pd and Pt + Pd electrodes activated with Ge, J. Electroanal. Chem. 434 (1997) 171–183. https://doi.org/10.1016/S0022-0728(97)00093-4.

[44] J. Souza-Garcia, E.A. Ticianelli, V. Climent, J.M. Feliu, Nitrate reduction on Pt single crystals with Pd multilayer, Electrochim. Acta. 54 (2009) 2094–2101. https://doi.org/10.1016/j.electacta.2008.08.059.

[45] G.E. Dima, A.C.A. De Vooys, M.T.M. Koper, Electrocatalytic reduction of nitrate at low concentration on coinage and transition-metal electrodes in acid solutions, J. Electroanal. Chem. 554–555 (2003) 15–23. https://doi.org/10.1016/S0022-

0728(02)01443-2.

[46] M.M. Hossain, T. Kawaguchi, K. Shimazu, K. Nakata, Reduction of nitrate on tin-modified palladium-platinum electrodes, J. Electroanal. Chem. 864 (2020) 114041. https://doi.org/10.1016/j.jelechem.2020.114041.

[47] Y.Y. Birdja, J. Yang, M.T.M. Koper, Electrocatalytic reduction of nitrate on tin-modified palladium electrodes, Electrochim. Acta. 140 (2014) 518–524. https://doi.org/10.1016/j.electacta.2014.06.011.

[48] van V.J.A.R. de Vooys, A. C.A., van Santen, R.A., Electrocatalytic reduction of NO3- on palladium/copper electrodes, J. Mol. Catal. A Chem. 154 (2000) 203–215. https://doi.org/10.1007/978-3-319-61112-9_2.

[49] S. Garcia-Segura, M. Lanzarini-Lopes, K. Hristovski, P. Westerhoff, Electrocatalytic reduction of nitrate: Fundamentals to full-scale water treatment applications, Appl. Catal. B Environ. 236 (2018) 546–568. https://doi.org/10.1016/j.apcatb.2018.05.041.

[50] V. Rosca, M. Duca, M.T. DeGroot, M.T.M. Koper, Nitrogen Cycle Electrocatalysis, Chem. Rev. 109 (2009) 2209–2244. https://doi.org/10.1021/cr8003696.

[51] S. Taguchi, J.M. Feliu, Electrochemical reduction of nitrate on Pt(S)[n(1 1 1) × (1 1 1)] electrodes in perchloric acid solution, Electrochim. Acta. 52 (2007) 6023–6033. https://doi.org/10.1016/j.electacta.2007.03.057.

[52] M.C. Figueiredo, J. Solla-Gullón, F.J. Vidal-Iglesias, V. Climent, J.M. Feliu, Nitrate reduction at Pt(1 0 0) single crystals and preferentially oriented nanoparticles in neutral media, Catal. Today. 202 (2013) 2–11. https://doi.org/10.1016/j.cattod.2012.02.038.

[53] J. Yang, F. Calle-Vallejo, M. Duca, M.T.M. Koper, Electrocatalytic reduction of nitrate on a Pt electrode modified by p-block metal adatoms in acid solution, ChemCatChem. 5 (2013) 1773–1783. https://doi.org/10.1002/cctc.201300075.

[54] K. Shimazu, R. Goto, S. Piao, R. Kayama, K. Nakata, Y. Yoshinaga, Reduction of nitrate ions on tin-modified palladium thin film electrodes, J. Electroanal. Chem. 601 (2007) 161–168. https://doi.org/10.1016/j.jelechem.2006.11.005.

[55] Y.Y. Birdja, J. Yang, M.T.M. Koper, Electrocatalytic reduction of nitrate on tin-modified palladium electrodes, Electrochim. Acta. 140 (2014) 518–524. https://doi.org/10.1016/j.electacta.2014.06.011.

[56] K. Shimazu, R. Goto, K. Tada, Electrochemical reduction of nitrate ions on tin-modified platinum and palladium electrodes, Chem. Lett. 31 (2002) 204–205. https://doi.org/10.1246/cl.2002.204.

[57] J. Yang, M. Duca, K.J.P. Schouten, M.T.M. Koper, Formation of volatile products during nitrate reduction on a Sn-modified Pt electrode in acid solution, J. Electroanal. Chem. 662 (2011) 87–92. https://doi.org/10.1016/j.jelechem.2011.03.015.

[58] J. Yang, Y. Kwon, M. Duca, M.T.M. Koper, Combining voltammetry and ion chromatography: Application to the selective reduction of nitrate on Pt and PtSn electrodes, Anal. Chem. 85 (2013) 7645–7649. https://doi.org/10.1021/ac401571w.

[59] M. Motahar Hossain, K. Nakata, T. Kawaguchi, K. Shimazu, Reduction of nitrate on electrochemically pre-reduced tin-modified palladium electrodes, J. Electroanal. Chem. 707 (2013) 59–65. https://doi.org/10.1016/j.jelechem.2013.08.015.

[60] O. Ghodbane, M. Sarrazin, L. Roué, D. Bélanger, Electrochemical Reduction of Nitrate on Pyrolytic Graphite-Supported Cu and Pd–Cu Electrocatalysts, J. Electrochem. Soc. 155 (2008) F117. https://doi.org/10.1149/1.2900094.

[61] S. Piao, Y. Kayama, Y. Nakano, K. Nakata, Y. Yoshinaga, K. Shimazu, Nitrate reduction on tin-modified rhodium, ruthenium, and iridium electrodes, J. Electroanal. Chem. 629 (2009) 110–116. https://doi.org/10.1016/j.jelechem.2009.01.031.

[62] M. Kato, A. Araki, Y. Hara, S. Taguchi, I. Yagi, Cathodic arc-plasma deposition of platinum nanoparticles on fluorine-doped tin oxide for electrocatalytic nitrate reduction reaction, Electrochemistry. 86 (2018) 220–222. https://doi.org/10.5796/electrochemistry.18-00031.

[63] A. Kudo, A. Mine, Electrocatalytic reduction of nitrous oxide on metal and oxide electrodes in aqueous solution, Appl. Surf. Sci. 121–122 (1997) 538–542. https://doi.org/10.1016/S0169-4332(97)00362-0.

[64] A. Ahmadi, E. Bracey, R. Wyn Evans, G. Attard, Anion-surface interactions. Part II. Nitrous oxide reduction as a probe of anion adsorption on transition metal surfaces, J. Electroanal. Chem. 350 (1993) 297–316. https://doi.org/10.1016/0022-0728(93)80212-Z.

[65] A. Aziznia, A. Bonakdarpour, E.L. Gyenge, C.W. Oloman, Electroreduction of nitrous oxide on platinum and palladium: Toward selective catalysts for methanol-nitrous oxide mixed-reactant fuel cells, Electrochim. Acta. 56 (2011) 5238–5244. https://doi.org/10.1016/j.electacta.2011.03.023.

[66] H. Ebert, R. Parsons, G. Ritzoulis, T. VanderNoot, The reduction of nitrous oxide on platinum electrodes in acid solution, J. Electroanal. Chem. 264 (1989) 181–193. https://doi.org/10.1016/0022-0728(89)80156-1.

[67] B. Wang, X.Y. Li, Electrocatalytic Properties of Nitrous Oxide and Its Voltammetric Detection at Palladium Electrodeposited on a Glassy Carbon Electrode, Anal. Chem. 70 (1998) 2181–2187. https://doi.org/10.1021/ac970601h.

[68] A.K. Vijh, Electrocatalysis of the electroreduction of nitric acid by metals, J. Catal. 32 (1974) 230–236. https://doi.org/10.1016/0021-9517(74)90071-2.

[69] O.A. Petrii, T.Y. Safonova, Electroreduction of nitrate and nitrite anions on platinum metals: A model process for elucidating the nature of the passivation by hydrogen adsorption, J. Electroanal. Chem. 331 (1992) 897–912. https://doi.org/10.1016/0022-0728(92)85013-S.

[70] G.E. Dima, V. Rosca, M.T.M. Koper, Role of germanium in promoting the electrocatalytic reduction of nitrate on platinum: An FTIR and DEMS study, J. Electroanal. Chem. 599 (2007) 167–176. https://doi.org/10.1016/j.jelechem.2005.12.005.

[71] J. Lim, C.Y. Liu, J. Park, Y.H. Liu, T.P. Senftle, S.W. Lee, M.C. Hatzell, Structure Sensitivity of Pd Facets for Enhanced Electrochemical Nitrate Reduction to Ammonia, ACS Catal. 11 (2021) 7568–7577. https://doi.org/10.1021/acscatal.1c01413.

[72] K. Tada, K. Shimazu, Kinetic studies of reduction of nitrate ions at Sn-modified Pt electrodes using a quartz crystal microbalance, J. Electroanal. Chem. 577 (2005) 303–309. https://doi.org/10.1016/j.jelechem.2004.11.039.

[73] K. Nishimura, K. Machida, M. Enyo, On-line mass spectroscopy applied to electroreduction of nitrite and nitrate ions at porous Pt electrode in sulfuric acid solutions, Electrochim. Acta. 36 (1991) 877–880. https://doi.org/10.1016/0013-4686(91)85288-I.

[74] A.C.A. De Vooys, M.T.M. Koper, R.A. Van Santen, J.A.R. Van Veen, Mechanistic study on the electrocatalytic reduction of nitric oxide on transition-

metal electrodes, J. Catal. 202 (2001) 387–394. https://doi.org/10.1006/jcat.2001.3275.

[75] M. Kato, M. Okui, S. Taguchi, I. Yagi, Electrocatalytic nitrate reduction on well-defined surfaces of tin-modified platinum, palladium and platinum-palladium single crystalline electrodes in acidic and neutral media, J. Electroanal. Chem. 800 (2017) 46–53. https://doi.org/10.1016/j.jelechem.2017.01.020.

[76] K. Nakata, Y. Doi, S. Kubota, K. Shimazu, Reduction of nitrite on tin-modified noble metal electrodes, J. Electroanal. Chem. 647 (2010) 187–193. https://doi.org/10.1016/j.jelechem.2010.06.003.

Chapter 2

Electrocatalytic Nitrate and Nitrous Oxide Reduction at Interfaces Between Pt-Pd Nanoparticles and Fluorine-Doped Tin Oxide

Reproduced in part with permission from "*Electrochim. Acta* 425 (**2022**) 140628"
DOI: https://doi.org/10.1016/j.electacta.2022.140628

2.1 Introduction

Various electrocatalysts such as noble metals [1–5], binary metals [6–15], and ternary metals [16–19] have been already studied for the electrocatalytic NO_3RR. Generally, single metal electrodes including Pt and Pd are known to show poor electrocatalytic NO_3RR activity because of low NO_3^- adsorption energy as compared with hydrogen [3,20,21]. The modification of their surfaces with p-block metal adatoms significantly increases NO_3^- adsorption, leading to the acceleration of the rate-determining step of the NO_3^- reduction to NO_2^- [6–9,12,15,19,22]. For example, the surface modification of Pt and Pd electrodes with Sn enhances the NO_3RR activity, and the Sn/Pt and Sn/Pd interfaces act as the active sites, respectively. For the NO_2^- reduction reaction (NO_2RR), both Sn-modified and unmodified Pt and Pd electrodes were found to be active [22]. For the NO reduction reaction (NORR) and N_2O reduction reaction (N_2ORR), the role of the Sn/Pt and Sn/Pd interfaces in the activity enhancement remains unclear. For trimetallic electrodes, Sn-modified PdPt alloy (Sn/PdPt) electrodes have been studied only for the NO_3RR and show higher NO_3RR activity than the bimetallic counterparts of Sn-modified Pt or Pd electrodes, and the enhancement of N–O bond cleavage of NO_3^- including N_2O and the suppression of N–H bond formation at the Sn/PdPt electrode increases the N_2 formation with decreasing the formation of NH_4^+ and NH_3OH^+ [16]. In a reverse system, Pt nanoparticle (NP)-modified fluorine-doped tin oxide (FTO) electrodes (Pt/FTO) were also found to be active for electrocatalytic NO_3RR, in which the Pt/Sn interface plays an important role [15]. However, there is a lack of detailed investigations on reverse systems of Pt and/or Pd NPs on FTO for the electrocatalytic NO_3RR, NO_2RR, NORR, and N_2ORR, even though these systems have interfaces between Pt and/or Pd and Sn.

Herein, we report the electrocatalytic activity of Pt and/or Pd NP-deposited FTO electrodes for the NO_3RR in acidic media. The role of the PtPd/Sn interface was investigated in not only the NO_3RR but also the reduction of potential by-products: NO_2^-, NO, and N_2O. Three different electrodes of Pt and/or Pd NPs were prepared on FTO substrates: Pt/FTO, Pd/FTO, and Pt/Pd/FTO by an arc-plasma deposition (APD) method under high vacuum conditions. The APD method enables the direct deposition of metal NPs on the substrates by changing the number of pulses for controlling the amount of metal NPs. This method requires no multi-step preparation for the removal of surfactants or the impregnation processes, which are needed in solution-based methods [23]. Using the APD method, the deposited amounts of Pt and/or Pd NPs on FTO substrates were optimized for the NO_3RR to their pulse number, and then the NO_2RR, NORR, and N_2ORR activity of the optimized electrode was investigated to understand the role of the PtPd/Sn interface.

2.2 Experimental

2.2.1 Materials

Acetone, 2-propanol, 30% hydrogen peroxide, 28% ammonia, and 60% perchloric acid were purchased from Wako Pure Chemical Industries, Ltd. Sodium nitrate and sodium nitrite were purchased from Kanto Chemical Co., Inc. Nitric oxide (NO) in Ar (50%) and nitrous oxide (N_2O, 99.5%) were purchased from Tomoe Shokai and GL Science, respectively. FTO glass sheets were purchased from SPD Laboratory, Inc.

2.2.2 Electrode preparation

A commercial FTO glass sheet was cut into small pieces with 1.5 cm × 1.5 cm. The FTO substrates were cleaned in 2-propanol, acetone, and then Milli-Q water under ultrasonication for 20 min each, kept in the mixture of 30% H_2O_2–28% NH_3–Milli-Q water (1:1:5, v/v/v) at 343 K for 1 h, rinsed with Milli-Q water, and then dried under N_2. Pt/FTO and Pd/FTO electrodes were prepared by the deposition of Pt and Pd NPs, respectively, on the FTO substrates at room temperature in the vacuum deposition chamber (Ulvac, MUE-ECO-EV) with ca. 10^{-3} Pa by using coaxial pulsed APD systems (ADVANCE RIKO, ARL-300) [23], in which cylindrical Pt and Pd cathodes were used as sources for Pt and Pd NPs, respectively. The APD of Pt and/or Pd was performed at an arc voltage of 100 V and a condenser capacity of 1080 μF. The APD pulses ranging from 10 to 300 pulses were set to control the amount of Pt and Pd NPs deposited on the FTO substrates, which were

placed ca. 7 cm away from the Pt and Pd cathodes. To prepare Pt/Pd/FTO electrodes, Pt and Pd were sequentially deposited on FTO substrates with 30 pulses changing Pt-to-Pd pulse ratio (Pt_x/Pd_{30-x}/FTO, where x (pulse number) = 5, 10, 15, 20, 25). Because almost no effect of the sequential APD order on the NO_3RR activity and particle size was confirmed by electrochemical measurements and TEM images, the experimental data of Pt_x/Pd_{30-x}/FTO are shown and discussed in this work.

2.2.3 Electrochemical measurements

All cyclic voltammograms (CVs) were recorded using a conventional three-electrode, one compartment electrochemical cell by a potentiostat HZ-5000 (Hokuto Denko Corp.). Pt and/or Pd NPs on FTO substrates were used as working electrodes, and a platinized Pt foil and an Ag|AgCl (sat. KCl) were used as the counter and the reference electrodes, respectively. The geometrical surface area of the working electrode was 0.95 cm^2. Before using, all glassware was immersed in the mixture of 1:1 concentrated nitric and sulfuric acid overnight, rinsed by and boiled in Milli-Q water, and then ultrasonicated. Before measurements of CVs, the electrolyte solution was purged with Ar (99.999%, Hokkaido Air Water Inc.) for at least 30 min. Pt/FTO electrodes were electrochemically cleaned in the potential range between –0.2 and +1.1 V vs. Ag|AgCl (sat. KCl) at a sweep rate of 50 mV s^{-1} until getting stable CVs in 0.1 M $HClO_4$ aqueous solution, and the Faradaic charges of hydrogen desorption were used to determine the electrochemically active surface area of Pt ($ECSA_{Pt}$) on FTO substrates. Pd/FTO electrodes were also electrochemically cleaned in 0.1 M $HClO_4$ aqueous solution between +0.1 and +1.1 V vs. Ag|AgCl (sat. KCl) at a sweep rate of 50 mV s^{-1} until getting stable CVs and the Faradaic charge of PdO_x reduction were used to determine the electrochemically active surface area of Pd ($ECSA_{Pd}$) on FTO substrates. For electrochemical NO_3^- reduction, CVs were recorded in 0.1 M $HClO_4$ aqueous solution containing 0.01 M $NaNO_3$ at a sweep rate of 10 mV s^{-1}. In the case of electrochemical NO_2^- reduction, 0.0345 g of $NaNO_2$ was added to deaerated 0.1 M $HClO_4$ aqueous solution (50 mL) to make 0.01 M $NaNO_2$ solution just before recording CVs. To investigate the NO electrochemical reduction, a 0.1 M $HClO_4$ aqueous solution was saturated with bubbling of NO gas for 30 min. In this case, NO gas was passed through a 1.0 M NaOH aqueous solution, which removes NO_x, followed by Milli-Q water before being introduced to the electrochemical cell. For electrochemical N_2O reduction, a 0.1 M $HClO_4$ aqueous solution in the electrochemical cell was saturated

with bubbling of N_2O gas for 30 min. The first cycle of the CVs was always used for making a graph in presence of the analyte. All potentials shown were converted to be versus the reversible hydrogen electrode (RHE) by using the following equation: E (vs. RHE) = E (vs. Ag|AgCl (sat. KCl)) + 0.199 + 0.059 × pH.

2.2.4 Physicochemical characterizations

X-ray photoelectron spectroscopy (XPS) data were collected at the pass energy of 10 eV using an Al Kα X-ray source by a photoelectron spectrometer JPS-9200 (JEOL). The C=C peak in the C 1s region was used as an internal standard (284.7 eV) to calibrate the binding energies of the elements. Carbon tape was used to make FTO substrates conductive with the sample holder of XPS, which gave a peak in the C 1s region. Transmission electron microscopy (TEM) images were obtained by JEM-2000FX (JEOL) at an acceleration voltage of 200 kV. Scanning transmission electron microscopy (STEM) and energy dispersive spectroscopy (EDS) elemental mapping images were obtained by JEM-ARM200F (JEOL) at 200 kV. For TEM, STEM, and EDS observations, Pt and/or Pd NPs were deposited on silicon oxide grids (ALLIANCE Biosystems) to ensure a similar oxide surface to the FTO substrate.

2.3 Results and discussion

2.3.1 Characterization of Pt/FTO and Pd/FTO electrodes

To characterize Pt on FTO electrodes with a different number of APD pulses (Pt_x/FTO, where x indicates the number of APD pulses), CVs of Pt_x/FTO were recorded at a sweep rate of 50 mV s^{-1} in a 0.1 M $HClO_4$ aqueous solution under Ar (Figure 2.1a). Hydrogen adsorption/desorption currents were observed in the potential range between +0.06 and +0.34 V vs. RHE. PtO_x reduction peaks were observed in the potential range between +0.72 and +0.76 V vs. RHE [24]. No such peaks were observed on bare FTO electrodes (gray broken line in Figure 2.1a), suggesting the deposition of Pt on FTO. The deposition of Pt NPs was confirmed by TEM observation of model samples of APD–Pt NPs with 30 pulses on a silicon oxide grid (Figure 2.1b). A surface density and an averaged diameter of APD–Pt NPs were determined to be 7.1×10^{12} cm^{-2} and 2.2 nm, respectively (Figure 2.1c), which is quite close to that previously reported for APD–Pt NPs [15]. For the APD–Pt NPs with 100 pulses, a surface density and an averaged diameter of them were determined to be 9.3×10^{12} cm^{-2} and 2.5 nm, respectively (Figures 2.2a and 2.2b). These

results reveal that the surface density of Pt NPs increases with keeping the almost same particle diameter as the number of APD pulses increases. Similar results were reported in a previous study [15]. The APD–Pt NPs with 200 pulses or more gave almost no individual NP, indicating the agglomeration of Pt NPs (Figure. 2.2c).

The electrochemically active surface area of Pt ($ECSA_{Pt}$) of Pt_x/FTO was calculated using the following equation: $ECSA_{Pt} = Q_H/210\ \mu C\ cm^{-2}$, where Q_H indicates the Faradaic charges for the hydrogen desorption at the Pt_x/FTO electrodes and 210 $\mu C\ cm^{-2}$ corresponds to the Faradaic charge density for the monolayer of the underpotentially deposited hydrogen on the smooth Pt surface [24]. The $ECSA_{Pt}$ was plotted against the number of APD pulses (Figure 2.3a). The $ECSA_{Pt}$ of Pt_x/FTO electrodes increases as the number of Pt pulses increases. The $ECSA_{Pt}$ was found to reach a plateau at around 200 Pt pulses due to the formation of a fully covered Pt film on the FTO substrates. A similar plateau region was observed in a previous study on APD–Pt/GC (GC = glassy carbon) electrodes [15]. Based on the $ECSA_{Pt}$ in the plateau region ($ECSA_{Pt,\ max}$), Pt coverages (θ_{Pt}) on FTO can be defined by the following equation: $\theta_{Pt} = ECSA_{Pt}/ECSA_{Pt,\ max}$.

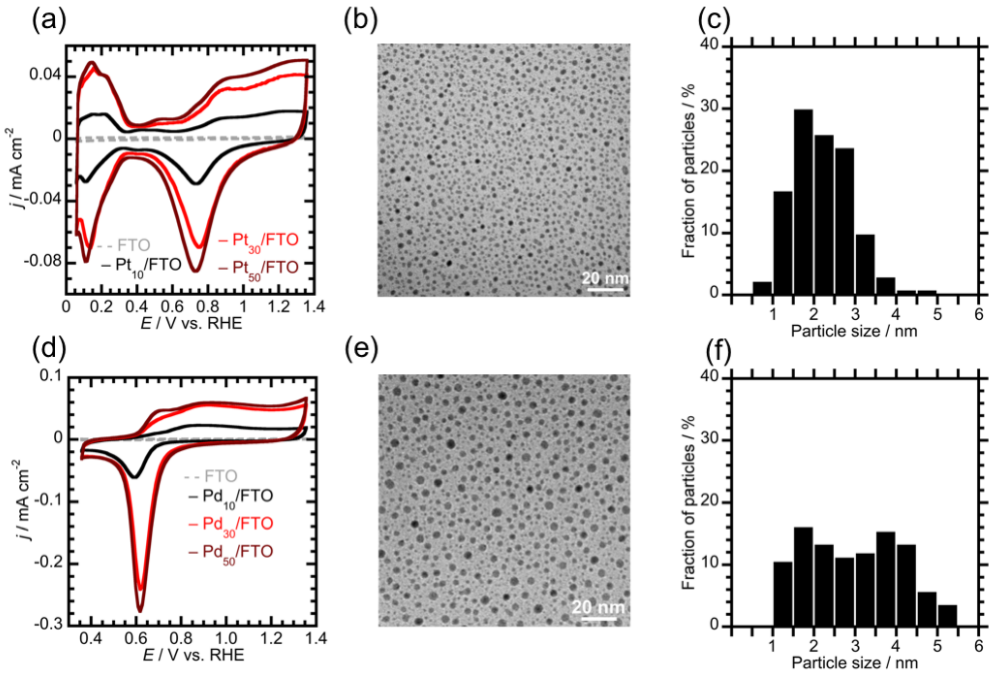


Figure 2.1 (a) CVs of Pt_x/FTO electrodes in a 0.1 M $HClO_4$ aqueous solution at a sweep rate of 50 mV s^{-1} under Ar. (b) TEM image of APD–Pt NPs with 30 pulses on a silicon oxide grid and (c) the histogram of the size distribution of Pt NPs. (d) CVs of Pd_x/FTO electrodes in a 0.1 M $HClO_4$ aqueous solution at a sweep rate of 50 mV s^{-1} under Ar. (e) TEM image of APD–Pd NPs with 30 pulses on a silicon oxide grid and (f) the histogram of the size distribution of Pd NPs.

CVs of FTO electrodes modified with Pd with a different number of APD pulses (Pd_x/FTO, where *x* indicates the number of APD pulses) were recorded at 50 mV s^{-1} in the potential range between +0.36 and +1.36 V vs. RHE in 0.1 M $HClO_4$ aqueous solution under Ar (Figure 2.1d). A reduction peak was observed in the potential range between +0.59 and +0.67 V vs. RHE, which can be associated with the reduction of PdO_x [25,26]. No such peak was observed at the bare FTO electrode (gray dashed line in Figure 2.1d). Thus, the deposition of APD–Pd was confirmed on FTO. TEM observation enabled us to determine a Pd NP density and an average diameter to be 3.5×10^{12} cm^{-2} and 3.0 nm for 30 pulses (Figures 2.1e and 2.1f) and 3.4×10^{12} cm^{-2} and 3.5 nm for 100 pulses (Figures 2.2d and 2.2e), respectively. Note that increasing the pulse number up to 100 causes almost no change of the Pd NP density but an increase in Pd NP diameter. This trend is different from that of APD-Pt NPs, as mentioned above. The particle size distribution of APD-Pd NPs (Figure 2.1f) is wider than that of APD-Pt NPs (Figure 2.1c). These results imply that Pd NPs tend to agglomerate on the substrate and/or deposit on Pd NPs already placed on the substrate, whereas Pt NPs tend to individually deposit on the substrate and be less sensitive to agglomeration.

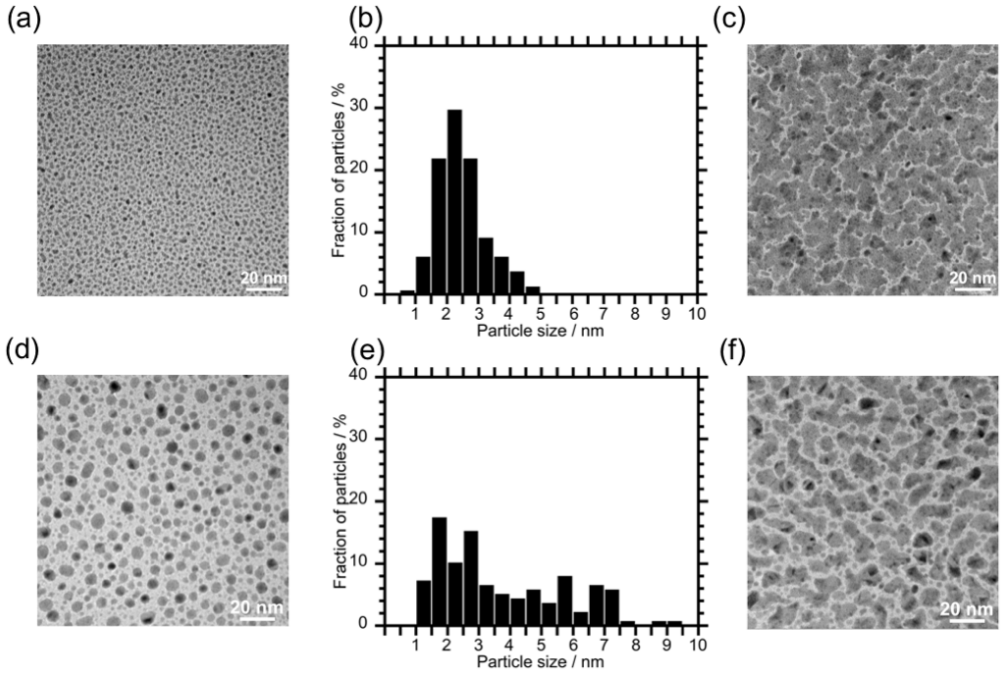


Figure 2.2 TEM images of APD–Pt NPs with (a) 100 pulses and (c) 200 pulses on silicon oxide grids. (b) The histogram of the Pt NPs' size distribution for 100 pulses produced from (a). TEM images of APD–Pd NPs with (d) 100 pulses and (f) 200 pulses on silicon oxide grids. (e) The histogram of the Pd NPs' size distribution for 100 pulses produced from (d).

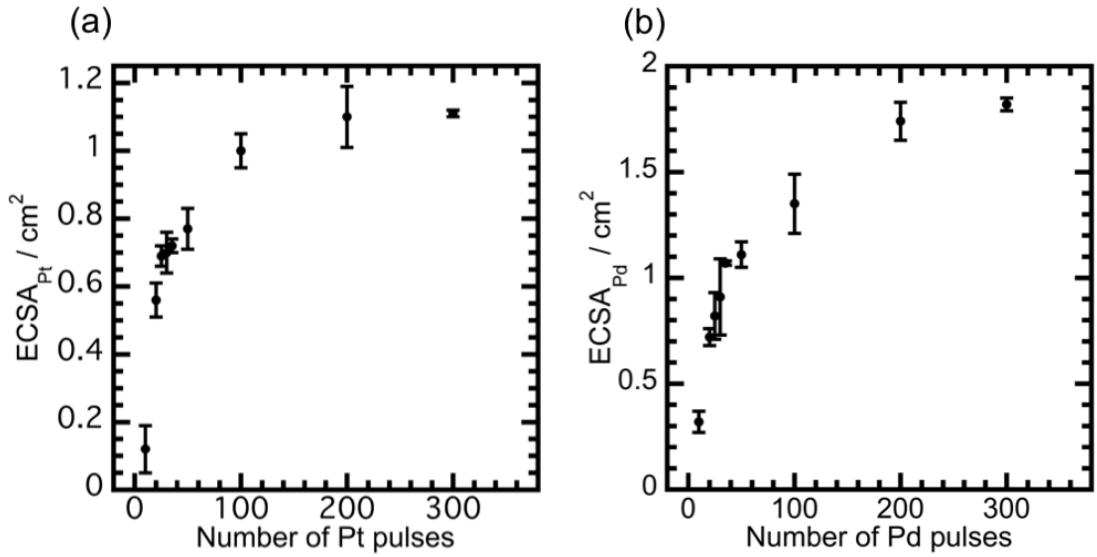


Figure 2.3 The plots of ECSA of (a) Pt on Pt_x/FTO electrodes and (b) Pd on Pd_x/FTO electrodes as a function of the number of Pt and Pd pulses, respectively.

ECSAs of Pd ($ECSA_{Pd}$) on Pd_x/FTO electrodes were determined based on the Faradaic charges for the reduction wave of the surface oxide film in the following equation: $ECSA_{Pd} = Q_{oxide}/424\ \mu C\ cm^{-2}$, where Q_{oxide} indicates the Faradaic charges for the oxide reduction at Pd_x/FTO electrodes and 424 μC cm^{-2} corresponds to the assumed Faradaic charge density for the reduction of surface PdO monolayer on a smooth Pd surface [25]. The $ECSA_{Pd}$ is determined based on the Faradaic charge for the reduction of the surface oxide film, not for the hydrogen adsorption or desorption, because both hydrogen adsorption and absorption occur at the Pd electrode in the same potential range from +0.025 to +0.375 V vs. RHE and they are difficult to be separated [25–28]. The $ECSA_{Pd}$ was plotted against the number of APD pulses (Figure 2.3b). The plateau region seems to start at around 300 Pd pulses. Thus, Pd coverages (θ_{Pd}) on the FTO substrates were determined based on the $ECSA_{Pd}$ in the plateau region ($ECSA_{Pd,\,max}$).

2.3.2 Optimizing NO_3RR at Pt/FTO and Pd/FTO electrodes

CVs of Pt_x/FTO electrodes were recorded in 0.1 M $HClO_4$ aqueous solution containing 0.01 M $NaNO_3$ under Ar (Figure 2.4a). All Pt_x/FTO electrodes showed cathodic currents in the potential range from +0.06 to +0.34 V vs. RHE only in the solution containing NO_3^-. These currents can be associated with the electrochemical NO_3RR [6,9,15,19,22]. The NO_3RR current densities of Pt_x/FTO electrodes at +0.16 V vs. RHE

were plotted against θ_{Pt} in Figure 2.4c [29]. The cathodic current density for the NO_3RR reached the maximum at $\theta_{Pt} \approx 0.63$ (corresponding to Pt_{30}/FTO), which is in good agreement with a previous study [15]. Sn-modified Pt electrodes previously showed the maximum current density for the NO_3RR at a tin coverage of $\theta_{Sn} \approx 0.35$ (–3.6 mA cm^{-2} at +0.16 V vs. RHE) [9], which is almost the same as $\theta_{Sn} \approx 0.37$ (the residual of $\theta_{Pt} \approx 0.63$) for the Pt_{30}/FTO electrode in this work. Thus, the Pt/Sn interface acts as the active site not only for the electrocatalytic NO_3RR in Sn-modified Pt electrodes but also in the reverse system of Pt_x/FTO [10,29]. The formation of the Pt/Sn interface modifies the electronic state of Pt, supported by XPS (Figure 2.5). Pt 4f peaks at Pt_{30}/FTO shifted to the lower binding energy than those at Pt_{30}/GC (Figure 2.5a and Table 2.1). These results suggest the charge transfer from Sn in FTO to Pt. Note that no clear binding energy shift was observed in the Sn 3d region (Table 2.2) because many Sn species of FTO show no direct interaction with Pt NPs, whereas most of Pt NPs interact with Sn species of FTO.

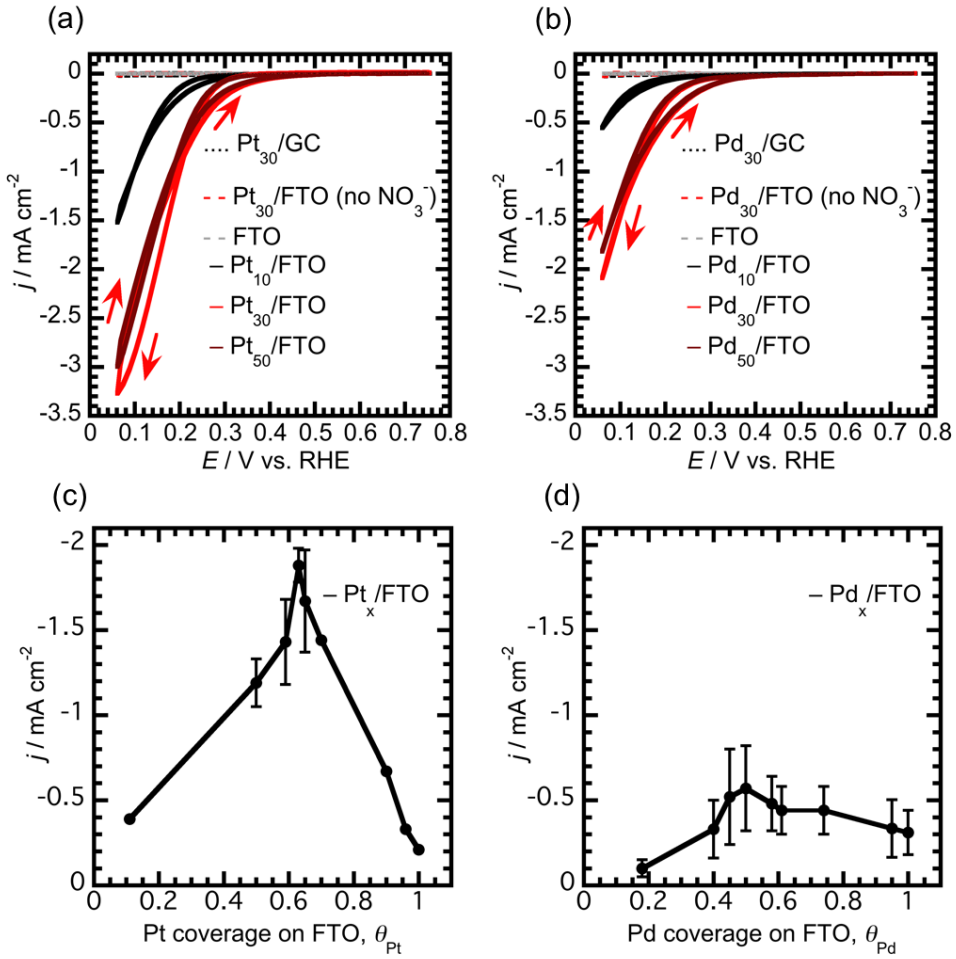


Figure 2.4 CVs of (a) Pt_x/FTO and (b) Pd_x/FTO electrodes in a 0.1 M $HClO_4$ aqueous solution containing 0.01 M $NaNO_3$ at 10 mV s^{-1} under Ar. The plots of (c) Pt and (d) Pd coverage-dependent current density for the NO_3RR at +0.16 V vs. RHE.

Pd_x/FTO electrodes also showed the NO_3RR activity (Figure 2.4b). The cathodic current densities for the NO_3RR at +0.16 V vs. RHE were plotted against θ_{Pd} (Figure 2.4d). The reduction current density increased with increasing θ_{Pd} up to $\theta_{Pd} \approx 0.50$ (corresponding to Pd_{30}/FTO) and then remained almost constant. Since no plateau region is observed for Pt_x/FTO (Figure 2.4c), the θ_{Pd} dependence of Pd_x/FTO on the NO_3RR activity is different from the θ_{Pt} dependence of Pt_x/FTO. This difference could be related to the difference in the APD process between Pt and Pd as mentioned above: the agglomeration tendency of Pd NPs but not in the case of Pt NPs during ADP process (See Section 3.1). The Pd_{30}/FTO electrode with $\theta_{Pd} \approx 0.50$ showed the highest electrocatalytic NO_3RR current density of ca. –0.57 mA cm^{-2} at +0.16 V vs. RHE in the Pd_x/FTO electrodes and the charge transfer from Sn to Pd was confirmed by the comparison of XPS data of Pd_{30}/FTO with Pd_{30}/GC in the Pd 3d region (Figure 2.5b and Tables 2.1).

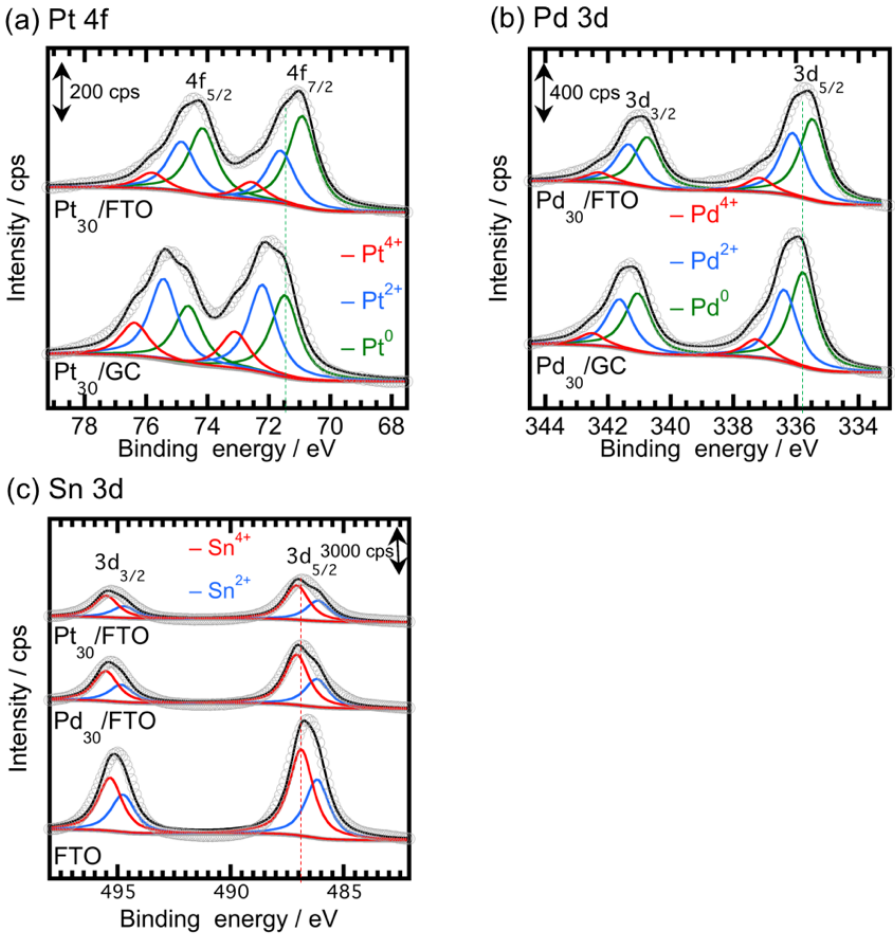


Figure 2.5 XPS of (a) Pt_{30}/FTO and Pt_{30}/GC electrodes in the Pt 4f region, (b) Pd_{30}/FTO and Pd_{30}/GC electrodes in the Pd 3d region, and (c) Pt_{30}/FTO, Pd_{30}/FTO, and FTO electrodes in the Sn 3d region. Experimental data (open circles), the sum of the deconvoluted data (solid line in black), and baseline (in gray).

Table 2.1 The results of peak deconvolution analysis of the XP Pt 4f peaks and XP Pd 3d peaks in Figures 2.5a and 2.5b.

Electrode	Peak position of XPS Pt $4f_{5/2}$ and Pd $3d_{3/2}$			Peak position of XPS Pt $4f_{7/2}$ and Pd $3d_{5/2}$		
	Pt^{4+}	Pt^{2+}	Pt^{0}	Pt^{4+}	Pt^{2+}	Pt^{0}
Pt_{30}/FTO	75.8	74.8	74.2	72.6	71.6	70.9
Pt_{30}/GC	76.4	75.4	74.6	73.1	72.2	71.5
	Pd^{4+}	Pd^{2+}	Pd^{0}	Pd^{4+}	Pd^{2+}	Pd^{0}
Pd_{30}/FTO	342.4	341.4	340.8	337.1	336.1	335.5
Pd_{30}/GC	342.5	341.6	341.0	337.3	336.4	335.8

Table 2.2 The results of peak deconvolution analysis of the XP Sn 3d spectra in Figure 2.5c.

Electrode	Peak position of XPS Sn $3d_{3/2}$		Peak position of XPS Sn $3d_{5/2}$	
	Sn^{4+}	Sn^{2+}	Sn^{4+}	Sn^{2+}
Pt_{30}/FTO	495.5	494.7	487.1	486.1
Pd_{30}/FTO	495.6	494.9	487.2	486.3
FTO	495.3	494.7	486.9	486.2

The Pt_{30}/FTO electrode with $\theta_{Pt} \approx 0.63$ showed greater activity for the NO_3RR than the Pd_{30}/FTO electrode with $\theta_{Pd} \approx 0.50$ (Figure 2.4), indicating that the Pt/Sn interface more efficiently catalyzes the NO_3RR than the Pd/Sn interface. A similar activity trend for the NO_3RR was reported in a previous study on Sn-modified noble metals: Sn-modified Pt electrodes showed higher NO_3RR activity than Sn-modified Pd electrodes [16]. Although the charge densities of Pt and Pd are modulated by charge transfer from Sn, the activity difference between Pt_{30}/FTO and Pd_{30}/FTO can be explained by the intrinsic difference between NO_3^- adsorption energies on Pt and Pd: NO_3^- adsorption energy on Pt surface (–2.23 eV) was reported to be higher than that on Pd surface (–2.14 eV) [30].

2.3.3 NO_3RR at Pt/Pd/FTO electrodes

For a ternary metallic system, Pt and Pd NPs were deposited on FTO substrates by the APD with 30 pulses changing Pt–to–Pd–pulses ratios (Pt_x/Pd_{30-x}/FTO, where x (pulse number) = 5, 10, 15, 20, 25). The total pulse number is based on the optimized pulse number for the bimetallic systems of Pt_{30}/FTO and Pd_{30}/FTO. The Pt_{15}/Pd_{15}/FTO electrode showed the highest NO_3RR activity of –2.24 mA cm^{-2} at +0.16 V vs. RHE in the Pt_x/Pd_{30-x}/FTO electrodes (Figure 2.6). In the following text, the optimized ternary and binary metallic electrodes of Pt_{15}/Pd_{15}/FTO, Pt_{30}/FTO, and Pd_{30}/FTO prepared by the APD method are referred as to Pt/Pd/FTO, Pt/FTO, and Pd/FTO, respectively.

The optimized ternary metallic electrode shows higher NO_3RR activity than the binary metallic electrodes: the order of NO_3RR activity was found as follows: Pt/Pd/FTO > Pt/FTO > Pd/FTO (Figure 2.6a). Similar results have also been reported for Sn-modified PdPt electrodes [16,19]. TEM, STEM, and EDS mapping images of Pt/Pd (Pt_{15}/Pd_{15}) on silicon oxide grids confirmed a particle density of 7.5×10^{12} cm^{-2} with an average diameter of 2.3 nm and the co-presence of Pt and Pd as a mixture in NPs with an atomic ratio to 3:2 (Figure 2.7). Furthermore, a Pt/Pd/GC (Pt_{15}/Pd_{15}/GC) electrode as a control sample showed almost no activity for the NO_3RR (Figure 2.6b). Thus, the ternary metallic PtPd/Sn interface of Pt/Pd/FTO plays an important role in the high NO_3RR activity.

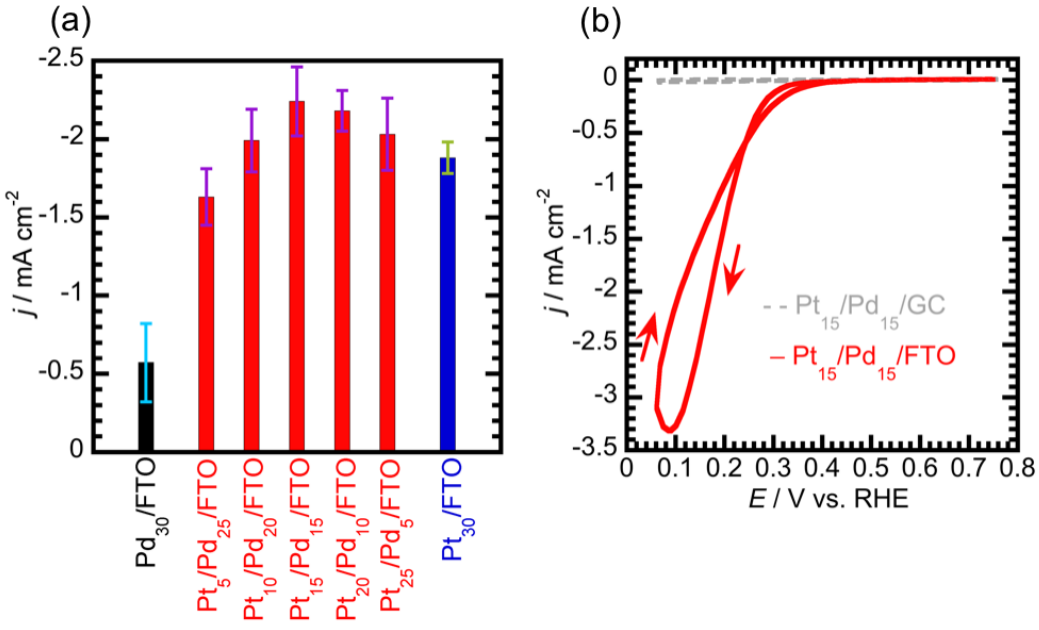


Figure 2.6 (a) Bar graph of current densities for the NO_3RR at +0.16 V vs. RHE shown by Pt_{30}/FTO, Pd_{30}/FTO, and Pt_x/Pd_{30-x}/FTO electrodes in their CVs. (b) CVs of Pt_{15}/Pd_{15}/GC (Pt/Pd/GC) and Pt_{15}/Pd_{15}/FTO (Pt/Pd/FTO) electrodes in 0.1 M $HClO_4$ aqueous solution containing 0.01 M $NaNO_3$ at a sweep rate of 10 mV s^{-1} under Ar.

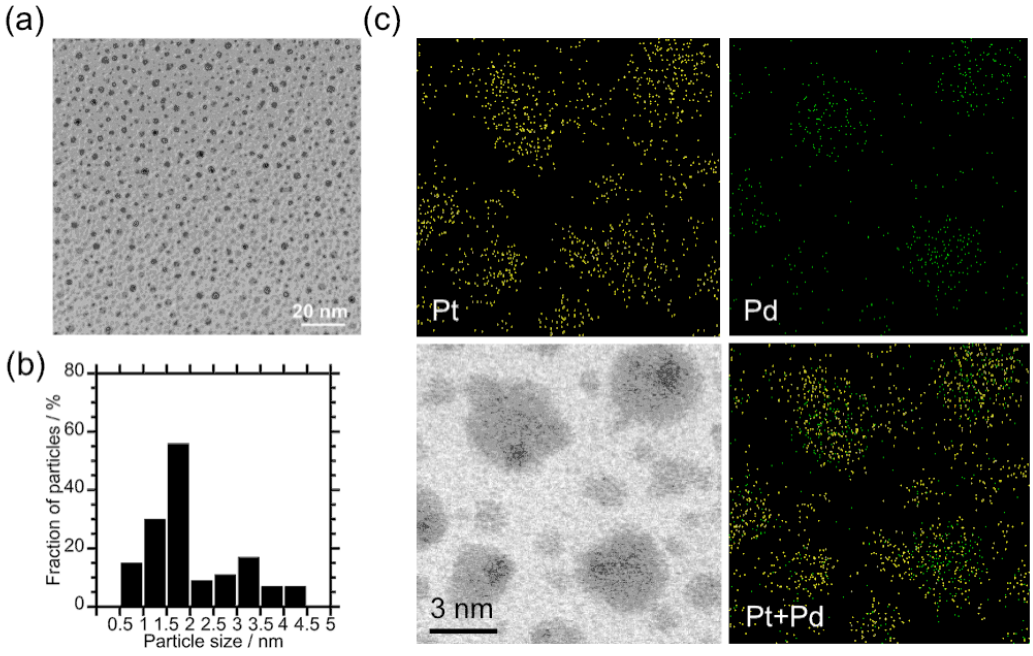


Figure 2.7 (a) TEM image, (b) size distribution, and (c) STEM image and EDS mapping of Pt/Pd NPs (Pt_{15}/Pd_{15}) on a silicon oxide grid. The yellow and green color images indicate the Pt and Pd elements, respectively.

The Pt/Pd/FTO electrode showed cathodic currents for the NO_3RR in the potential region between +0.06 and +0.34 V vs. RHE (Figure 2.6b). In this potential region, the adsorption of NO_3^- competes with the hydrogen adsorption (Figure 2.8) [3,20,30]. The formation of the PtPd/Sn interface could enhance the NO_3^- adsorption and/or suppress the hydrogen adsorption [19], and then accelerate the rate-determining step of the NO_3^- reduction to NO_2^- [11,17,18]. This explanation can be supported by the observation of the charge transfer from Sn to Pt and Pd for the Pt/Pd/FTO like the binary metallic systems: lower binding energy shifts than Pt/Pd/GC in the Pt 4f and Pd 3d regions (Figure 2.9, and Tables 2.3 and 2.4). Thus, the ternary metallic PtPd/Sn interface enables us to finely tune the adsorption ability of NO_3^-, resulting in the high NO_3RR activity.

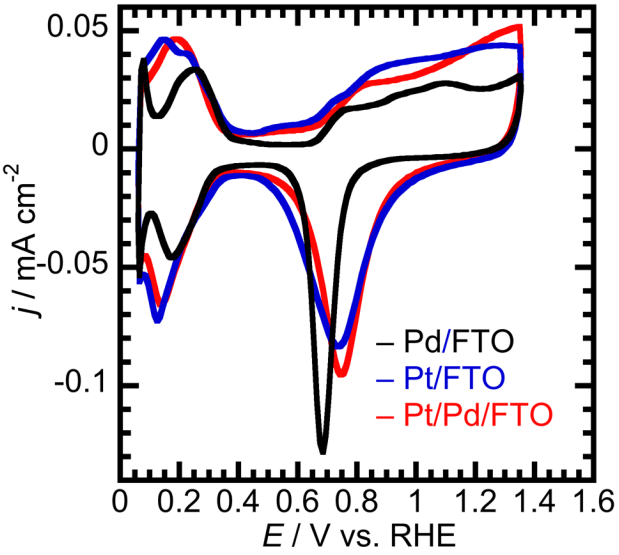


Figure 2.8 CVs of Pd/FTO, Pt/FTO, and Pt/Pd/FTO electrodes in an aqueous solution of 0.1 M $HClO_4$ at the sweep rate of 50 mV s^{-1} under Ar.

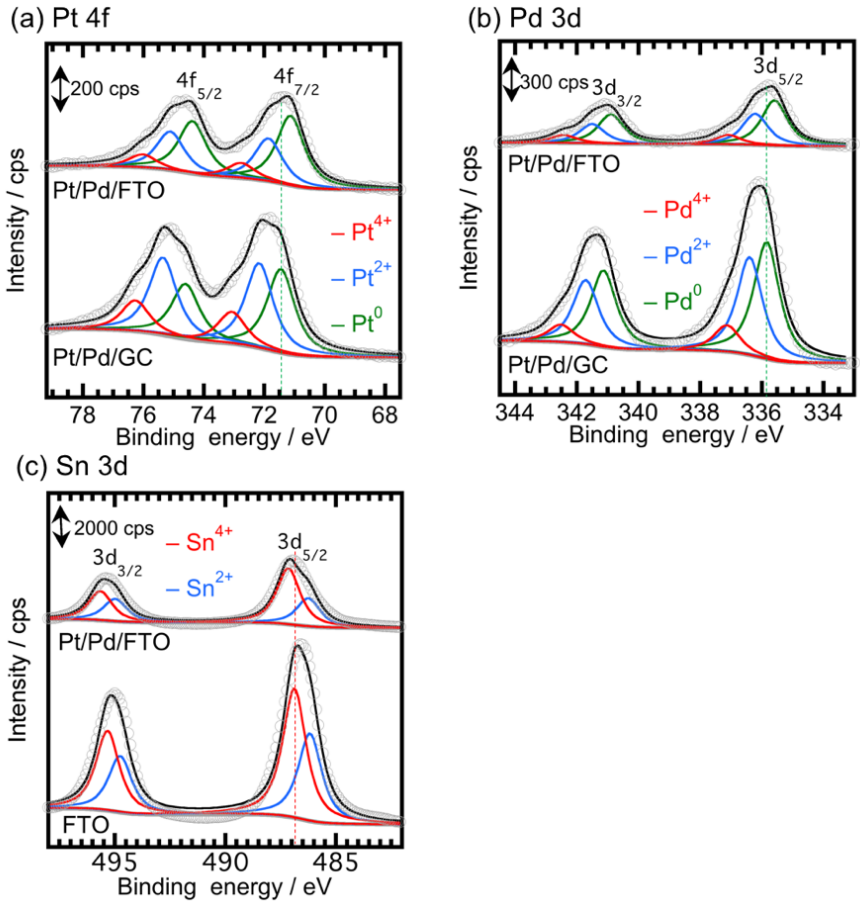


Figure 2.9 XPS of Pt/Pd/FTO and Pt/Pd/GC electrodes in the (a) Pt 4f, and (b) Pd 3d regions, and (c) Pt/Pd/FTO and FTO electrodes in the Sn 3d region. Experimental data (open circles), the sum of the deconvoluted data (solid line in black), and baseline (in gray).

Table 2.3 The results of peak deconvolution analysis of the XPS data in the Pt 4f and Pd 3d regions in Figure 2.9.

Electrode	Peak position in Pt $4f_{5/2}$ and Pd $3d_{3/2}$ / eV			Peak position in Pt $4f_{7/2}$ and Pd $3d_{5/2}$ / eV		
	Pt^{4+}	Pt^{2+}	Pt^{0}	Pt^{4+}	Pt^{2+}	Pt^{0}
Pt/Pd/FTO	76.0	75.1	74.4	72.8	71.9	71.1
Pt/Pd/GC	76.3	75.4	74.6	73.1	72.2	71.4
	Pd^{4+}	Pd^{2+}	Pd^{0}	Pd^{4+}	Pd^{2+}	Pd^{0}
Pt/Pd/FTO	342.4	341.5	340.9	337.1	336.2	335.6
Pt/Pd/GC	342.5	341.7	341.1	337.1	336.4	335.8

Table 2.4 The results of peak deconvolution analysis of the XPS data in the Sn 3d region in Figure 2.9.

Electrode	Peak position in Sn $3d_{3/2}$ / eV		Peak position in Sn $3d_{5/2}$ / eV	
	Sn^{4+}	Sn^{2+}	Sn^{4+}	Sn^{2+}
Pt/Pd/FTO	495.6	495.0	487.1	486.3
FTO	495.3	494.7	486.9	486.2

2.3.4 NO_2RR, NORR, and N_2ORR at Pt/Pd/FTO and Pt/Pd/GC electrodes

The high NO_3RR activity of the ternary metallic Pt/Pd/FTO encourages us to study NO_2RR, NORR, and N_2ORR using Pt/Pd/FTO and Pt/Pd/GC electrodes to further understand the role of the PtPd/Sn interface. Pt/Pd/FTO showed much higher cathodic currents than Pt/Pd/GC in a 0.1 M $HClO_4$ aqueous solution under N_2O (Figure 2.10a). Although Pt/FTO and Pd/FTO also showed the electrocatalytic N_2ORR activity (Figure 2.11), the activity of Pt/Pd/FTO was higher than those of Pt/FTO and Pd/FTO (Table 2.5). Therefore, the formation of the PtPd/Sn interface increases not only the NO_3RR activity but also the N_2ORR activity. The cathodic currents of Pt/Pd/FTO for the N_2ORR can be mainly found in the hydrogen adsorption region between +0.06 and +0.34 V vs. RHE (Figure 2.8). The N_2O adsorption can compete with the hydrogen adsorption on Pt and Pd

electrodes [31–33]. The PtPd/Sn interface could enhance the N_2O adsorption and/or suppress the hydrogen adsorption, leading to the enhancement of the N_2ORR activity.

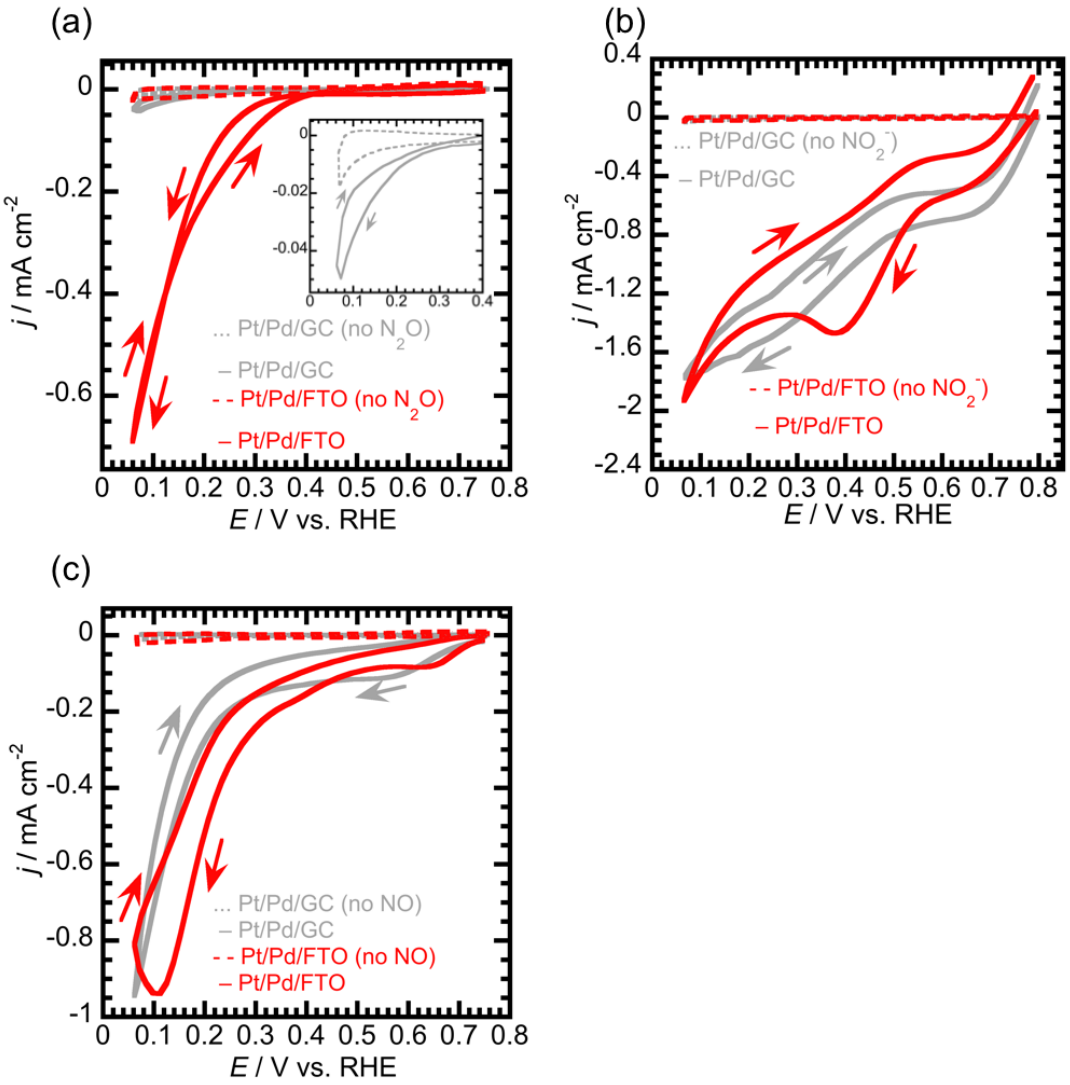


Figure 2.10 CVs of Pt/Pd/GC and Pt/Pd/FTO electrodes at a sweep rate of 10 mV s^{-1} in an aqueous solution of 0.1 M $HClO_4$ (a) under N_2O (The inset shows the magnified CVs of Pt/Pd/GC electrode), (b) containing 0.01 M $NaNO_2$ under Ar, and (c) under NO.

Pt/Pd/FTO and Pt/Pd/GC electrodes show similar cathodic currents for the NO_2RR and NORR, as shown in Figures 2.10b and c, respectively, indicating almost no difference in the NO_2RR and NORR activity between Pt/Pd/FTO and Pt/Pd/GC. This finding indicates that Sn shows no drastic contribution to the activity improvement for the NO_2RR and NORR. Because the NO_2RR and NORR mainly occur at more positive potentials than the hydrogen adsorption, NO_2^- or NO adsorption does not compete with the hydrogen

adsorption, resulting in no contribution of the ternary interface including Sn to the activity enhancement.

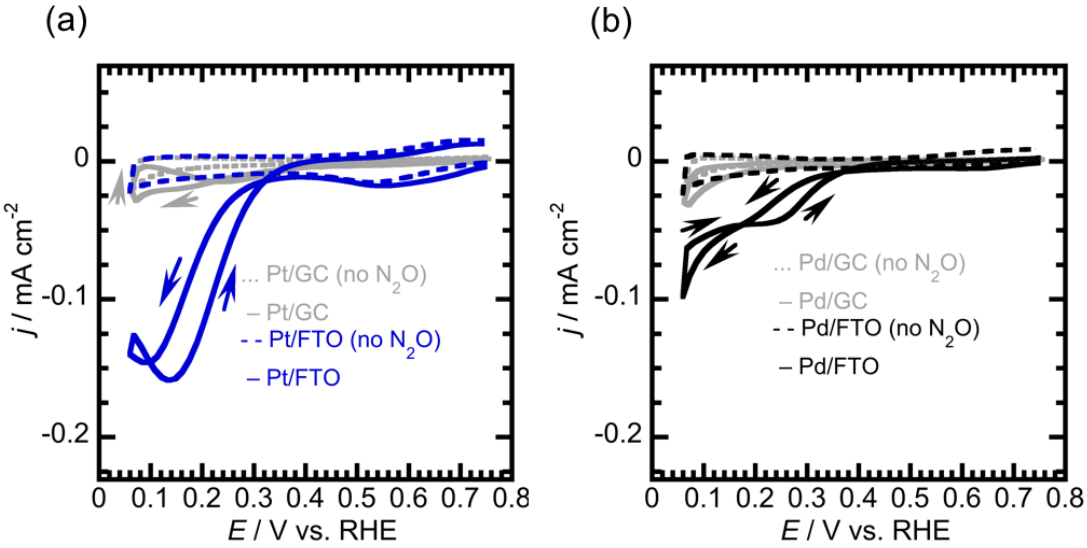
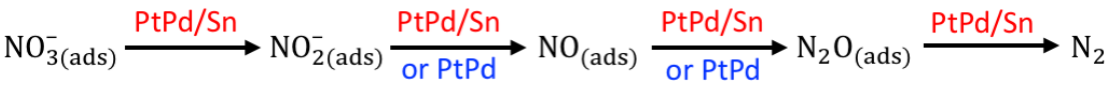


Figure 2.11 CVs of (a) Pt/GC and Pt/FTO electrodes, and (b) Pd/GC and Pd/FTO electrodes at a sweep rate of 10 mV s^{-1} in an aqueous solution of 0.1 M $HClO_4$ under N_2O.

Table 2.5 N_2ORR current densities (j) at +0.16 V vs. RHE shown by the Pd/FTO, Pt/FTO, and Pt/Pd/FTO electrodes in Figures 2.10a and 2.11.

Electrode	j/mA cm^{-2}
Pt/Pd/FTO	–0.25±0.04
Pt/FTO	–0.10±0.04
Pd/FTO	–0.05±0.01



Scheme 2.1 Highly active catalytic sites for the electrocatalytic NO_3RR, NO_2RR, NORR, and N_2ORR.

For the Pt/Pd/FTO electrode, the PtPd/Sn interface efficiently catalyzed the NO_3RR and N_2ORR but not the NO_2RR and NORR (Scheme 2.1). The NO_3RR and N_2ORR occur in the potential range of the hydrogen adsorption between +0.06 and +0.34 V vs. RHE (Figure 2.8). Since the adsorption of NO_3^- or N_2O competes with hydrogen adsorption on Pt and Pd electrodes in this potential region, the PtPd/Sn interface enhanced

the adsorption of NO_3^- or N_2O and/or suppressed the adsorption of hydrogen. As a consequence, the activity of NO_3RR and N_2ORR increased and less hydrogen at the PtPd/Sn interface may favor the formation of the most likely product N_2 instead of the formation of NH_4^+ and NH_3OH^+ [3,16,34,35]. In contrast, because of no overlap of onset potentials of the NO_2RR and NORR with hydrogen adsorption, Sn did not work as a promoter for the NO_2RR and NORR.

2.4 Conclusions

Our study demonstrates that the PtPd/Sn interface is effective to the electrocatalytic NO_3RR and N_2ORR, whereas it showed no drastic contribution to the electrocatalytic NO_2RR and NORR. It is most likely that the ternary metallic PtPd/Sn interface enhances the adsorption of NO_3^- and N_2O and/or suppressed the adsorption of hydrogen. XPS data of the Pt/Pd/FTO electrode revealed the charge transfer from Sn in FTO to Pt and Pd, suggesting the modulation of the adsorption ability of NO_3^-, N_2O, and hydrogen at the PtPd/Sn interface. Our findings will be helpful to develop highly efficient noble metal mixture/alloy NPs on FTO support electrodes for the practical application of denitrification.

2.5 References

[1] V. Rosca, M. Duca, M.T. DeGroot, M.T.M. Koper, Nitrogen Cycle Electrocatalysis, Chem. Rev. 109 (2009) 2209–2244. https://doi.org/10.1021/cr8003696.

[2] M. Duca, M.T.M. Koper, Powering denitrification: The perspectives of electrocatalytic nitrate reduction, Energy Environ. Sci. 5 (2012) 9726–9742. https://doi.org/10.1039/c2ee23062c.

[3] G.E. Dima, A.C.A. De Vooys, M.T.M. Koper, Electrocatalytic reduction of nitrate at low concentration on coinage and transition-metal electrodes in acid solutions, J. Electroanal. Chem. 554–555 (2003) 15–23. https://doi.org/10.1016/S0022-0728(02)01443-2.

[4] S. Taguchi, J.M. Feliu, Electrochemical reduction of nitrate on Pt(S)[n(1 1 1) × (1 1 1)] electrodes in perchloric acid solution, Electrochim. Acta. 52 (2007) 6023–6033. https://doi.org/10.1016/j.electacta.2007.03.057.

[5] M.C. Figueiredo, J. Solla-Gullón, F.J. Vidal-Iglesias, V. Climent, J.M. Feliu, Nitrate reduction at Pt(1 0 0) single crystals and preferentially oriented

nanoparticles in neutral media, Catal. Today. 202 (2013) 2–11. https://doi.org/10.1016/j.cattod.2012.02.038.

[6] J. Yang, F. Calle-Vallejo, M. Duca, M.T.M. Koper, Electrocatalytic reduction of nitrate on a Pt electrode modified by p-block metal adatoms in acid solution, ChemCatChem. 5 (2013) 1773–1783. https://doi.org/10.1002/cctc.201300075.

[7] K. Shimazu, R. Goto, S. Piao, R. Kayama, K. Nakata, Y. Yoshinaga, Reduction of nitrate ions on tin-modified palladium thin film electrodes, J. Electroanal. Chem. 601 (2007) 161–168. https://doi.org/10.1016/j.jelechem.2006.11.005.

[8] Y.Y. Birdja, J. Yang, M.T.M. Koper, Electrocatalytic reduction of nitrate on tin-modified palladium electrodes, Electrochim. Acta. 140 (2014) 518–524. https://doi.org/10.1016/j.electacta.2014.06.011.

[9] K. Shimazu, R. Goto, K. Tada, Electrochemical reduction of nitrate ions on tin-modified platinum and palladium electrodes, Chem. Lett. 31 (2002) 204–205. https://doi.org/10.1246/cl.2002.204.

[10] J. Yang, M. Duca, K.J.P. Schouten, M.T.M. Koper, Formation of volatile products during nitrate reduction on a Sn-modified Pt electrode in acid solution, J. Electroanal. Chem. 662 (2011) 87–92. https://doi.org/10.1016/j.jelechem.2011.03.015.

[11] J. Yang, Y. Kwon, M. Duca, M.T.M. Koper, Combining voltammetry and ion chromatography: Application to the selective reduction of nitrate on Pt and PtSn electrodes, Anal. Chem. 85 (2013) 7645–7649. https://doi.org/10.1021/ac401571w.

[12] M. Motahar Hossain, K. Nakata, T. Kawaguchi, K. Shimazu, Reduction of nitrate on electrochemically pre-reduced tin-modified palladium electrodes, J. Electroanal. Chem. 707 (2013) 59–65. https://doi.org/10.1016/j.jelechem.2013.08.015.

[13] O. Ghodbane, M. Sarrazin, L. Roué, D. Bélanger, Electrochemical Reduction of Nitrate on Pyrolytic Graphite-Supported Cu and Pd–Cu Electrocatalysts, J. Electrochem. Soc. 155 (2008) F117. https://doi.org/10.1149/1.2900094.

[14] S. Piao, Y. Kayama, Y. Nakano, K. Nakata, Y. Yoshinaga, K. Shimazu, Nitrate reduction on tin-modified rhodium, ruthenium, and iridium electrodes, J. Electroanal. Chem. 629 (2009) 110–116. https://doi.org/10.1016/j.jelechem.2009.01.031.

[15] M. Kato, A. Araki, Y. Hara, S. Taguchi, I. Yagi, Cathodic arc-plasma deposition of platinum nanoparticles on fluorine-doped tin oxide for electrocatalytic nitrate reduction reaction, Electrochemistry. 86 (2018) 220–222. https://doi.org/10.5796/electrochemistry.18-00031.

[16] M.M. Hossain, T. Kawaguchi, K. Shimazu, K. Nakata, Reduction of nitrate on tin-modified palladium-platinum electrodes, J. Electroanal. Chem. 864 (2020) 114041. https://doi.org/10.1016/j.jelechem.2020.114041.

[17] M. Kato, Y. Unuma, M. Okui, Y. Qu, J. Zheng, S. Taguchi, F. Kiguchi, M. Torihata, Y. Gao, N. Hoshi, I. Yagi, Electrocatalytic activity and volatile product selectivity for nitrate reduction at tin-modified Pt(100), Pd(100) and Pd–Pt(100) single crystal electrodes in acidic media, Electrochim. Acta. 398 (2021) 139281. https://doi.org/10.1016/j.electacta.2021.139281.

[18] J.F.E. Gootzen, P.G.J.M. Peeters, J.M.B. Dukers, L. Lefferts, W. Visscher, J.A.R. Van Veen, The electrocatalytic reduction of NO-3 on Pt, Pd and Pt + Pd electrodes activated with Ge, J. Electroanal. Chem. 434 (1997) 171–183. https://doi.org/10.1016/S0022-0728(97)00093-4.

[19] M. Kato, M. Okui, S. Taguchi, I. Yagi, Electrocatalytic nitrate reduction on well-defined surfaces of tin-modified platinum, palladium and platinum-palladium single crystalline electrodes in acidic and neutral media, J. Electroanal. Chem. 800 (2017) 46–53. https://doi.org/10.1016/j.jelechem.2017.01.020.

[20] G.E. Dima, V. Rosca, M.T.M. Koper, Role of germanium in promoting the electrocatalytic reduction of nitrate on platinum: An FTIR and DEMS study, J. Electroanal. Chem. 599 (2007) 167–176. https://doi.org/10.1016/j.jelechem.2005.12.005.

[21] J. Lim, C.Y. Liu, J. Park, Y.H. Liu, T.P. Senftle, S.W. Lee, M.C. Hatzell, Structure Sensitivity of Pd Facets for Enhanced Electrochemical Nitrate Reduction to Ammonia, ACS Catal. 11 (2021) 7568–7577. https://doi.org/10.1021/acscatal.1c01413.

[22] K. Nakata, Y. Doi, S. Kubota, K. Shimazu, Reduction of nitrite on tin-modified noble metal electrodes, J. Electroanal. Chem. 647 (2010) 187–193. https://doi.org/10.1016/j.jelechem.2010.06.003.

[23] S. Hinokuma, S. Misumi, H. Yoshida, M. Machida, Nanoparticle catalyst preparation using pulsed arc plasma deposition, Catal. Sci. Technol. 5 (2015)

4249–4257. https://doi.org/10.1039/c5cy00636h.

[24] M. Lukaszewski, M. Soszko, A. Czerwiński, Electrochemical methods of real surface area determination of noble metal electrodes - an overview, Int. J. Electrochem. Sci. 11 (2016) 4442–4469. https://doi.org/10.20964/2016.06.71.

[25] M. Grdeń, M. Łukaszewski, G. Jerkiewicz, A. Czerwiński, Electrochemical behaviour of palladium electrode: Oxidation, electrodissolution and ionic adsorption, Electrochim. Acta. 53 (2008) 7583–7598. https://doi.org/10.1016/j.electacta.2008.05.046.

[26] L.H. Dall'Antonia, G. Tremiliosi-Filho, G. Jerkiewicz, Influence of temperature on the growth of surface oxides on palladium electrodes, J. Electroanal. Chem. 502 (2001) 72–81. https://doi.org/10.1016/S0022-0728(00)00505-2.

[27] C. Gabrielli, P.P. Grand, A. Lasia, H. Perrot, Investigation of Hydrogen Adsorption and Absorption in Palladium Thin Films, J. Electrochem. Soc. 151 (2004) A1937. https://doi.org/10.1149/1.1797035.

[28] I. Achari, S. Ambrozik, N. Dimitrov, Electrochemical Atomic Layer Deposition of Pd Ultrathin Films by Surface Limited Redox Replacement of Underpotentially Deposited H in a Single Cell, J. Phys. Chem. C. 121 (2017) 4404–4411. https://doi.org/10.1021/acs.jpcc.6b12794.

[29] K. Tada, K. Shimazu, Kinetic studies of reduction of nitrate ions at Sn-modified Pt electrodes using a quartz crystal microbalance, J. Electroanal. Chem. 577 (2005) 303–309. https://doi.org/10.1016/j.jelechem.2004.11.039.

[30] J.X. Liu, D. Richards, N. Singh, B.R. Goldsmith, Activity and Selectivity Trends in Electrocatalytic Nitrate Reduction on Transition Metals, ACS Catal. 9 (2019) 7052–7064. https://doi.org/10.1021/acscatal.9b02179.

[31] H. Ebert, R. Parsons, G. Ritzoulis, T. VanderNoot, The reduction of nitrous oxide on platinum electrodes in acid solution, J. Electroanal. Chem. 264 (1989) 181–193. https://doi.org/10.1016/0022-0728(89)80156-1.

[32] A. Ahmadi, E. Bracey, R. Wyn Evans, G. Attard, Anion-surface interactions. Part II. Nitrous oxide reduction as a probe of anion adsorption on transition metal surfaces, J. Electroanal. Chem. 350 (1993) 297–316. https://doi.org/10.1016/0022-0728(93)80212-Z.

[33] A. Aziznia, A. Bonakdarpour, E.L. Gyenge, C.W. Oloman, Electroreduction of nitrous oxide on platinum and palladium: Toward selective catalysts for methanol-

nitrous oxide mixed-reactant fuel cells, Electrochim. Acta. 56 (2011) 5238–5244. https://doi.org/10.1016/j.electacta.2011.03.023.

[34] J. Souza-Garcia, E.A. Ticianelli, V. Climent, J.M. Feliu, Mechanistic changes observed in heavy water for nitrate reduction reaction on palladium-modified Pt(hkl) electrodes, Chem. Sci. 3 (2012) 3063–3070. https://doi.org/10.1039/c2sc20490h.

[35] J. Souza-Garcia, E.A. Ticianelli, V. Climent, J.M. Feliu, Nitrate reduction on Pt single crystals with Pd multilayer, Electrochim. Acta. 54 (2009) 2094–2101. https://doi.org/10.1016/j.electacta.2008.08.059.

Chapter 3

Electrocatalytic Nitrous Oxide Reduction at Pt–Pd–Sn Nanoparticles

3.1 Introduction

Nitrous oxide (N_2O) is an ozone-depleting and global warming gas and can be reduced using a green technology electrocatalytic N_2O reduction [1,2]. Electrocatalytic N_2O reduction has been widely studied on noble metal electrodes including Pt and Pd [3–8]. Generally, Pt and Pd show low N_2ORR activity in acidic media because of the competitive adsorption of N_2O with hydrogen, although they can produce N_2 with about 100% Faradaic efficiency [3,5,7,8]. In Chapter 2, the improvement of N_2ORR activity was demonstrated by Pt and/or Pd nanoparticles (NPs) prepared by an arc-plasma deposition (APD) method on fluorine-doped tin oxide (FTO) substrates (Pt/FTO, Pd/FTO, and Pt/Pd/FTO), in which the Pt/FTO electrode showed higher N_2ORR activity than the Pd/FTO electrode. Even the trimetallic Pt/Pd/FTO electrode with Pt:Pd = 3:2 atomic ratio showed greater N_2ORR activity than the bimetallic Pt/FTO electrode. Since the deposition of Pt and Pd NPs on FTO substrates by the APD is a model study to get the optimized Pt to Pd atomic ratio for N_2ORR, there is a lack of detailed investigation on the Faradaic efficiency (FE) of N_2 and the catalytic performance in terms of turnover frequency (TOF) of N_2, therefore, the Pt–Pd–Sn NPs were synthesized with the optimized Pt:Pd = 3:2 atomic ratio by a wet chemical method, which is more practical.

Herein, we report the preparation of Pt–Sn NPs, and Pt–Pd–Sn NPs based on the optimized Pt:Pd = 3:2 atomic ratio obtained from the APD method to investigate the role of the PtPd/Sn interface for electrocatalytic N_2ORR activity in acidic media. Chronoamperometric experiments were performed at different potentials for the detection and quantification of the gaseous product N_2 by gas chromatography. In the potential region of hydrogen evolution, H_2 was detected and the Faradaic efficiency of H_2 allowed us to confirm the suppression of hydrogen adsorption at the trimetallic PtPd/Sn interface when compared that at the bimetallic Pt/Sn interface. To evaluate the catalytic efficiency, the TOF of N_2 was calculated. To understand the electronic effects, X-ray photoelectron spectroscopy (XPS) of the catalysts was performed.

3.2 Experimental section

3.2.1 Materials

Ethanol, hexane, 2-propanol, perchloric acid, oleylamine, butylamine, [$Pt(acac)_2$] (acac = acetylacetonate) and 5% Nafion DE520 were purchased from Wako Pure Chemical Industries, Ltd. Borane-mopholine complex, tin(II) chloride dihydrate and [$Pd(acac)_2$] were commercially available from TCI, Kanto Chemical Co., Inc. and Sigma-Aldrich, respectively. Vulcan XC-72 carbon black was bought from Cabot Corporation. Pure argon gas (99.9995%, Hokkaido Air Water) and nitrous oxide (99.5%, GL Science) were used for electrochemical measurements.

3.2.2 Synthesis of Pt–Sn and Pt–Pd–Sn nanoparticles

Pt–Sn NPs were synthesized with Pt:Sn = 75:25 (at%) in a modified method based on a reported synthetic procedure [9]. In a three-necked round bottom flask (100 mL), 47.2 mg of [$Pt(acac)_2$] (0.12 mmol) and 15 mL of oleylamine (OAm) were added and mixed them by ultrasonication for 10 min, but the mixture was not transparent. The mixture was then placed in an oil bath and the temperature of the mixture was increased to 60 °C under Ar and magnetic stirring to get a transparent mixture with pale yellow color. In a glass vial, 100 mg of borane-morpholine complex (BM) (0.99 mmol), a reductant, was dissolved in 3 mL of OAm by ultrasonication and the solution was quickly injected into the 60 °C precursor solution to initiate the nucleation. Then, the temperature was raised to 90 °C and the color of the mixture changed completely to black. The mixture was kept at this temperature for 30 min for the formation of Pt seed NPs. After that, the temperature of the mixture was raised to 180 °C for the growth of the NPs. In a glass vial, 9.0 mg of $SnCl_2.2H_2O$ (0.04 mmol) was dissolved in 3 mL of OAm by ultrasonication, and the solution was quickly injected into the 180 °C mixture. The mixture was kept at 180 °C for 30 min for the formation of Pt–Sn NPs. After the mixture had cooled to room temperature, the Pt–Sn NPs were separated by adding ethanol and centrifugation at 12,000 rpm at 25 °C for 10 min using a Micro Refrigerated Centrifuge 3700 equipped with an angle rotor AF-5004CA (Kubota Co.). The Pt–Sn NPs were further washed with ca. 15 mL of ethanol–hexane solvent mixture (8:2, *v*/*v*) eight times under centrifugation at 10,000 rpm at 25 °C for 5 min and finally stored in ethanol at room temperature until use. Similarly, the Pt NPs were synthesized without the addition of $SnCl_2.2H_2O$.

Pt–Pd–Sn NPs with Pt:Pd:Sn = 45:30:25 (at%) were synthesized in a similar synthetic procedure of Pt–Sn NPs by replacing some at% of Pt by Pd with keeping the optimized Pt:Pd = 3:2 = 45:30 atomic ratio obtained from APD system in Chapter 2. In this case, 28.3 mg of [$Pt(acac)_2$] (0.072 mmol) and 14.6 mg of [$Pd(acac)_2$] (0.048 mmol) were mixed together in OAm by ultrasonication in a three-necked round bottom flask (100 mL). The Pt–Pd NPs were synthesized in a similar synthetic procedure of Pt–Pd–Sn NPs without using $SnCl_2.2H_2O$.

3.2.3 Preparation of carbon-supported Pt–Sn and Pt–Pd–Sn NPs

Vulcan XC-72 carbon black (ca. 1.2 mg, 80%) and Pt–Sn or Pt–Pd–Sn NPs (ca. 0.3 mg, 20%) were dispersed in 10 mL of butyleamine (BAm) in order to the removal of OAm and the impregnation of the NPs on the carbon support. The mixture was ultrasonicated for one hour and then stirred at 200 rpm for three days. After that, the mixture was collected by centrifugation at 12,000 rpm for 10 min. The precipitate was washed with ethanol (ca. 10 mL) two times at 10,000 rpm for 7 min and then re-dispersed in 900 μL of 2-propanol and 1600 μL of Milli-Q water. The mixture was transferred into a 5 mL of a glass vial and 10 μL of 5% Nafion DE520 was added. Then, the mixture was ultrasonicated for three hours to obtain the catalyst ink of carbon-supported Pt–Sn or Pt–Pd–Sn NPs (Pt–Sn/C or Pt–Pd–Sn/C) for the preparation of working electrodes.

3.2.4 Catalyst characterizations

Transmission electron microscopy (TEM) images were taken by a JEM-2000FX (JEOL) at an acceleration voltage of 200 kV. Scanning transmission electron microscopy (STEM) and energy dispersive spectroscopy (EDS) elemental mapping images were taken by a JEM-ARM200F (JEOL) at an acceleration voltage of 200 kV. X-ray powder diffraction (XRD) was performed on a BRUKER D2 PHAGER 2nd Gen diffractometer with Cu Kα radiation (λ = 0.154184 nm). The crystallite size (D) from the 111 diffraction peak was calculated by Scherrer`s equation [10]:

$$D = k\lambda/\beta\cos\theta \qquad (3.1)$$

where k is a particle shape-dependent constant (assuming spherical particles, $k = 0.9$), λ is the wavelength of the X-ray radiation (for Cu Kα, λ = 0.154184 nm), θ is the angle in radians of the diffraction peak and β is the width in radians of the diffraction peak at half-height. Inductively coupled plasma mass spectrometry (ICP-MS) measurements were

performed using an ICP-MS spectrometer 8800 ICP-QQQ (Agilent Technologies). For sample preparation of ICP-MS, a catalyst ink was dispersed in aqua regia solution, and then the dispersion was stirred at 35 °C for at least 24 h. The dispersion was filtered through a membrane filter (13HP045AN, ADVANTEC), and then the filtrate was diluted with Milli-Q water. X-ray photoelectron spectroscopy (XPS) data were collected at the pass energy of 10 eV using an Al Kα X-ray source by a photoelectron spectrometer JPS-9200 (JEOL). The binding energy was calibrated using C 1s peak at 284.7 eV. To prepare the sample for XPS, catalyst ink of carbon (ca. 1.2 mg)-supported NPs (ca. 0.6 mg) in 2-propanol without Nafion was drop-cast on a carbon tape (ca. 1 cm in length) and the solvent was evaporated at 100 °C.

3.2.5 Electrochemical measurements

Electrochemical measurements were performed using a conventional three-electrode, one compartment electrochemical cell by a potentiostat HZ-7000 (Hokuto Denko Corp.). A platinized Pt foil and an Ag|AgCl (sat. KCl) were used as the counter and the reference electrodes, respectively. A glassy carbon (GC) plate, on which the catalyst was cast, was used as the working electrode.

A GC plate ($25 \times 25 \times 2$ mm^3, AS ALS Co., Ltd.) was polished with alumina slurry (0.3 μm, Baikalox), followed by alumina slurry (0.05 μm, Baikalox), and then sonicated in water, ethanol, and Milli-Q water for 5 min each. A polyethylene tape with a prepared hole of 8 mm in diameter was placed on the GC plate to control the surface area of the working electrode. Thus, the geometrical surface area of the working electrode was controlled to be 0.50 cm^2. For all catalysts, the ink (43~50 μL) was drop-cast on the hole so that the metal loading was 11.2 μg cm^{-2}, and then dried at 40 °C for 20 min.

Cyclic voltammograms (CVs) were recorded in an aqueous solution of 0.1 M $HClO_4$. Before measurements of CVs, the electrolyte solution was purged with Ar for at least 30 min. For electrochemical cleaning, three potential cycles at 200 mV s^{-1} were performed in the potential range between –0.2 and +1.1 V vs. Ag|AgCl (sat. KCl) in a 0.1 M $HClO_4$ aqueous solution under Ar before recording CVs at 50 mV s^{-1} in the text. For electrochemical N_2O reduction, a 0.1 M $HClO_4$ aqueous solution in the electrochemical cell was saturated with bubbling of N_2O gas at 10 mL min^{-1} for 30 min, and then the CVs were recorded under N_2O at a sweep rate of 10 mV s^{-1}. The first cycle of the CVs was

always used for making a graph in presence of N_2O. All potentials shown were converted to be versus the reversible hydrogen electrode (RHE) by using the following equation:
E (vs. RHE) = E (vs. Ag|AgCl (sat. KCl)) + 0.199 + 0.059 × pH.

Electrolysis experiments for N_2ORR in acidic media were conducted with an H-type electrolytic cell separated by a Nafion NRE-211 (DuPoint) membrane. The Nafion membrane was boiled in 3% H_2O_2 at 80 ºC for 1 h, in Milli-Q water at 100 ºC for 1 h, in 1 M H_2SO_4 at 80 ºC for 1 h, and then in Milli-Q water at 100 ºC for 1 h, sequentially. The working electrodes, Pt–Sn/C and Pt–Pd–Sn/C, were prepared on both sides of the GC substrates (2.69 cm^2+2.69 cm^2) with metal loading 11.2 μg cm^{-2}. A working electrode and an Ag|AgCl (sat. KCl) as the reference electrode were placed in the cathodic chamber, and a platinized Pt foil as the counter electrode was placed in the anodic chamber. 25 mL of a 0.1 M $HClO_4$ aqueous solution was added in each chamber and only the solution in the cathodic chamber was saturated with bubbling of N_2O for 30 min at 10 mL min^{-1} after pursing the solution with Ar for 30 min. Chronoamperometry (CA) was performed at 0.0 V, +0.06 V, and +0.12 V vs. RHE for 1 h for the detection of gaseous products.

3.2.6 Gaseous product detection and quantification

The gaseous products were analyzed by gas chromatography (GC-8A, SHIMADZU) equipped with a thermal conductivity detector (TCD) at a constant column temperature of 50 °C and a detector temperature of 150 °C. The chromatographic column was a Shincarbon-ST 50/80 and an Ar stream was the carrier gas flowing at a constant pressure of 0.5 MPa. 100 μL of the gaseous product was collected by a Hamilton syringe (100 μL) from the headspace of the cathodic chamber after 1 h electrolysis and introduced in the GC–TCD, and N_2 and/or H_2 were detected. The retention times of H_2 and N_2 was ca. 3.4 and 9.3 min, respectively. Air-tightness of the electrochemical cell was confirmed by GC–TCD after a blank experiment under Ar. For the quantification of N_2, an external calibration was carried out by pure N_2 gas with aliquotes of 3 to 50 μL. For the calibration curve of H_2, 10 ~ 90 μL of a mixture of H_2 and Ar with 1:9 (v/v) ratio was injected into the GC–TCD. The number of moles (n) of N_2 or H_2 was calculated using the following Eq. (3.2):

$$n = \frac{pV}{RT} \qquad (3.2)$$

where the p is the pressure of the gas (p = 101325 Pa), R is the gas constant (R = 8.314 J mol^{-1} K^{-1}) and T is the absolute temperature of the gas (298.15 K), and V is the injected

volume (L) of N_2 or H_2 into the GC–TCD. The plots of peak area against the number of moles of N_2 or H_2 showed a linear relationship with $R^2 = 0.9999$ (Figure 3.1). Using the calibration curves, the number of moles of N_2 and H_2 each present in 100 μL of headspace was calculated and thus, the total number of moles of N_2 or H_2 present in the head space was estimated.

The number of moles of N_2 and/or H_2 present in the solution was calculated based on Henry`s law [11]. This law can be stated by the following Eq. (3.3):

$$c = H^{cp} \times p$$

$$\text{Or } n = H^{cp} \times p \times V \qquad (3.3)$$

where c is the solubility (mol L^{-1}) of a gas in the solution, p is the partial pressure (Pa) of the gas in the headspace under equilibrium conditions, H^{cp} is Henry`s law solubility constant (H^{cp} = 6.4 ×10^{-9} mol L^{-1} Pa^{-1} for N_2 and 7.7 ×10^{-9} mol L^{-1} Pa^{-1} for H_2), n is the number of moles of the gas in the solution, and V is the volume (L) of the solution in the cathodic chamber. The p of the gas was calculated using Eq. (3.2) when V is assigned as the volume of the head space.

The total number of moles of produced N_2 or H_2 ($mol_{N_2 \text{ or } H_2}$) in the cathodic chamber allowed us to calculate Faradaic efficiency (FE) for each of them using Eq. (3.4):

$$\text{FE} = \frac{mol_{N_2 \text{ or } H_2} \times F \times 2}{Q} \times 100 \qquad (3.4)$$

where $mol_{N_2 \text{ or } H_2}$ is the number of moles of the produced N_2 or H_2, F is the Faradaic constant (F = 96485 C mol^{-1}), Q is the total charges (C) obtained from 1 h of electrolysis, and 2 is the number of electrons required for the N_2O reduction to N_2 or the $2H^+$ reduction to H_2. Collection of the gaseous products from electrochemical cell and injection them into the GC–TCD by the Hamilton syringe using hand may cause small amount of missing FE.

The turnover frequency (TOF) of produced N_2 or H_2 in the cathodic chamber after 1 h electrolysis was calculated using Eq. (3.5) [12,13]:

$$\text{TOF} = \frac{\mathrm{d}(mol_{N_2 \text{ or } H_2})/\mathrm{d}t}{mol_{(\text{noble metals})}} \qquad (3.5)$$

where $(mol_{N_2 \text{ or } H_2})/\mathrm{d}t$ is the rate at which the number of moles of the N_2 or H_2 is generated after 1 h electrolysis, $mol_{(\text{noble metal})}$ is the number of moles of noble metals involved in the production of N_2 or H_2.

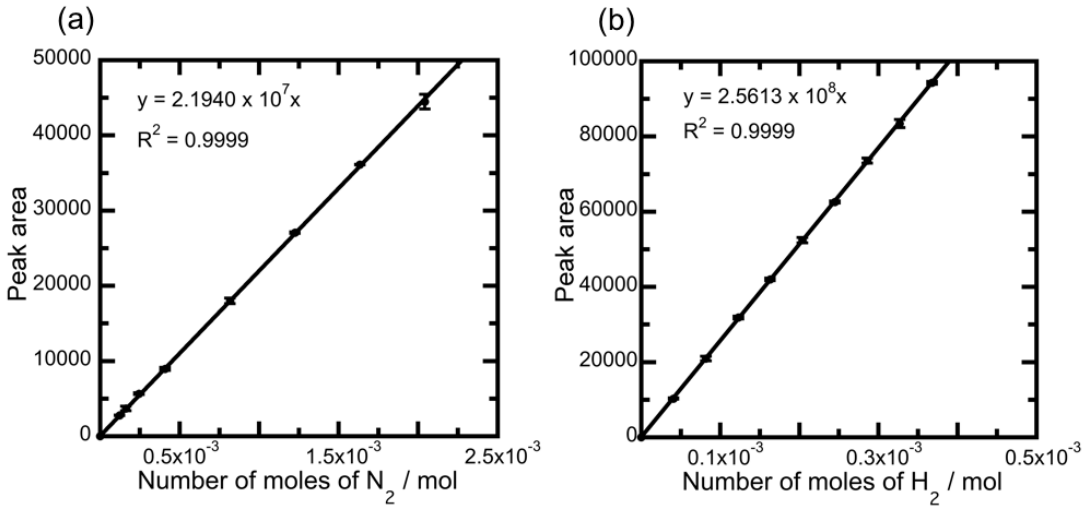


Figure 3.1 The peak area-mole calibration curves of (a) N_2 and (b) H_2 by gas chromatography.

3.3 Results and discussion

3.3.1 Characterization of Pt–Sn/C and Pt–Pd–Sn/C

TEM observation of Pt–Sn/C revealed the preparation of Pt–Sn NPs with an average size of 8.2 nm, which were loaded on carbon support (Figure 3.2a). STEM and EDS mapping images of Pt–Sn/C showed that the Sn is present around the Pt NPs, indicating the formation of Sn-patched Pt NPs (Figure 3.2b). And the Pt:Sn atomic ratio was found to be 81:19, which is almost similar to 81:19 obtained from inductively coupled plasma mass spectroscopy (ICP-MS) measurements. For Pt–Pd–Sn/C, TEM, STEM, and EDS mapping images in Figure 3.3 allowed us to confirm the Sn-patched Pt-Pd mixture NPs with a Pt:Pd:Sn atomic ratio of 52:29:19, which is almost similar to the Pt:Pd:Sn atomic ratio of 48:29:23 obtained from ICP-MS measurement. The average size of the Pt–Pd–Sn NPs was found to be 10.2 nm. X-ray diffraction (XRD) patterns of the Pt–Sn/C and Pt–Pd–Sn/C indicate the representative face-centered cubic (fcc) structure (Figure 3.4) [10,14]. Almost no diffraction peak shift occurred for Pt–Sn/C and Pt–Pd–Sn/C when compared with Pt/C and Pt–Pd/C, respectively, indicating the presence of Sn around Pt and Pt-Pd mixture NPs, respectively (Table 3.1). In the co-presence of smaller Pd atoms with Pt atoms in Pt–Pd/C, the 111 diffraction peak shifted to a little bit higher value of $2\theta \approx 39.78°$ than that ($2\theta \approx 39.64°$) of Pt/C, indicating the formation of Pt-Pd mixture NPs that were confirmed from STEM and EDS mapping images in Figure 3.3. Note that the 111 diffraction peak of Pd NPs was reported to be 40.48° [15]. When the Sn (bigger than

Pt) was incorporated on the surface of Pt-Pd mixture NPs, the 111 diffraction peak shifted to a little bit lower value of $2\theta \approx 39.64°$ than that ($2\theta \approx 39.78°$) of Pt–Pd/C. The $2\theta \approx 39.64°$ value of Pt–Pd–Sn/C is similar to that of Pt/C because of some surface alloy formation of Pt, Pd, and Sn. The crystallite diameters were determined by Scherrer`s equation for intense 111 diffraction peak (Table 3.2). They differed from 2.6 to 3.6 nm. In XPS spectra, the Pt–Sn/C showed peaks in the Pt 4f and Sn 3d regions, and the Pt–Pd–Sn/C showed peaks in the Pt 4f and Pd 3d and Sn 3d regions, indicating the preparation of Pt–Sn and Pt–Pd–Sn NPs (Figure 3.5).

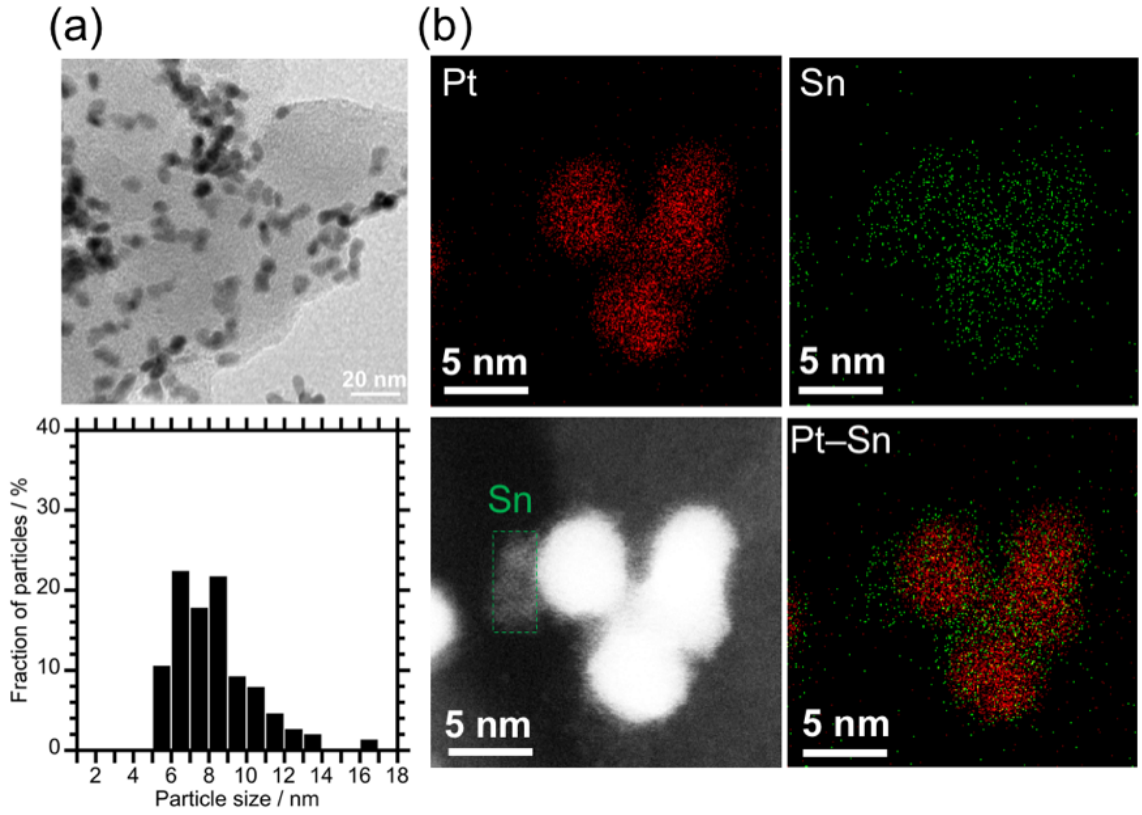


Figure 3.2 (a) TEM image and size distribution, and (c) STEM and EDS elemental mapping images of Pt–Sn/C. The red and green color images indicate the Pt and Sn elements, respectively.

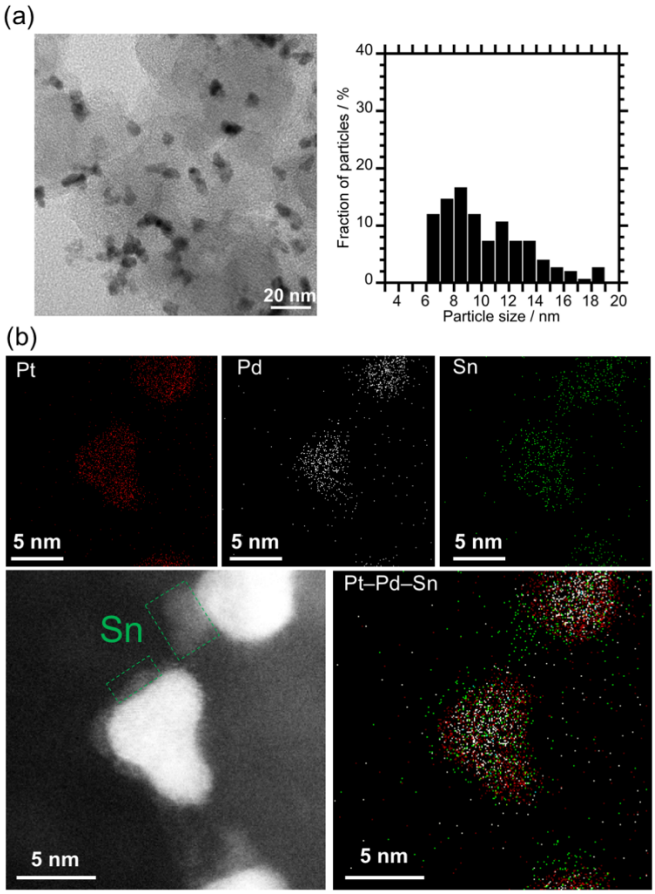


Figure 3.3 (a) TEM image and size distribution, and (b) STEM and EDS elemental maping images of Pt–Pd–Sn/C. The red, pale yellow, and green color images indicate the Pt, Pd, and Sn elements, respectively.

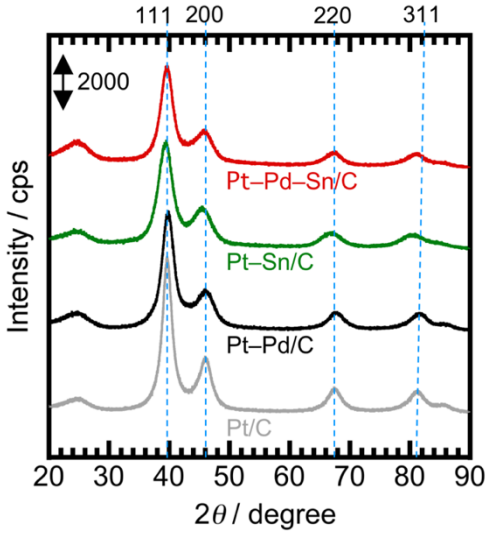


Figure 3.4 XRD patterns of Pt–Pd–Sn/C, Pt–Sn/C, Pt–Pd/C, and Pt/C.

Table 3.1 XRD results of the Pt–Pd–Sn/C, Pt–Sn/C, Pt–Pd/C, and Pt/C in Figure 3.4.

Catalysts	111	200	220	311
Pd–Pd–Sn/C	39.64	45.83	67.36	81.25
Pt–Sn/C	39.52	45.44	67.25	80.89
Pt–Pd/C	39.78	46.03	67.52	81.60
Pt/C	39.64	45.99	67.44	81.33

Table 3.2 Crystallite size of the Pt–Pd–Sn/C, Pt–Sn/C, Pt–Pd/C, and Pt/C calculated from the 111 diffraction peak in Figure 3.4.

Catalysts	Crystallite size, D / nm
Pd–Pd–Sn/C	3.0
Pt–Sn/C	2.6
Pt–Pd/C	3.1
Pt/C	3.6

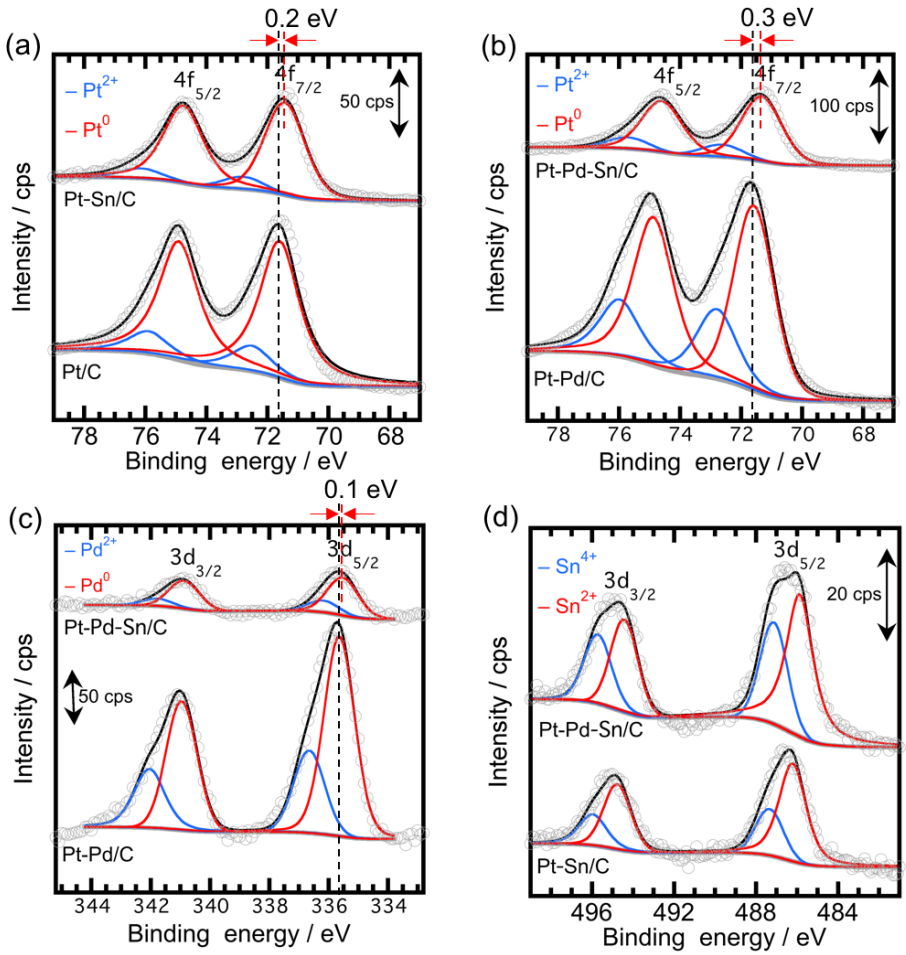


Figure 3.5 XPS of Pt–Sn/C and Pt/C in the (a) Pt 4f and (d) Sn 3d regions, and Pt–Pd–Sn/C and Pt–Pd/C in the (b) Pt 4f, (c) Pd 3d, and (d) Sn 3d regions. Experimental data (open circles), the sum of the deconvoluted data (solid line in black), and baseline (in gray).

3.3.2 Electrocatalytic N_2ORR at Pt–Sn/C and Pt–Pd–Sn/C

CVs of Pt–Sn/C and Pt–Pd–Sn/C were recorded at a sweep rate of 50 mV s^{-1} in a 0.1 M $HClO_4$ aqueous solution under Ar before investigating electrocatalytic N_2ORR under N_2O (Figure 3.6a). Hydrogen adsorption/desorption currents were observed in the potential range between +0.06 and +0.36 V vs. RHE. In the positive going sweep, Sn oxidation waves were observed between +0.6 and +0.9 V vs. RHE, where no such wave was observed at Pt/C and Pt–Pd/C (a controlled sample of Pt–Pd–Sn/C without Sn) and a wider reduction peak of metal oxides including SnO_x was observed between +0.54 and +0.70 V vs. RHE than Pt/C at +0.69 V vs. RHE and Pt–Pd/C at +0.66 V vs. RHE in the negative going sweep [16]. These results indicate that the Sn is present on the surface of Pt and Pt–Pd NPs.

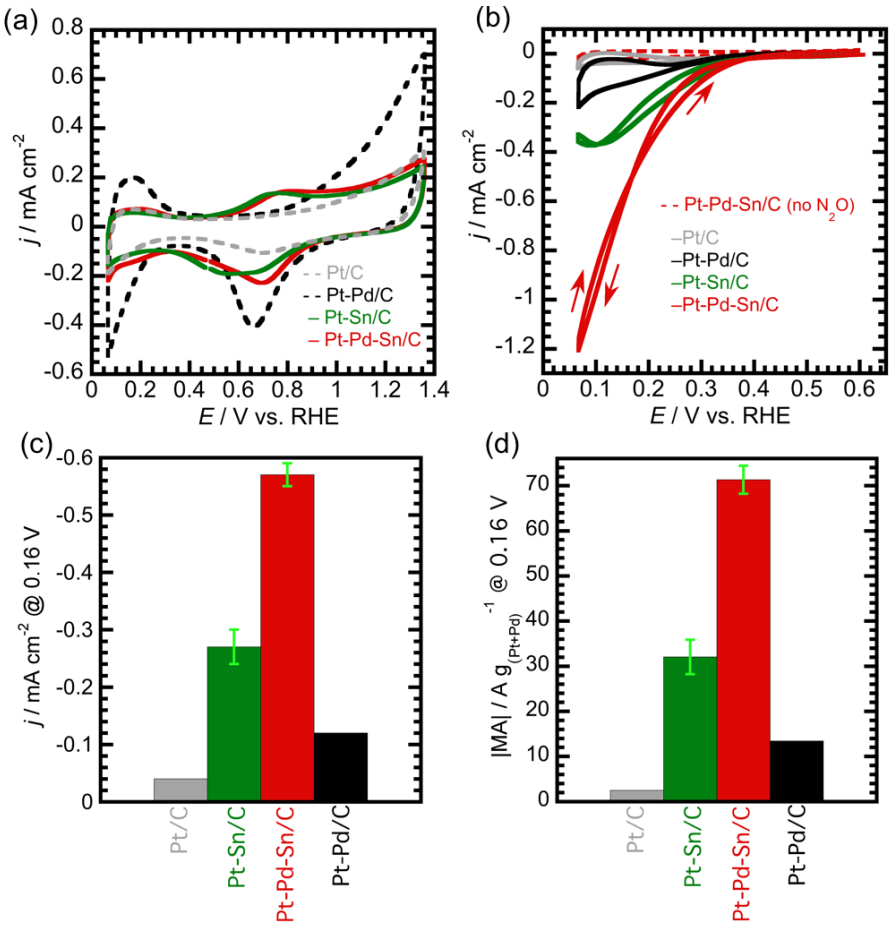


Figure 3.6 CVs of Pt–Pd–Sn/C, Pt–Sn/C, Pt–Pd/C, and Pt/C in a 0.1 M $HClO_4$ aqueous solution (a) at a sweep rate of 50 mV s^{-1} under Ar and (b) at a sweep rate of 10 mV s^{-1} under N_2O. The histograms of the N_2ORR (c) current density and (d) noble metal mass activity at +0.16 V vs. RHE.

The CVs of the Pt–Sn/C and Pt–Pd–Sn/C under N_2O showed cathodic currents in the potential range between +0.06 and +0.36 V vs. RHE (Figure 3.6b). These currents can be associated with the electrochemical N_2ORR [17]. The Pt–Sn/C showed high N_2ORR currents when compared with a Pt/C, indicating the role of Pt/Sn interfaces in the enhancement N_2ORR activity. A similar enhancement role of the Pt/Sn interfaces was discussed for N_2ORR at the Pt/FTO electrode in Chapter 2. The value of N_2ORR current density of Pt–Sn/C was found to be –0.27 mA cm^{-2} at +0.16 V vs. RHE, which is about three times higher than the Pt/FTO (Figure 3.6c). The Pt–Sn/C also showed higher mass activity of 32.04 A g_{Pt}^{-1} than Pt/C at +0.16 V vs. RHE (Figure 3.6d) and the charge transfer from Sn to Pt was confirmed by XPS, in which Pt 4f peaks of Pt–Sn/C shifted to the lower binding energy than those of Pt/C (Figure 3.5a).

The trimetallic Pt–Pd–Sn/C showed higher N_2ORR current density than the bimetallic Pt–Sn/C (Figure 3.6b). A similar result was reported in Chapter 2, in which the trimetallic Pt/Pd/FTO electrode showed higher N_2ORR current density than the bimetallic Pt/FTO electrode. The N_2ORR current density of Pt–Pd–Sn/C at +0.16 V vs. RHE was found to be –0.57 mA cm^{-2}, which is about two times higher than –0.25 mA cm^{-2} at Pt/Pd/FTO electrode (Figure 3.6c). The Pt–Pd–Sn/C also showed the highest mass activity of 72.38 A $g_{(Pt+Pd)}^{-1}$ at +0.16 V vs. RHE (Figure 3.6d). Furthermore, Pt–Pd/C showed very lower N_2ORR activity than Pt–Pd–Sn/C (Figure 3.5b). Thus, the effective role of PtPd/Sn interfaces of the Pt–Pd–Sn/C has been confirmed for high N_2ORR activity and the N_2ORR activity follows the following order: Pt–Pd–Sn/C > Pt–Sn/C > Pt–Pd/C > Pt/C.

The Pt–Pd–Sn/C showed N_2ORR currents in the potential region between +0.06 and +0.36 V vs. RHE (Figure 3.6b). In this potential region, the adsorption of N_2O competes with the adsorption of hydrogen (Figure 3.6a) [5,7,8]. The PtPd/Sn interface could enhance the adsorption of N_2O and/or suppress the adsorption of hydrogen, leading to the enhancement of the N_2ORR activity. A similar observation was found for N_2ORR at Pt/Pd/FTO electrode. XPS observation of Pt–Pd–Sn/C confirms the charge transfer from Sn to Pt and Pd: lower binding energy shifts than Pt–Pd/C in the in the Pt 4f and Pd 3d regions (Figures 3.5b and c). Thus, the ternary metallic PtPd/Sn interface finely tunes the N_2O adsorption ability, resulting in the high N_2ORR activity.

3.3.3 Product analysis of electrocatalytic N_2ORR

The product obtained from N_2ORR in acidic media was analyzed by gas chromatography (GC) equipped with a thermal conductivity detector (TCD). For this, chronoamperometric (CA) experiments of Pt–Sn/C and Pt–Pd–Sn/C were performed using an airtight H-type electrochemical cell containing 0.1 M $HClO_4$ (aq) under N_2O at three equidistant potentials: 0.0, +0.06, and +0.12 V vs. RHE for 1 h (Figures 3.7a and b). After electrolysis, N_2 and/or H_2 were detected by the GC–TCD. The Pt–Sn/C and Pt–Pd–Sn/C showed almost 100% FE for N_2 at +0.06 V vs. RHE or more positive potential, but below this potential, the FE of N_2 decreased due to H_2 evolution reaction (Figures 3.7c and d, and Table 3.3) [3]. At 0.0 V vs. RHE, the FEs of N_2 and H_2 at Pt–Sn/C were found to be ca. 64.38 and 30.23 %, respectively, whereas 75.49 and 10.67 %, respectively, at Pt–Pd–Sn/C. The lower value of the FE of H_2 at Pt–Pd–Sn/C than at Pt–Sn/C indicates the suppression

of H_2 evolution reaction as well as H-adsorption at PtPd/Sn interfaces, which causes the higher FE of N_2 as well as higher N_2ORR activity at Pt–Pd–Sn/C than at Pt–Sn/C.

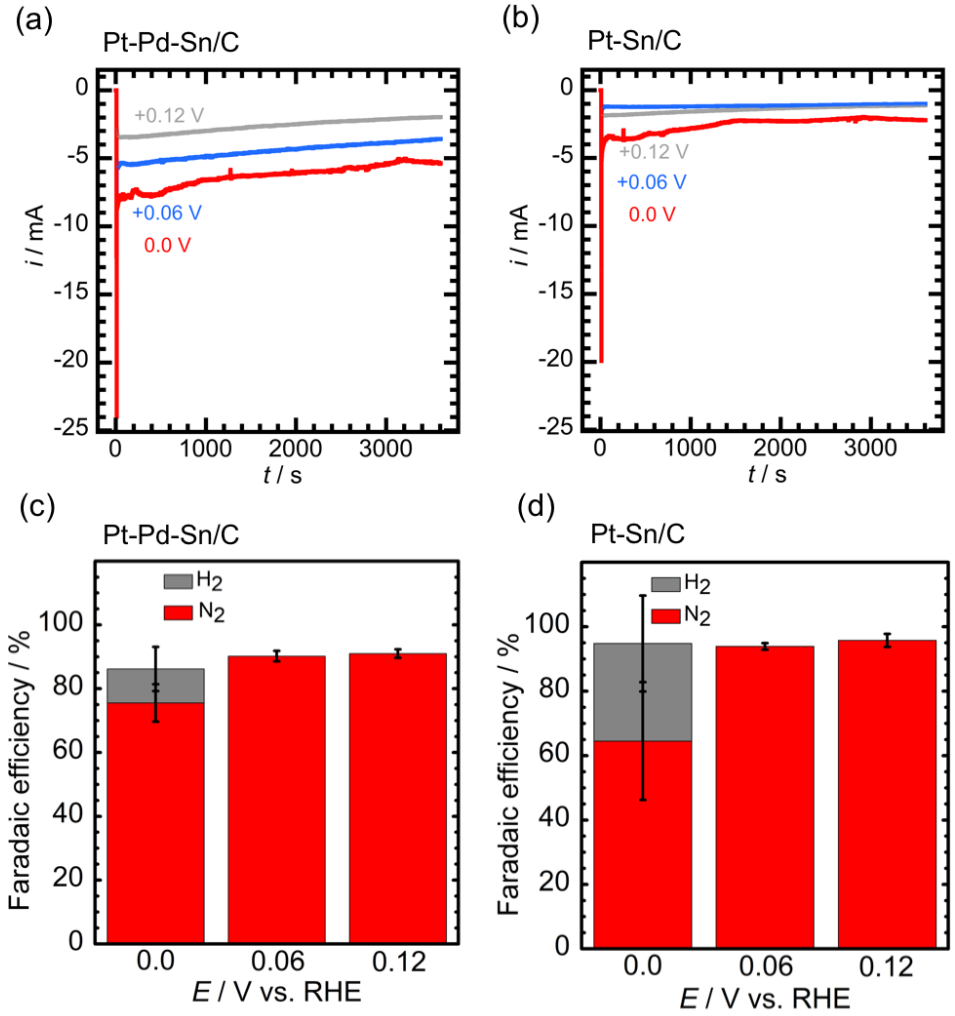


Figure 3.7 Chronoamperometry of (a) Pt–Pd–Sn/C and (b) Pt–Sn/C in a 0.1 M $HClO_4$ aqueous solution for 1 h at 0.0, +0.06, and +0.12 V vs. RHE under N_2O. Faradaic efficiencies of N_2 and H_2 obtained from N_2ORR at (c) Pt–Pd–Sn/C and (d) Pt–Sn/C.

Table 3.3 Faradaic efficiencies (FEs) of N_2 and H_2 obtained from N_2ORR at Pt–Pd–Sn/C and Pt–Sn/C after 1 h electrolysis at 0.0, +0.06, and +0.12 V vs. RHE.

Catalysts	FE / %			
	0.0 V vs. RHE		+0.06 V vs. RHE	+0.12 V vs. RHE
	H_2	N_2	N_2	N_2
Pt–Pd–Sn/C	10.67±6.95	75.49±5.86	90.20±1.65	91.00±1.32
Pt–Sn/C	30.23±14.84	64.38±18.27	93.62±1.05	95.56±2.03

The quantification of the amount of N_2 and H_2 allowed us to calculate their TOFs. The TOF of N_2 or H_2 indicates the number of moles of N_2 or H_2 is generated from per unit mole of noble metals per unit time [11,12]. TOF of N_2 at Pt–Pd–Sn/C increased with decreasing the potential from +0.12 V to 0.0 V vs. RHE and always found to greater than those at Pt–Sn/C (Figure 3.8 and Table 3.4). At +0.06 V vs. RHE, the Pt–Pd–Sn/C showed about three times higher TOF of 4.92 $\mathrm{mol}_{N_2}\ \mathrm{mol}^{-1}_{(Pt+Pd)}\ \mathrm{min}^{-1}$ than Pt–Sn/C, indicating the PtPd/Sn interface as the best for N_2 production from N_2ORR in acidic media. Even this value of TOF of N_2 is about 82 times greater than that on Pd foil electrode at +0.1 V vs. RHE calculated from a recently published report [18].

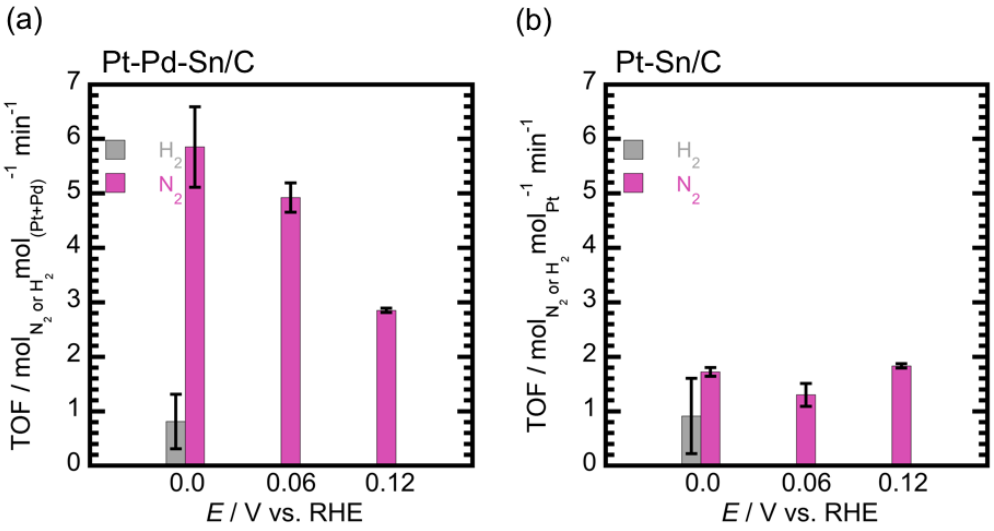


Figure 3.8 Turnover frequencies (TOFs) of N_2 and H_2 obtained from N_2ORR at (a) Pt–Pd–Sn/C and (b) Pt–Sn/C.

Table 3.4 Turnover frequencies (TOFs) of N_2 and H_2 obtained from N_2ORR at Pt–Pd–Sn/C and Pt–Sn/C after 1 h electrolysis at 0.0, +0.06, and +0.12 V vs. RHE.

Catalysts	TOF / $\mathrm{mol}_{N_2 \text{or } H_2}\mathrm{mol}^{-1}_{(Pt+Pd)}\ \mathrm{min}^{-1}$			
	0.0 V vs. RHE		+0.06 V vs. RHE	+0.12 V vs. RHE
	H_2	N_2	N_2	N_2
Pt–Pd–Sn/C	0.81±0.50	5.85±0.74	4.92±0.27	2.85±0.04
Pt–Sn/C	0.91±0.69	1.72±0.08	1.30±0.21	1.83±0.04

3.4 Conclusions

The PtPd/Sn interface of Pt–Pd–Sn/C exhibited the highest electrocatalytic N_2ORR activity in acidic media. The PtPd/Sn interface always showed greater TOF of N_2 than the Pt/Sn interface at any potential, although both the interfaces showed about 100% FE of N_2 at +0.06 V vs. RHE or more positive potential. It is most likely that the PtPd/Sn interface enhanced the adsorption of N_2O adsorption and/or suppressed the adsorption of hydrogen, as the lower FE of H_2 was observed at the PtPd/Sn interface than that at the Pt/Sn interface at 0.0 V vs. RHE. XPS observation of the Pt–Pd–Sn/C revealed the charge transfer from Sn to Pt and Pd, suggesting the modulation of the adsorption ability of N_2O and hydrogen at the PtPd/Sn interface. Our findings will be helpful to develop highly efficient p-block metal-containing noble metal mixture/alloy NPs for the practical application of N_2ORR to N_2.

3.5 References

[1] O. Badr, S.D. Probert, Nitrous Oxide in the Earth's Atmosphere, Appl. Energy. 41 (1992) 177–200. https://doi.org/10.1016/0306-2619(92)90002-S.

[2] H. Tian, R. Xu, J.G. Canadell, R.L. Thompson, W. Winiwarter, P. Suntharalingam, E.A. Davidson, P. Ciais, R.B. Jackson, G. Janssens-Maenhout, M.J. Prather, P. Regnier, N. Pan, S. Pan, G.P. Peters, H. Shi, F.N. Tubiello, S. Zaehle, F. Zhou, A. Arneth, G. Battaglia, S. Berthet, L. Bopp, A.F. Bouwman, E.T. Buitenhuis, J. Chang, M.P. Chipperfield, S.R.S. Dangal, E. Dlugokencky, J.W. Elkins, B.D. Eyre, B. Fu, B. Hall, A. Ito, F. Joos, P.B. Krummel, A. Landolfi, G.G. Laruelle, R. Lauerwald, W. Li, S. Lienert, T. Maavara, M. MacLeod, D.B. Millet, S. Olin, P.K. Patra, R.G. Prinn, P.A. Raymond, D.J. Ruiz, G.R. van der Werf, N. Vuichard, J. Wang, R.F. Weiss, K.C. Wells, C. Wilson, J. Yang, Y. Yao, A comprehensive quantification of global nitrous oxide sources and sinks, Nature. 586 (2020) 248–256. https://doi.org/10.1038/s41586-020-2780-0.

[3] A. Kudo, A. Mine, Electrocatalysis for N2O reduction on metal electrodes, J. Electroanal. Chem. 408 (1996) 267–269. https://doi.org/10.1016/0022-0728(96)04630-X.

[4] A. Kudo, A. Mine, Electrocatalytic reduction of nitrous oxide on metal and oxide electrodes in aqueous solution, Appl. Surf. Sci. 121–122 (1997) 538–542. https://doi.org/10.1016/S0169-4332(97)00362-0.

[5] A. Ahmadi, E. Bracey, R. Wyn Evans, G. Attard, Anion-surface interactions. Part II. Nitrous oxide reduction as a probe of anion adsorption on transition metal surfaces, J. Electroanal. Chem. 350 (1993) 297–316. https://doi.org/10.1016/0022-

0728(93)80212-Z.

[6] A. Aziznia, A. Bonakdarpour, E.L. Gyenge, C.W. Oloman, Electroreduction of nitrous oxide on platinum and palladium: Toward selective catalysts for methanol-nitrous oxide mixed-reactant fuel cells, Electrochim. Acta. 56 (2011) 5238–5244. https://doi.org/10.1016/j.electacta.2011.03.023.

[7] H. Ebert, R. Parsons, G. Ritzoulis, T. VanderNoot, The reduction of nitrous oxide on platinum electrodes in acid solution, J. Electroanal. Chem. 264 (1989) 181–193. https://doi.org/10.1016/0022-0728(89)80156-1.

[8] B. Wang, X.Y. Li, Electrocatalytic Properties of Nitrous Oxide and Its Voltammetric Detection at Palladium Electrodeposited on a Glassy Carbon Electrode, Anal. Chem. 70 (1998) 2181–2187. https://doi.org/10.1021/ac970601h.

[9] Y. Liu, M. Chi, V. Mazumder, K.L. More, S. Soled, J.D. Henao, S. Sun, Composition-controlled synthesis of bimetallic PdPt nanoparticles and their electro-oxidation of methanol, Chem. Mater. 23 (2011) 4199–4203. https://doi.org/10.1021/cm2014785.

[10] M.M. Magalhães, J.F. Gomes, G. Tremiliosi-Filho, P.B.S. de Figueiredo, R.B. de Lima, F. Colmati, Ethanol electro-oxidation on carbon-supported Pt3Sn/C, Pt3Cu/C and PtSnCu/C catalysts: CV and in situ FTIR study, J. Appl. Electrochem. 51 (2021) 173–181. https://doi.org/10.1007/s10800-020-01491-4.

[11] R. Sander, Compilation of Henry's law constants (version 4.0) for water as solvent, Atmos. Chem. Phys. 15 (2015) 4399–4981. https://doi.org/10.5194/acp-15-4399-2015.

[12] M. MacHida, Y. Tokudome, A. Maeda, Y. Kuzuhara, T. Hirakawa, T. Sato, H. Yoshida, J. Ohyama, K. Fujii, N. Ishikawa, Nanometric Platinum Overlayer to Catalyze NH3 Oxidation with High Turnover Frequency, ACS Catal. 10 (2020) 4677–4685. https://doi.org/10.1021/acscatal.0c00542.

[13] C. Costentin, G. Passard, J.M. Savéant, Benchmarking of homogeneous electrocatalysts: Overpotential, turnover frequency, limiting turnover number, J. Am. Chem. Soc. 137 (2015) 5461–5467. https://doi.org/10.1021/jacs.5b00914.

[14] R. Choi, S. Il Choi, C.H. Choi, K.M. Nam, S.I. Woo, J.T. Park, S.W. Han, Designed synthesis of well-defined Pd@Pt core-shell nanoparticles with controlled shell thickness as efficient oxygen reduction electrocatalysts, Chem. - A Eur. J. 19 (2013) 8190–8198. https://doi.org/10.1002/chem.201203834.

[15] M.O. Mavukkandy, S. Chakraborty, T. Abbasi, S.A. Abbasi, A clean-green synthesis of platinum nanoparticles utilizing a pernicious weed lantana (Lantana camara), Am. J. Eng. Appl. Sci. 9 (2016) 84–90. https://doi.org/10.3844/ajeassp.2016.84.90.

[16] Z. Liu, B. Guo, L. Hong, T.H. Lim, Microwave heated polyol synthesis of carbon-supported PtSn nanoparticles for methanol electrooxidation, Electrochem. Commun. 8 (2006) 83–90. https://doi.org/10.1016/j.elecom.2005.10.019.

[17] J. Yang, M. Duca, K.J.P. Schouten, M.T.M. Koper, Formation of volatile products during nitrate reduction on a Sn-modified Pt electrode in acid solution, J. Electroanal. Chem. 662 (2011) 87–92. https://doi.org/10.1016/j.jelechem.2011.03.015.

[18] B.H. Ko, B. Hasa, H. Shin, Y. Zhao, F. Jiao, Electrochemical Reduction of Gaseous Nitrogen Oxides on Transition Metals at Ambient Conditions, J. Am. Chem. Soc. 144 (2022) 1258–1266. https://doi.org/10.1021/jacs.1c10535.

Chapter 4

Electrocatalytic Nitrous Oxide Reduction at Sn-Modified Pd Nanocubes

4.1 Introduction

Nitrous oxide (N_2O), a potent greenhouse gas, is accountable for stratospheric ozone depletion and global warming and can be removed using electrocatalytic technologies [1,2]. Noble metal electrodes, such as Pt and Pd substrates have been widely studied for electrocatalytic N_2O reduction reaction (N_2ORR) [3–8]. Generally, Pd has low N_2ORR activity in acidic media, although it showed about 100% Faradaic efficiency of N_2 [3,5,7,8]. Lower N_2O adsorption energy than hydrogen adsorption energy on Pd may also be accountable for such low N_2ORR activity [8–10]. In Chapter 2, electrocatalytic N_2ORR activity was improved at Pd nanoparticles (NPs) prepared by an arc-plasma deposition (APD) method on fluorine-doped tin oxide (FTO) substrates (Pd/FTO), in which Pd/Sn interfaces plays an important role for the enhancement of N_2ORR activity. Even the presence of Pd in the chemically synthesized Pt–Pd–Sn NPs made double the N_2ORR activity than Pt–Sn NPs, which has been discussed in Chapter 3.

Atomic arrangement on the electrode surface and electrode materials play a vital role in the betterment of the catalytic activity. For example, Sn-modified Pd(100) electrode (Sn/Pd(100)) showed higher NO_3RR activity than Sn-modified Pd(111) electrode (Sn/Pd(111)) [11,12]. Even Sn/Pd(100) and Sn-modified PdPt(100) (3 wt% Pd) electrodes were reported to be promising catalysts for high N_2 selectivity obtained from NO_3RR [12]. As N_2O is the key intermediate for the production of N_2 from NO_3RR, the Sn/Pd(100) might have high N_2ORR activity to N_2. Similar to Pd(100) surface, a Pd nanocube (NC) has six (100) facets that inspired us to investigate N_2ORR activity at the Pd NC and the Sn-modified Pd NC was expected to show high N_2ORR activity.

Herein, we report the preparation of Pd NC and Sn-modified Pd NC to understand the role of Pd/Sn interfaces at ordered surface for electrocatalytic N_2ORR activity in acidic media. To understand the size and shape, the Pd NCs were characterized by transmission electron microscopy (TEM).

4.2 Experimental section

4.2.1 Materials

Ethanol, 2-propanol, perchloric acid (60%), palladium(II) chloride ($PdCl_2$, 99.9%), L(+)-ascorbic acid (99.5%), and 5% Nafion DE520 were obtained from Wako Pure Chemical Industries, Ltd. Hexadecyltrimethylammonium bromide (CTAB, 98.0%) and tin(II) chloride dihydrate (97%) were purchased from Tokyo Chemical Industry Co., Ltd. and Kanto Chemical Co., Inc., respectively. Vulcan XC-72 carbon black was bought from Cabot Corporation. Pure argon gas (99.9995%, Hokkaido Air Water) and nitrous oxide (99.5%, GL Science) were used for electrochemical measurements.

4.2.2 Synthesis of Pd nanocubes

Pd nanocubes (NCs) were synthesized using a 10 mM tetrachloropalladic acid (H_2PdCl_4) solution precursor based on a reported synthetic procedure, in which all solutions were prepared in Milli-Q water [13]. Firstly, the 10 mM H_2PdCl_4 solution was prepared by dissolving 17.7 mg of the $PdCl_2$ (0.1 mmol) in 5 mL of 40 mM HCl (0.2 mmol) under ultrasonication for two hours and further diluting to 10 mL with Milli-Q water. Next, to prepare Pd nanocubes (NCs), 70 mL of 12.5 mM of CTAB solution was added to a round bottom flask (100 mL), and heated at 95 °C for 5 min under magnetic stirring. Then, 3.5 mL of the 10 mM H_2PdCl_4 solution was added to the CTAB solution at 95 °C and the mixture was kept at this temperature for 5 min before adding 560 μL of freshly prepared 100 mM ascorbic acid solution. The reaction was allowed to proceed for 30 min and then, a dark brown mixture of Pd NCs was obtained. After the mixture had cooled to room temperature, the Pd NCs were separated by centrifugation at 12,000 rpm at 25 °C for 10 min using a Micro Refrigerated Centrifuge 3700 equipped with an angle rotor AF-5004CA (Kubota Co.). Then, the Pd NCs were washed with ca. 15 mL of Milli-Q water for two times by centrifugation at 12,000 rpm for 10 min followed by ca. 15 mL of 1 M NaOH for one time and ca. 15 mL of ethanol five-time at 8,000 rpm for 5 min and finally stored in 5 mL of ethanol at room temperature until use.

4.2.3 Preparation of carbon-supported Pd NCs

Vulcan XC-72 carbon black (ca. 1.2 mg) and Pd NCs (ca. 0.3 mg) were dispersed in 10 mL of ethanol and the mixture was ultrasonicated for three hours in order to the impregnation of the NCs on the carbon support. After that, the mixture was collected by

centrifugation at 12, 000 rpm for 7 min and then, re-dispersed in 900 μL of 2-propanol and 1600 μL of Milli-Q water. The mixture was transferred into 5 mL of a glass vial and 10 μL of 5% Nafion DE520 was added. The mixture was ultrasonicated for three hours to obtain the catalyst ink of carbon-supported Pd NCs (Pd_NC/C) for the preparation of working electrodes.

4.2.4 Catalyst characterization

Transmission electron microscopy (TEM) images of Pd NCs and Pd_NC/C were taken by a JEM-2000FX (JEOL) at an acceleration voltage of 200 kV.

4.2.5 Electrochemical measurements

Electrochemical measurements were performed using a conventional three-electrode, one compartment electrochemical cell by a potentiostat HZ-7000 (Hokuto Denko Corp.). A platinized Pt foil and an Ag|AgCl (sat. KCl) were used as the counter and the reference electrodes, respectively. A glassy carbon (GC) plate, on which the catalyst was cast, was used as the working electrode.

A GC plate ($25 \times 25 \times 2$ mm^3, AS ALS Co., Ltd.) was polished with alumina slurry (0.3 μm, Baikalox), followed by alumina slurry (0.05 μm, Baikalox), and then sonicated in water, ethanol, and Milli-Q water for 5 min each. A polyethylene tape with a prepared hole of 8 mm in diameter was placed on the GC plate to control the surface area of the working electrode. Thus, the geometrical surface area of the working electrode was controlled to be 0.50 cm^2. To characterize Pd NC without carbon support and Nafion, 50 μL of Pd NC dispersed in ethanol was cast on the hole of the GC and dried the solvent at 40 °C, and the electrode was referred to as Pd_NC/GC. Next, for making Pd_NC/C ink-modified GC electrodes, the catalyst ink (45.6 μL) was cast on the hole to control the Pd loading of 11.2 μg cm^{-2}, and then removed the solvent at 40 °C for 20 min, and the electrode was further assigned as the Pd_NC/C.

For characterizing Pd_NC/GC, cyclic voltammograms (CVs) were recorded in both 0.1 M H_2SO_4 and 0.1 M $HClO_4$ aqueous solutions. Before measurements of CVs, the electrolyte solution was purged with Ar (99.999%, Hokkaido Air Water Inc.) for at least 30 min. The Pd_NC/GC was electrochemical cleaned for five cycles at 200 mV s^{-1} to get stable CVs in the potential range between –0.16 and +0.44 V vs. Ag|AgCl (sat. KCl) in a

0.1 M H_2SO_4 aqueous solution under Ar before recording CVs at 50 mV s^{-1} in the text, and then in a 0.1 M $HClO_4$ aqueous solution at 50 mV s^{-1}.

In the case of Pd_NC/C, five potential cycles were cleaned at 200 mV s^{-1} to remove the impurities and to get stable CVs in the potential range between –0.2 and +0.25 V vs. Ag|AgCl (sat. KCl) in a 0.1 M $HClO_4$ aqueous solution under Ar before recording CVs at 50 mV s^{-1} in the text. For electrochemical N_2O reduction, a 0.1 M $HClO_4$ aqueous solution in the electrochemical cell was saturated with bubbling of N_2O gas at 10 mL min^{-1} for 30 min, and then the CVs were recorded under N_2O at a sweep rate of 10 mV s^{-1}. The first cycle of the CVs was always used for making a graph in presence of N_2O. All potentials shown were converted to be versus the reversible hydrogen electrode (RHE) by using the following equation: E (vs. RHE) = E (vs. Ag|AgCl (sat. KCl)) + 0.199 + 0.059 × pH.

The surface modification of Pd_NC/C with tin was carried out based on a reported procedure [14]. The Pd_NC/C was immersed in 0.1 M $HClO_4$ aqueous solution containing 10 mM $SnCl_2$ under Ar for 20 min and then the electrode was immersed in Milli-Q water to remove excess tin species from the surface. The CVs of tin-modified Pd_NC/C (Sn/Pd_NC/C) in the underpotentially hydrogen adsorption/desorption region in 0.1 M $HClO_4$ aqueous solution allowed us to determine the tin surface coverage (θ_{Sn}) using the following equation: $\theta_{Sn} = (Q_H^0 - Q_H)/Q_H^0$, where $Q_H^0$and Q_H indicate the Faradaic charges corresponding to the hydrogen desorption before and after the tin modification, respectively.

4.3 Results and discussion

4.3.1 Synthesis and characterization of Pd NCs

Pd NCs were prepared by the addition of H_2PdCl_4 precursor solution and ascorbic acid solution, a reducing agent, in a solution of CTAB as a caping agent [13]. The bromide ions (Br^-) from CTAB bind to the {100} sites of Pd and promote the formation of Pd NC [13]. After synthesizing the NCs were washed with Milli-Q water, 1 M NaOH, and ethanol, as the cleaning of the surface of Pd NCs with NaOH was reported in the literature [15,16]. The TEM image revealed the formation of the Pd NCs that were enclosed by six {100} facets with an average edge length of 20.6±1.9 nm and loaded on carbon support (Pd_NC/C) (Figure 4.1).

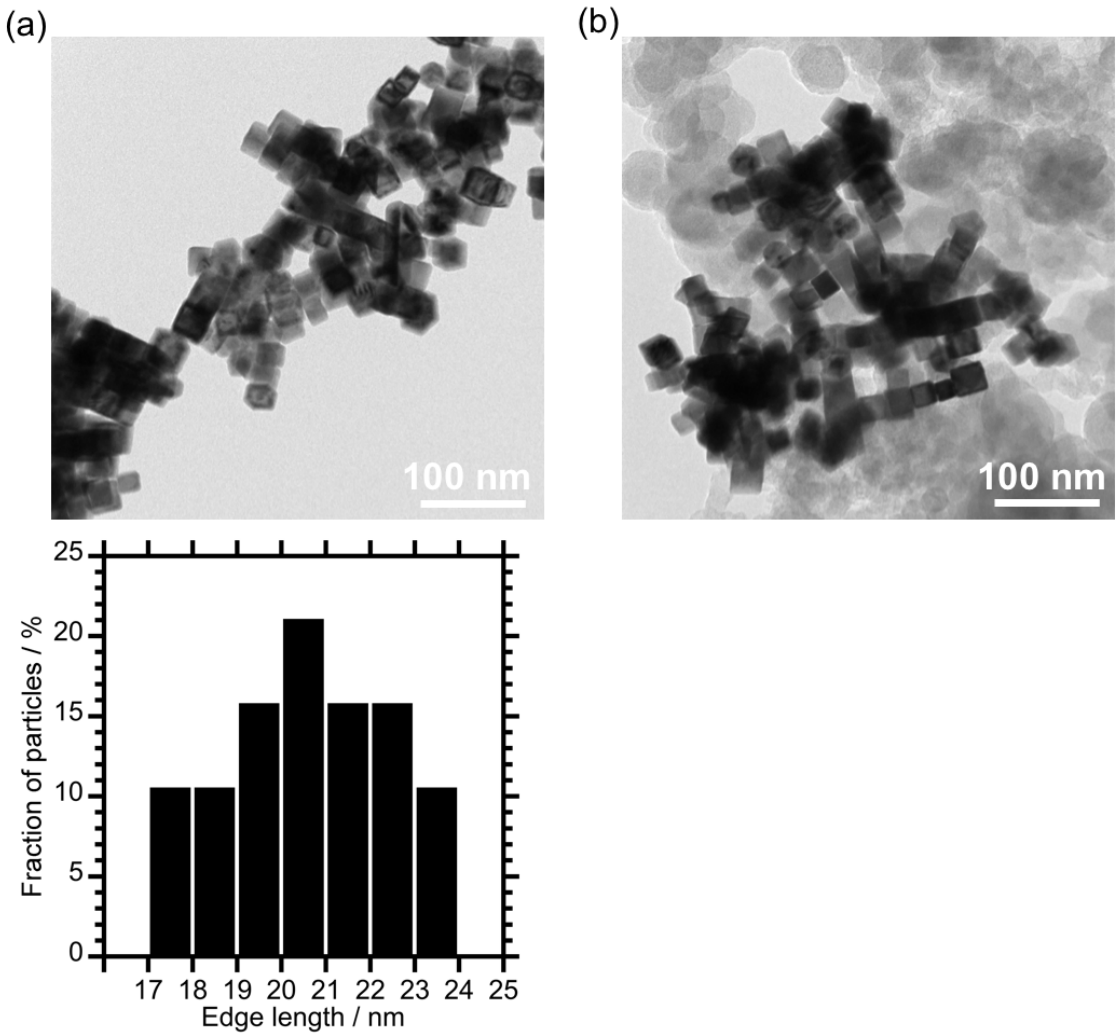


Figure 4.1 (a) TEM image of Pd NCs and their edge-length-distribution and, (b) TEM image of Pd_NC/C.

The CVs of the Pd NCs on glassy carbon (GC) substrates (Pd_NC/GC) in both 0.1 M H_2SO_4 and 0.1 M $HClO_4$ aqueous solutions showed characteristic features of {100} facets in the potential region of hydrogen adsorption and desorption (Figure 4.2a) [16,17]. In a 0.1 M H_2SO_4 aqueous solution, the hydrogen/(bi) sulfate anion adsorption and desorption peaks were observed at 0.22 and 0.28 V vs. RHE, respectively, which were reported in the previous studies [16,17]. In a 0.1 M $HClO_4$ aqueous solution, the hydrogen adsorption and desorption peaks were also observed at 0.20 and 0.27 V vs. RHE. On the other hand, Pd_NC/C showed the hydrogen desorption peak at 0.19 V vs. RHE and the hydrogen adsorption currents without showing any peak in 0.1 M $HClO_4$ aqueous solution (Figure 4.2b). This could be due to the presence of carbon and Nafion on the Pd NCs.

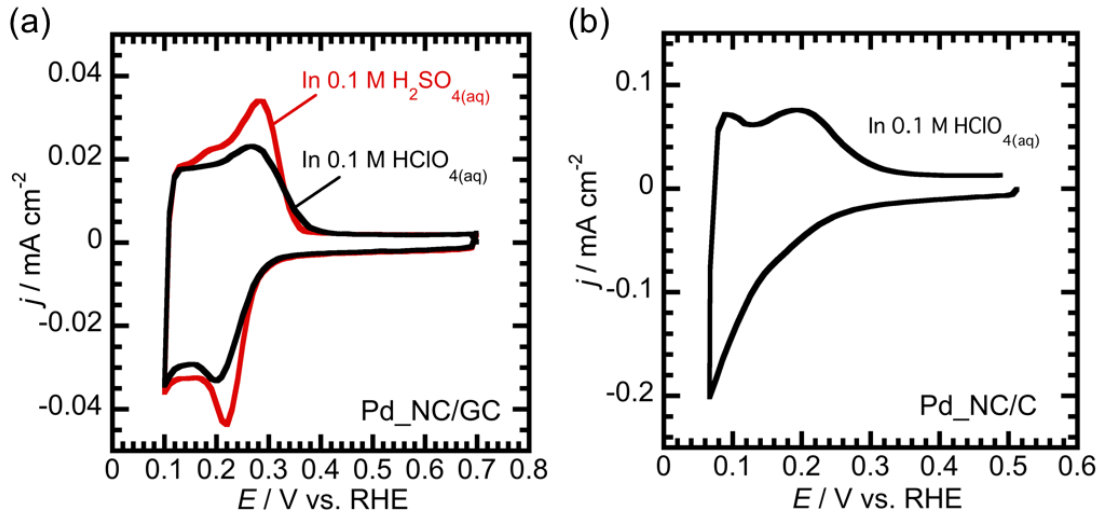


Figure 4.2 CVs of (a) Pd_NC/GC in 0.1 M H_2SO_4 and 0.1 M $HClO_4$ aqueous solutions at a sweep rate of 50 mV s^{-1} under Ar and (b) Pd_NC/C in a 0.1 M $HClO_4$ aqueous solution at a sweep rate of 50 mV s^{-1} under Ar.

4.3.2 Characterization of Sn-modified Pd_NC/C

The surface of Pd NCs of Pd_NC/C electrode was modified with Sn using an irreversible adsorbtion method [14]. The Pd_NC/C electrode was immersed in 0.1 M $HClO_4$ aqueous solution containing 10 mM $SnCl_2$ for 20 min to get Sn-modified Pd_NC/C electrodes (Sn/Pd_NC/C). The CVs of the Pd_NC/C and Sn/Pd_NC/C electrodes were recorded in 0.1 M $HClO_4$ aqueous solution at a sweep rate of 50 mV s^{-1} under Ar (Figure 4.3). For Sn/Pd_NC/C electrode, the current associated with H-adsorption/desorption was reduced when compared to that with Pd_NC/C because the H-adsorption site is blocked by the Sn ad-atoms of the Sn/Pd_NC/C electrode [18]. The Sn coverage (θ_{Sn}) was determined to be 0.87 using the following equation: $\theta_{Sn} = (Q_H^0 - Q_H)/Q_H^0 = 1 - Q_H/Q_H^0$, where $Q_H^0$and Q_H indicate the Faradaic charges corresponding to the H-desorption from Pd_NC/C and Sn/Pd_NC/C electrodes, respectively (Figure 4.3).

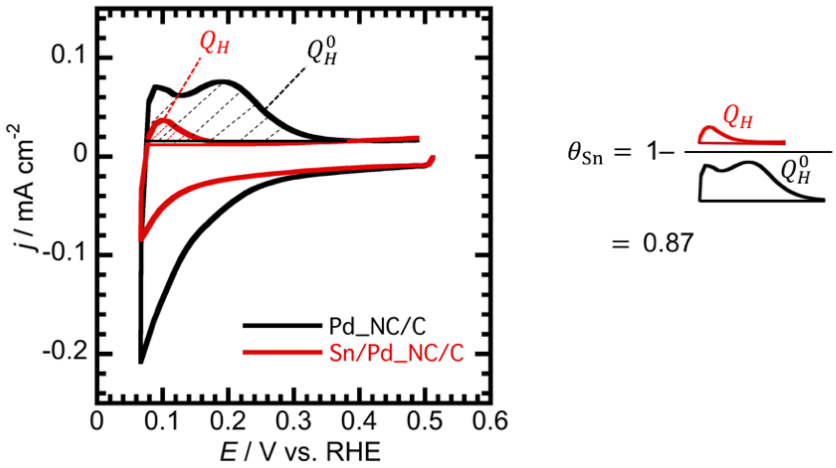


Figure 4.3 CVs of Pd_NC/C before Sn modification and after Sn modification (Sn/Pd_NC/C) in a 0.1 M $HClO_4$ aqueous solutions at a sweep rate of 50 mV s^{-1} under Ar.

4.3.3 Electrocatalytic N_2ORR at Sn/Pd_NC/C

To evaluate the electrocatalytic activity of Sn/Pd_NC/C for N_2ORR, the CVs of the Sn/Pd_NC/C and Pd_NC/C were recorded in a 0.1 M $HClO_4$ aqueous solution at a sweep rate of 10 mV s^{-1} under N_2O (Figure 4.4). The Sn/Pd_NC/C showed cathodic currents in the potential range between +0.06 and +0.36 V vs. RHE only under N_2O. In this potential region, the Sn/Pd_NC/C showed poor H-adsorption/desorption currents under Ar. These results indicate that the currents can be associated with the electrochemical N_2ORR [5,8]. The Sn/Pd_NC/C showed much higher N_2ORR currents than Pd_NC/C, indicating the effective role of Pd/Sn interfaces for the acceleration of N_2ORR activity. A similar result was explained at Pd/Sn interfaces for N_2ORR at arc-plasma deposited Pd nanoparticles (NPs) on fluorine-doped tin oxide (FTO) electrodes (Pd/FTO) in Chapter 2. The N_2ORR current density at +0.16 V vs. RHE was found to be –0.09 mA cm^{-2} at Sn/Pd_NC/C, which is about two times higher than –0.05 mA cm^{-2} at the Pd/FTO (Figure 4.4b and Table 4.1).

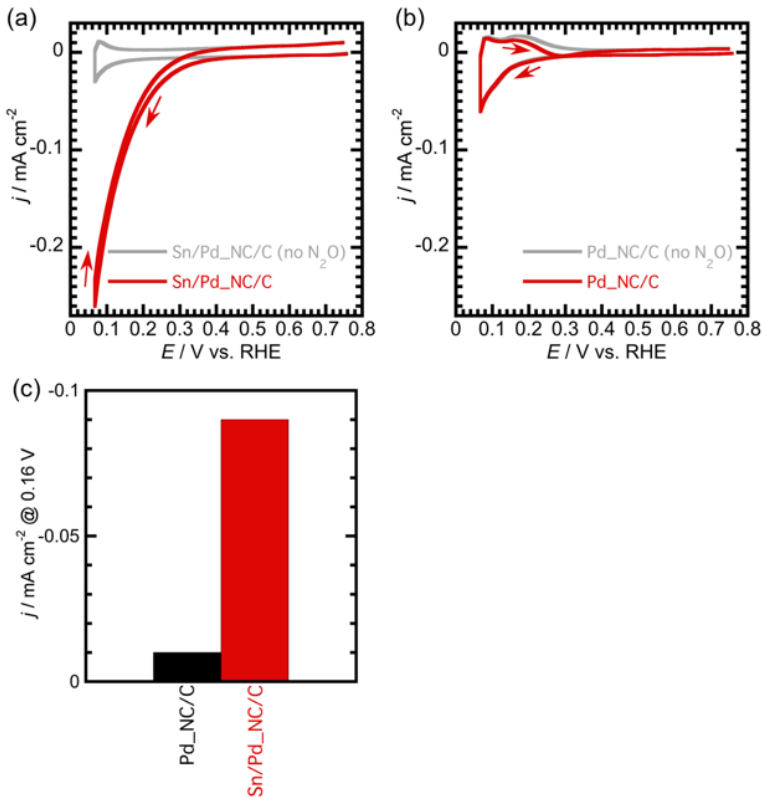


Figure 4.4 CVs of (a) Sn/Pd_NC/C and (b) Pd_NC/C in a 0.1 M $HClO_4$ aqueous solution at a sweep rate of 10 mV s^{-1} under N_2O. (c) The histogram of the N_2ORR current density at +0.16 V vs. RHE.

Table 4.1 N_2ORR current densities (j) at +0.16 V vs. RHE are shown by the Sn/Pd_NC/C and Pd_NC/C in Figure 4.4 and Pd/FTO from Chapter 2.

Electrode	j/mA cm^{-2}
Sn/Pd_NC/C	–0.09
Pd_NC/C	–0.010
Pd/FTO	–0.05±0.01

The Sn/Pd_NC/C showed N_2ORR currents in the potential region between +0.06 and +0.36 V vs. RHE (Figure 4.4). In this potential region, the adsorption of N_2O competes with the adsorption of hydrogen at Pd_NC/C (Figure 4.3) [5,8]. The presence of Sn in Sn/Pd_NC/C decreased the onset potential of H-adsorption from +0.36 V to +0.2 V vs. RHE. Thus, the Pd/Sn interface of Sn/Pd_NC/C enhanced the adsorption of N_2O through the suppression of H-adsorption, leading to the enhancement of the N_2ORR activity. Moreover, at +0.16 V vs. RHE, the Sn/Pd_NC/C showed N_2ORR current density about three times lower than Pt–Sn/C and about six times lower than Pt–Pd–Sn/C in Chapter 3. Therefore, future work is needed to improve the N_2ORR activity of Pd NCs: i) optimization of Sn-coverage on Pd_NCs and, ii) synthesis of Pd–Pt NCs and modification of their surfaces with Sn.

4.4 Conclusions

The Pd/Sn interface of Sn/Pd_NC/C showed the maximum electrocatalytic N_2ORR activity in acidic media. The suppression of H-adsorption at the Pd/Sn interface of Sn/Pd_NC/C when compared with Pd_NC/C, may enhance the adsorption of N_2O, resulting in the enhancement of the N_2ORR activity. Our findings will be helpful to develop highly efficient p-block metal modified shape-controlled noble metal mixture/alloy NPs for the practical application of N_2ORR to N_2.

4.5 References

[1] O. Badr, S.D. Probert, Nitrous Oxide in the Earth's Atmosphere, Appl. Energy. 41 (1992) 177–200. https://doi.org/10.1016/0306-2619(92)90002-S.

[2] H. Tian, R. Xu, J.G. Canadell, R.L. Thompson, W. Winiwarter, P. Suntharalingam, E.A. Davidson, P. Ciais, R.B. Jackson, G. Janssens-Maenhout, M.J. Prather, P. Regnier, N. Pan, S. Pan, G.P. Peters, H. Shi, F.N. Tubiello, S. Zaehle, F. Zhou, A. Arneth, G. Battaglia, S. Berthet, L. Bopp, A.F. Bouwman, E.T. Buitenhuis, J. Chang, M.P. Chipperfield, S.R.S. Dangal, E. Dlugokencky, J.W. Elkins, B.D. Eyre, B. Fu, B. Hall, A. Ito, F. Joos, P.B. Krummel, A. Landolfi, G.G. Laruelle, R. Lauerwald, W. Li, S. Lienert, T. Maavara, M. MacLeod, D.B. Millet, S. Olin, P.K. Patra, R.G. Prinn, P.A. Raymond, D.J. Ruiz, G.R. van der Werf, N. Vuichard, J. Wang, R.F. Weiss, K.C. Wells, C. Wilson, J. Yang, Y. Yao, A comprehensive quantification of global nitrous oxide sources and sinks, Nature.

586 (2020) 248–256. https://doi.org/10.1038/s41586-020-2780-0.

[3] A. Kudo, A. Mine, Electrocatalysis for N2O reduction on metal electrodes, J. Electroanal. Chem. 408 (1996) 267–269. https://doi.org/10.1016/0022-0728(96)04630-X.

[4] A. Kudo, A. Mine, Electrocatalytic reduction of nitrous oxide on metal and oxide electrodes in aqueous solution, Appl. Surf. Sci. 121–122 (1997) 538–542. https://doi.org/10.1016/S0169-4332(97)00362-0.

[5] A. Ahmadi, E. Bracey, R. Wyn Evans, G. Attard, Anion-surface interactions. Part II. Nitrous oxide reduction as a probe of anion adsorption on transition metal surfaces, J. Electroanal. Chem. 350 (1993) 297–316. https://doi.org/10.1016/0022-0728(93)80212-Z.

[6] A. Aziznia, A. Bonakdarpour, E.L. Gyenge, C.W. Oloman, Electroreduction of nitrous oxide on platinum and palladium: Toward selective catalysts for methanol-nitrous oxide mixed-reactant fuel cells, Electrochim. Acta. 56 (2011) 5238–5244. https://doi.org/10.1016/j.electacta.2011.03.023.

[7] H. Ebert, R. Parsons, G. Ritzoulis, T. VanderNoot, The reduction of nitrous oxide on platinum electrodes in acid solution, J. Electroanal. Chem. 264 (1989) 181–193. https://doi.org/10.1016/0022-0728(89)80156-1.

[8] B. Wang, X.Y. Li, Electrocatalytic Properties of Nitrous Oxide and Its Voltammetric Detection at Palladium Electrodeposited on a Glassy Carbon Electrode, Anal. Chem. 70 (1998) 2181–2187. https://doi.org/10.1021/ac970601h.

[9] A. V. Zeigarnik, Adsorption and Reactions of N 2 O on Transition Metal Surfaces, Kinet. Catal. 44 (2002) 233–246.

[10] I.A. Pašti, N.M. Gavrilov, S. V. Mentus, Hydrogen adsorption on palladium and platinum overlayers: DFT study, Adv. Phys. Chem. 2011 (2011). https://doi.org/10.1155/2011/305634.

[11] M. Kato, M. Okui, S. Taguchi, I. Yagi, Electrocatalytic nitrate reduction on well-defined surfaces of tin-modified platinum, palladium and platinum-palladium single crystalline electrodes in acidic and neutral media, J. Electroanal. Chem. 800 (2017) 46–53. https://doi.org/10.1016/j.jelechem.2017.01.020.

[12] M. Kato, Y. Unuma, M. Okui, Y. Qu, J. Zheng, S. Taguchi, F. Kiguchi, M. Torihata, Y. Gao, N. Hoshi, I. Yagi, Electrocatalytic activity and volatile product selectivity for nitrate reduction at tin-modified Pt(100), Pd(100) and Pd–Pt(100)

single crystal electrodes in acidic media, Electrochim. Acta. 398 (2021) 139281. https://doi.org/10.1016/j.electacta.2021.139281.

[13] W. Niu, Z.Y. Li, L. Shi, X. Liu, H. Li, S. Han, J. Chen, G. Xu, Seed-mediated growth of nearly monodisperse palladium nanocubes with controllable sizes, Cryst. Growth Des. 8 (2008) 4440–4444. https://doi.org/10.1021/cg8002433.

[14] M. Kato, M. Okui, S. Taguchi, I. Yagi, Electrocatalytic nitrate reduction on well-defined surfaces of tin-modified platinum, palladium and platinum-palladium single crystalline electrodes in acidic and neutral media, J. Electroanal. Chem. 800 (2017) 46–53. https://doi.org/10.1016/j.jelechem.2017.01.020.

[15] M.A. Montiel, F.J. Vidal-Iglesias, V. Montiel, J. Solla-Gullón, Electrocatalysis on shape-controlled metal nanoparticles: Progress in surface cleaning methodologies, Curr. Opin. Electrochem. 1 (2017) 34–39. https://doi.org/10.1016/j.coelec.2016.12.007.

[16] E. Garnier, F.J. Vidal-Iglesias, J.M. Feliu, J. Solla-Gullón, Surface Structure Characterization of Shape and Size Controlled Pd Nanoparticles by Cu UPD: A Quantitative Approach, Front. Chem. 7 (2019) 1–11. https://doi.org/10.3389/fchem.2019.00527.

[17] H. Erikson, A. Sarapuu, K. Tammeveski, J. Solla-Gullón, J.M. Feliu, Enhanced electrocatalytic activity of cubic Pd nanoparticles towards the oxygen reduction reaction in acid media, Electrochem. Commun. 13 (2011) 734–737. https://doi.org/10.1016/j.elecom.2011.04.024.

[18] Q.W. Zheng, C.J. Fan, C.H. Zhen, Z.Y. Zhou, S.G. Sun, Irreversible adsorption of Sn adatoms on basal planes of Pt single crystal and its impact on electrooxidation of ethanol, Electrochim. Acta. 53 (2008) 6081–6088. https://doi.org/10.1016/j.electacta.2008.01.078.

Chapter 5

General Conclusions

In this study, firstly in Chapter 2, the Pt and/or Pd nanoparticle (NP)-deposited fluorine-doped tin oxide (FTO) electrodes prepared by the arc-plasma deposition (APD) method were examined for the electrocatalytic reduction of NO_3^-, NO_2^-, NO, and N_2O in acidic media to investigate the role of the PtPd/Sn interface. The trimetallic PtPd/Sn interface of the Pt/Pd/FTO showed higher catalytic activity than the bimetallic Pt/Sn or Pd/Sn interface for the NO_3RR and N_2ORR, whereas the PtPd/Sn interface showed no drastic contribution to the electrocatalytic NO_2^- and NO reduction reactions. Because the NO_3^- and N_2O reduction reactions occur in the potential region of H-adsorption on Pt and Pd electrodes, the PtPd/Sn interface could enhance NO_3^- and N_2O adsorption and/or suppress the H-adsorption.

In Chapter 3, Pt–Sn and Pt–Pd–Sn NPs on carbon support were prepared for the electrocatalytic N_2ORR. TEM, STEM, and EDS mapping images confirmed the formation of Sn-patched Pt and Pt-Pd mixture NPs. The trimetallic Pt–Pd–Sn NPs showed higher N_2ORR activity than the bimetallic Pt–Sn NPs. The suppression of H-adsorption was confirmed from the lower FE of H_2 at the PtPd/Sn interface than that at the Pt/Sn interface at 0.0 V vs. RHE, resulting in the high N_2ORR activity at the PtPd/Sn interface. The PtPd/Sn interface showed TOF of 4.92 $\mathrm{mol}_{\mathrm{N_2}}\ \mathrm{mol}_{(\mathrm{Pt+Pd})}^{-1}\mathrm{min}^{-1}$ for the N_2ORR to N_2 with about 100% Faradaic efficiency at +0.06 V vs. RHE.

In Chapter 4, Pd nanocubes (NCs) supported on carbon were prepared, modified with Sn, and then studied for the electrocatalytic N_2ORR. TEM images confirmed the preparation of NCs. The Sn modification increases the N_2ORR activity of NCs. The Sn modification could suppress the H-adsorption at Pd(100) surfaces, resulting in the enhancement of the N_2ORR activity at Pd/Sn interfaces.

In conclusion, it was demonstrated that the enhancement of NO_3^- and N_2O adsorption and/or suppression of H-adsorption is necessary at the electrode surface for the improvement of the NO_3RR and N_2ORR in acidic media. The trimetallic PtPd/Sn interface can highly modulate such competitive adsorption processes, resulting in the high NO_3RR and N_2ORR activity. The suppression of H-adsorption could favor N_2 formation rather than

the formation of protonated species such as NH_4^+ and NH_3OH^+ for the NO_3RR. Furthermore, the Pd/Sn interface of Sn-modified Pd NCs improved more N_2ORR activity than unmodified Pd NCs through the suppression of H-adsorption. The catalysts could be useful for real groundwater treatment (and N_2O removal (Figure 5.1)) using polymer electrolyte membrane (PEM)-type electrolysis cell, in which the H^+ ions produced from water oxidation in the anodic chamber move through the PEM to the cathodic chamber and keep continuing the cathodic reaction [1]. Our findings will be helpful for making highly efficient interfaces between Pt-Pd mixture/alloy NPs and Sn or shape-controlled Pt-Pd mixture/alloy NPs and Sn for the modulation of the NO_3^-, N_2O, and H-adsorption processes.

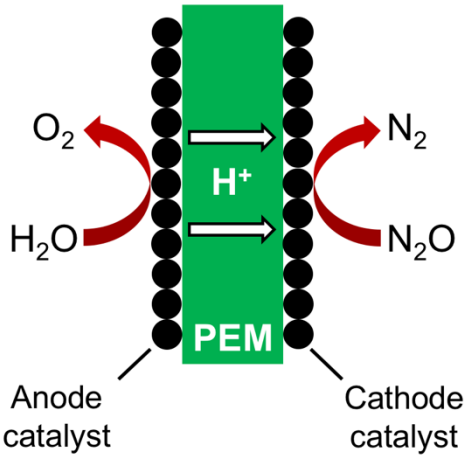


Figure 5.1 Schematic representation of the electrocatalytic N_2O removal in a PEM-type electrolysis cell.

[1] S. Bunea, K. Clemens, A. Urakawa, Electrified Conversion of Contaminated Water to Value: Selective Conversion of Aqueous Nitrate to Ammonia in a Polymer Electrolyte Membrane Cell, ChemSusChem. 15 (2022) 1–9. https://doi.org/10.1002/cssc.202102180.

Acknowledgments

The study presented in this thesis has been carried out at Yagi Laboratory, Division of Environmental Materials Science, Graduate School of Environmental Science, Hokkaido University. It was my privilege to have the opportunity to work at Yagi Laboratory. I earned the most valuable chemistry education and research knowledge from Professor Yagi's research group. I would like to express my sincere gratitude to my supervisor Professor Ichizo Yagi for his continuous guidance, dedication, suggestions, discussions, and encouragement throughout my Doctoral journey. I would like to acknowledge Associate Professor Masaru Kato for his continuous guidance, suggestions, encouragement, and time to discuss every single point of this study. I am grateful to Assistant Professor Kou Nakata for his suggetions on product detection; all the members of Yagi Laboratory for their cooperation and inspiration; the staff of Yagi Laboratory for administrative cooperation.

I would like to acknowledge Professor Yuichi Kamiya and Associate Professor Yukatsu Shichibu, Faculty of Environmental Earth Science, Graduate School of Environmental Science, Hokkaido University for reviewing this thesis and their valuable sugessions. I am thankful to Professor Shinichiro Noro, Faculty of Environmental Earth Science, Graduate School of Environmental Science, Hokkaido University for giving XRD facilities. I would like to thank Takashi Tanioka and Ryoko Yokohira (Faculty of Engineering, Hokkaido University) for taking TEM images; Naomi Hirai and Yuko Mori (Research Institute for Electronic Science, Hokkaido University) for taking the STEM and EDS mapping images and XPS data; Nozomi Takeda (Open Facility Division, Hokkaido University) for ICP-MS measurments.

I would like to acknowledge the financial support of the Ministry of Education, Culture, Sports, Science and Technology (MEXT), Japan.

I would like to acknowledge Begum Rokeya University, Rangpur, Bangladesh for giving me study leave to achieve Doctoral education. I also would like to thank my teachers and friends for their support.

Finally, I would like to remember my family members and their dedication in every step of my life. I am grateful to Sonia Das (wife), Kira Sarker (daughter), and my parents for their unconditional caring and support.